# LAYERED OXIDE PHASES FOR SODIUM-ION BATTERY ELECTRODES

by

Ryan I. Fielden

Submitted in partial fulfilment of the requirements
for the degree of Master of Science

at

Dalhousie University
Halifax, Nova Scotia
August 2014

**DEDICATION PAGE**

I would like to dedicate this work to my son Isaac Ethan Fielden, who was born on March 12th 2013 during the heart of this work. Isaac has become an unlimited source of motivation. I know that even after my formal education is over I still have a great deal more to learn and understand. I hope he is blessed with tremendous teachers as I have been.

"I am indebted to my Father for living,
but to my teacher for living well."

-Alexander the Great

# TABLE OF CONTENTS

# LIST OF TABLES

# LIST OF FIGURES

# ABSTRACT

Sodium-ion batteries could offer an economical and environmentally friendly alternative to lithium-ion batteries, however many challenges must be overcome first. This project focused on the investigation of layered sodium transition metal oxide phase systems. These systems are of great importance for the development of not only cathode materials but anode materials as well for sodium-ion batteries. The high energy densities and ease of sodium intercalation of these layered systems make them prime candidates for implementation in sodium-ion batteries. It is desirable that simple, low cost synthesis methods be used to obtain these materials. The work herein aimed at understanding the synthesis and electrochemistry of the Na-Ni-Mn-O and Na-Ni-Ti-O phase systems, as well as other select phases that allow for facile sodium-ion diffusion.

# LIST OF ABBREVIATIONS USED

| | |
|---|---|
| EV | Electric vehicle |
| XRD | X-Ray Diffraction |
| PVdF | Polyvinylidene fluoride |
| NMP | N-Methyl-2-Pyrrolidone |
| PC | Propylene carbonate |
| TMO | Transition metal oxide |
| M | Transition metal |
| SEI | Solid electrolyte interphase |
| LIB | Lithium-ion battery |
| NIB | Sodium-ion battery |
| BMF | Blown microfiber separator |

# ACKNOWLEDGEMENTS

# CHAPTER 1     INTRODUCTION

## 1.1 Context

The highest energy density secondary batteries used in consumer electronics and electric vehicles are currently lithium-ion batteries [1]. The reason for their success is their high energy density (~760 Wh/L) and their long cycle life (>1000 cycles). Lithium-ion batteries have revolutionized portable electronics since their introduction to the market by Sony in the early 1990s. As a result great efforts have been made at improving lithium-ion battery energy density, cycle life, and safety, while lowering their cost. Lithium-ion batteries are now becoming a mature technology. However, because of increasing energy demands of modern electronics and trends towards the electrification of automobiles, there is a great need for higher energy density and lower cost materials for energy storage.

Lithium-ion battery technology actually comprises a family of battery chemistries that employ various combinations of anode and cathode materials, each with varying structures. Each of the combinations offer advantages and disadvantages in terms of the following four metrics: safety, performance, cost, and lifetime. Often a battery may perform well in only some of these metrics, while performing poorly in the others.

Today modern lithium-ion batteries can hold more than twice as much energy by weight as the first commercial versions sold by Sony in 1991, and are ten times cheaper; however they could be nearing their energy limit. Most researchers think that further improvements in the energy of lithium-ion cells can achieve, at most, 30% more energy by weight [2]. The increase in the specific energy density since 1991 has been continuously provided by structural modifications and different anode and cathode combinations. The basic electrochemistry of lithium-ion batteries has remained essentially unchanged since

their introduction. Modern high energy density lithium-ion batteries typically still employ a form of a carbon based anode and a lithium transition metal oxide as they did originally. Intense research over the past few decades has not yet yielded a battery that can keep up with today's modern electronic technology and its accompanying high energy demands.

Despite the benefits that lithium-ion batteries bring in terms of energy density, there still remain questions regarding lithium-ion battery safety, cost, and poor low-temperature performance [3]. Additionally, if the use of large scale format lithium batteries becomes widespread, the price of lithium could be driven up with the increasing demand for lithium containing chemicals because lithium mineral reserves are considered to be geographically constrained [4,5]. This fact has driven researchers to search for more sustainable alternative energy storage solutions. Sodium-ion batteries have shown promise as an alternate battery chemistry to lithium-ion [6,7]. Sodium is more readily available (6th most abundant element in the earth's crust and there are large reserves in the world's oceans), has a potentially lower cost, could be more environmentally friendly than lithium, and innovative chemistries could yield high energy density materials. Moreover, sodium will not alloy with aluminum current collector foil at low voltages versus sodium. This result is advantageous as current collector foil is a major cost in battery cell production. Higher cost copper foil of the anode could be exchanged for low cost aluminum foil.

Intercalation compounds exist where sodium can be electrochemically intercalated reversibly in organic electrolytes [8], showing that sodium-ion cells are promising, although their energy density and cyclability must be increased for practical use. While still in its early stages sodium-ion battery research has the potential to yield unique and interesting results in the field of energy storage with respect to electrode materials.

2

## 1.2 Goals of this Work

This project aims at designing, synthesizing, and characterizing new sodium-ion based electrode materials for application in EVs. Layered structures were a primary target for these electrodes, as layered structures typically give good conduction of sodium ions and electrons. There are some important principles of design that should be discussed. At the materials level the cost is commonly determined by the abundance of the starting chemicals, reaction temperature and pressure, and the performance of the final product, however these are not the only factors. Figure 1.1 shows a periodic table that has been constructed as a guide to determine which materials from an elemental stand point would be suitable for battery materials.



Figure 1.1: Periodic table showing the elements available for the design of new battery electrode materials. Certain elements can be excluded due to their high cost, radioactivity, or toxicity.

The most influential factors for determining whether an element is appropriate for batteries are cost and performance (*i.e.* volumetric capacity) [9]. Weight is not deemed as significant for portable electronic and electric vehicle applications [10]. Therefore, the atomic weight which correlates to gravimetric capacity, is not taken into account here. Precious metals such as Au, Pt, and Rh can be excluded as incorporating these elements as

a major component of the battery would drastically increase the total cost of the battery cell. Of course if these expensive elements were used in small quantities as additives or dopants, to enhance the electrochemical properties of cells, it may be acceptable. Two dollars per gram was the boundary for eliminating elements according to cost. This cost, from Sigma-Aldrich [11], was per gram of the pure substance or common compounds such as carbonates, nitrates, or hydroxides of the element in question.

Other important cost factors were also taken into account while constructing this periodic table including the Herfindahl-Hirschman index, which is a measure of geopolitical influence of elemental production and element reserves [4,12]. The European restriction of hazardous substances is a good guideline for elements to exclude according to toxicity (elements include $Cr^{+6}$, cadmium, mercury, and lead) [13]. Other elements such as As and Be are also toxic and could cause safety concerns if distributed in batteries. The low natural abundance of other elements, such as Sc and Te, would make them impractical. Some elements can be eliminated by more than one factor, thus the color designation on the table is for the major factor. This eliminates a large portion of the periodic table. Even with a now limited number of elements, a vast number of combinations of potential materials are possible. It is important to note that even though some elements pose risks in terms of toxicity, they are sometimes still actively studied because of their superior performance and this is reflected in the table with two colors for some elements. This is the case with lead and certain oxidation states of the transition metals. The focus of this thesis is the creation of electrode materials from the most inexpensive and highest energy density positive electrode materials and, as with lithium-ion chemistry, sodium first row transition metal oxides are the most likely candidates.

4

Such materials combine high volumetric capacities, appropriate voltages and low cost. This project investigated the Na-Mn-Ni-O and Na-Ni-Ti-O phase systems and other transition metal oxides, with emphasis on facile and low cost synthesis. It is of significance that these systems contain elements that are deemed suitable for batteries in Figure 1.1. Specific compositions of interest within these systems were isolated for further evaluation as sodium-ion electrode materials. Both of the systems have materials with layered structures that are amenable towards sodium intercalation. It was a key goal of this work to find materials that could reduce cost and still have good performance, while being green and sustainable.

# CHAPTER 2        BACKGROUND

In this section lithium-ion batteries will be described. They can be seen as analogous to sodium-ion batteries due to similar chemistries resulting from being from the same group in the periodic table. This description will be followed by a description of the current state of sodium-ion positive and negative electrode materials as well as a discussion on layered type structures.

## 2.1 Lithium-ion Batteries

Mechanistically, sodium-ion batteries operate in an analogous way to lithium-ion batteries. This analogy can be made because they have similar charge storage mechanisms. Thus, lithium-ion battery chemistry, which is in common use, will be discussed herein to introduce the subject. Lithium-ion batteries consist of three main components: a positive electrode, a negative electrode and an electrolyte. Figure 2.1 shows a schematic diagram of a lithium-ion battery.
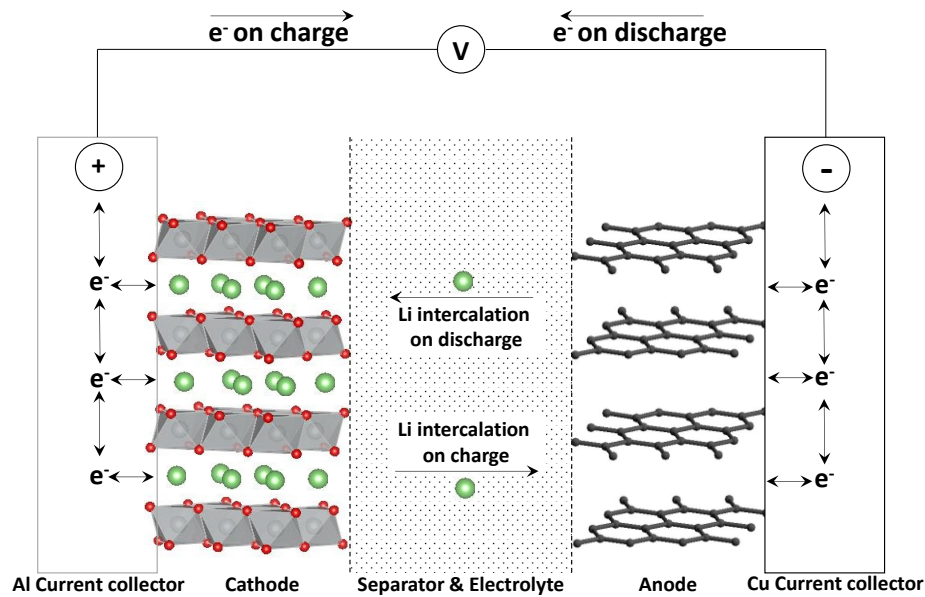
Figure 2.1: Schematic diagram of a Li-ion battery. A $LiMO_2$ cathode and graphite anode are shown. The green, red, and grey spheres of the cathode are lithium, oxygen, and transition metal ions respectively.

6

During discharge and charge, lithium ions are shuttled back and forth between the positive and negative electrode, respectively. This mechanism is often described as the rocking chair mechanism, as lithium rocks back a forth from one electrode to the other during the charge and discharge processes. The positive electrode is a material that initially contains lithium ions which can be removed electrochemically and at least one second element with multiple oxidation states. When lithium is removed electrochemically from the positive electrode an electron is removed while the second element oxidizes to maintain charge neutrality. Usually the positive electrode is an oxide, as the chemical potential of lithium in oxides is highly negative, resulting in high voltages of oxide cathodes versus lithium metal. The negative electrode is usually graphite that accepts electrons and lithium ions during charge (lithium ions can intercalate in its layered structure). The electrolyte is usually an organic solution of a lithium salt which provides lithium transport and diffusion between the positive and negative electrodes. There is additionally a separator which is typically a polymer membrane that allows the passage of ions while at the same time being electrically insulating, preventing short circuits between the positive and negative electrodes.

Often lithium-ion positive electrode materials are of two main crystal structures, namely layered and spinel oxides. Layered lithium transition metal oxides typically adopt a hexagonal structure with the general chemical formula $LiMO_2$. M stands for a single transition metal or a mixture of transition metals and dopants. The lithium spinels have a cubic structure with the general formula $LiM_2O_4$. With each structure a distinct set of Bragg peaks is observed when analyzed via X-ray diffraction (XRD). These peaks allow one to

obtain lattice parameters and atomic positions that describe the unit cell, and hence, the material's structure.  The chemical composition of the positive electrode has a significant effect on its functionality and properties, as different combinations of transition metals and dopants can change the capacity, voltage and thermal stability of constructed cells.

There are several limitations with lithium-ion technologies that limit its practical implementation in certain applications [14].  These include: cost, cycle life and safety.  Of these three the biggest issue is the cost, which is currently twice what is regarded as practical for electric vehicles.  Another issue is the ability for all the lithium reserves in the world to supply the automotive market, and to extract lithium ores without detrimental effects on the environment.  These results provide clear evidence of room for improvement when it comes to meeting the energy needs of storage materials.

## 2.2 Sodium-ion: An Alternate Battery Chemistry

Intense research has taken place in the field of lithium-ion battery technology and as of early 2014 only five cathode chemistries ($LiCoO_2$, $Li(NiMnCo)O_2$, $Li(NiCoAl)O_2$, $LiMn_2O_4$ and $LiFePO_4$) and two anode chemistries (graphite and $Li_4Ti_5O_{12}$) exist that are commercially utilized [1].  The lithium-ion idea is equally applicable to other metal-ion systems, making these systems promising areas for finding new practical battery chemistries.  Sodium-ion has shown potential as an alternate metal-ion battery chemistry, where lithium ions are simply exchanged for sodium ions.  Figure 2.2 shows a schematic of a sodium-ion battery using a layered sodium metal oxide for both the anode and cathode material, as well as aluminum foil for both current collectors.
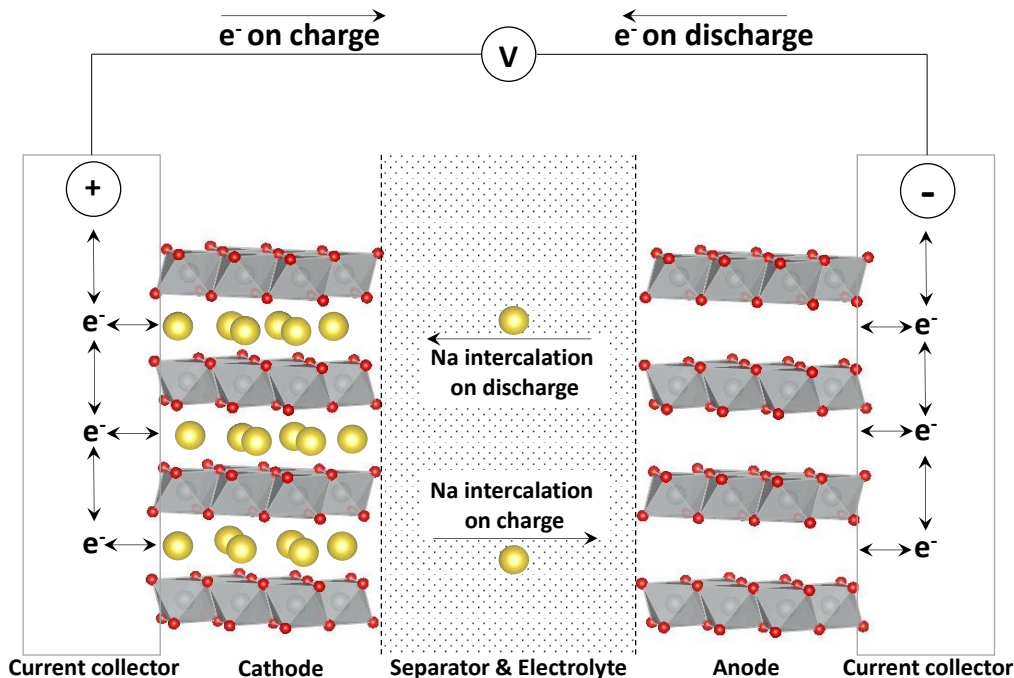
Figure 2.2: Schematic diagram of a Na-ion battery. A NaMO$_2$ layered phase is shown for both the cathode and anode. The yellow, red, and grey spheres of the electrodes are sodium, oxygen, and transition metal ions respectively.

There are apparent differences between lithium and sodium ions, however their chemistry is somewhat similar owing to the fact that they are in the same group of the periodic table. Perhaps the most substantial difference is their ionic radii: the radius of Na$^+$ is 1.02 Å and the radius of Li$^+$ is 0.76 Å, when their coordination number is six [15]. This larger ionic radius of sodium could pose challenges for sodium intercalation because of sterics.

While research in sodium-ion batteries is still considered very much exploratory at the moment, research actually began in the early 1980's but waned due the superior performance of lithium-ion materials. The reemergence of interest in sodium-ion batteries today is mainly due to the much higher natural abundance of sodium compared to lithium. The first studies of sodium-ion electrodes concentrated on NaMO$_2$ materials, where M =

transition metal. Much of this early work was performed at the Delmas lab in France [16] and has been revisited by in recent years by other researchers [17]. One such example is the $Na_xMnO_2$ system where in 1985 the Delmas group evaluated the two phases α- and β-$NaMnO_2$ as positive electrode materials [16]. Their results showed that only a small amount of sodium, 0.22 and 0.15 mole percent, could be reversibly intercalated from the α- and β-phases respectively using 1M $NaClO_4$ in PC as an electrolyte. The monoclinic α-$NaMnO_2$ was studied again in 2011 by the Ceder group at MIT and they were able to reversibly intercalate 0.8 of the sodium using 1M $NaPF_6$ in EC:DMC (1:1) electrolyte, which corresponds to almost 200 mAh/g capacity [17]. The success of the Ceder group versus the Delmas group was claimed to be due to the difference in electrolytes used. The development of practical negative electrode materials for Na-ion batteries has been much more difficult. Thus, research on sodium ion negative electrodes was not reported as early as that of the positive electrodes.

## 2.2.1 Cathode Materials for Sodium-ion Batteries

Cathode materials typically have a voltage greater than 2 V versus sodium metal. Material types that can function as cathodes in sodium-ion cells include: phosphates & sulfates (polyanion compounds), fluorides, sulfides, and oxides [8,18]. In the case of phosphates, the best known example is olivine structured $NaFePO_4$. Almost all of the sodium in this compound can be reversibly cycled with a gravimetric capacity of 140 mAh/g, however this material has a poor volumetric capacity owing to its low density [19]. Perhaps the best known intercalation electrode is $TiS_2$ [20]. Unfortunately the voltage versus sodium metal is 1.8 to 2.0 V which is not practical for either a cathode or anode.

By far the most extensively studied group of materials for positive electrodes is oxides, as is the case with lithium batteries. Layered $NaMO_2$ possess various crystal structures and display high voltages versus sodium metal. In 1981 the Delmas group demonstrated that sodium could be reversibly intercalated in $Na_xCoO_2$ with sodium half cells [21]. Since then most of the $NaMO_2$ oxides of the first row transition metals have been studied electrochemically: $NaCrO_2$ [22,23], $NaMnO_2$ [16,17], $NaFeO_2$ [24,25], $NaCoO_2$ [26], $NaNiO_2$ [22,27], and $NaCuO_2$ [28,29]. Most of these layered compounds allow only 0.5 of the sodium to be cycled from the structure with an average of 120 mAh/g or less capacity. Typically the voltage curves for these materials slope severely and have low average voltages, which is undesirable for practical applications. These values and characteristics for cathode materials need to be improved.

As with lithium layered materials, more recent studies have focused on sodium mixed transition metal oxide materials, where the occupants of the transition metal layer can be varied while maintaining stoichiometry and charge neutrality. This combining of transition metals can allow tuning of material properties, most notably voltage characteristics. The first example of this in sodium-ion electrode materials was $Na_xNi_{0.6}Co_{0.4}O_2$ in 1996 [30]. The Dahn group then reported in 2001 the $Na_{2/3}Mn_{2/3}Ni_{1/3}O_2$ material electrochemistry [31]. Since then many mixed transition metal oxides have been reported: $NaNi_{1/3}Mn_{1/3}Co_{1/3}O_2$ [32], $NaNi_{1/3}Fe_{1/3}Mn_{1/3}O_2$ [33,34], $NaFe_{1/2}Mn_{1/2}O_2$ [35–37], $NaFe_{1/2}Co_{1/2}O_2$ [38], $NaMn_{1/2}Co_{1/2}O_2$ [39], $NaNi_{1/3}Co_{1/3}Fe_{1/3}O_2$ [40], and $NaNi_{1/2}Mn_{1/2}O_2$ [41,42]. These materials tend to lead to an increase in average voltage and higher capacities compared to the $NaMO_2$ materials. In addition fewer phase transitions occur upon cycling which can be observed in the voltage capacity profile of these materials

which tend to have a single sloping plateau instead of multiple plateaus. Thus multiple transition metals or dopants help maintain the starting structure and allow more sodium to be deintercalated. These fewer transitions during cycling are indicative of greater structural stability and can lead to longer cycling life. These materials with high energy density based on abundant, low cost raw materials could enable commercial sodium-ion batteries, if paired with a practical anode material. However practical high energy density anode materials for sodium-ion batteries have been much harder to achieve thus far.

## 2.2.2 Anode Materials for Sodium-ion Batteries

Graphite is commonly used as an anode in lithium batteries [1]. It is easily compressed to low porosity in electrode coatings, has a high volumetric capacity density of about 700 Ah/L with lithium, a low average voltage versus Li metal (~150 mV) and excellent coulombic efficiency when appropriate electrolyte additives are used (~99.997%) [1]. Unfortunately, graphite does not intercalate sodium to any appreciable extent [43]. Hard carbon has been shown to reversibly intercalate sodium, but has a relatively low volumetric capacity of only 510 Ah/L [44–46].

Using metallic sodium as an anode material would be a poor choice as it poses safety concerns. It forms dendrites readily and is expected to become unstable towards thermal runaway during cycling. The temperature could quickly rise to the melting point of metallic sodium and cause a violent reaction. In group I of the periodic table the alkali metal reactivity increases down the group. Thus, sodium is more reactive with organic electrolyte solvents and has shown to have more extreme dendritic formation during cycling than lithium [47]. A lower melting point of 98 °C also poses a safety hazard for

devices designed to operate at room temperature. In this work sodium half-cells were used but a technique developed in the Obrovac lab was also used to limit dendritic growth by using BMF, in addition to Celgard, as a separator [48].

Non-carbonaceous anode materials for sodium ion batteries have also been studied. The lowest intercalation potential for sodium reported to date is that of $Na_2Ti_3O_7$, which has a capacity of 175 mAh/g at 0.3 V [49]. Unfortunately, these materials are white, as a result of not being good electron conductors, and large amounts of carbon black must be added which adversely affects the capacity. Conversion reactions of metal oxides can also be employed as anodes. The first reported was that of $NiCo_2O_4$ in 2002 [50] and have since reemerged with materials such as CuO [51]. CuO shows a first discharge capacity of 600 mAh/g most of which is realized below 0.6 V, however 250 mAh/g of this capacity is irreversible. This conversion reaction and others need to be improved as they have a large volume expansion and large hysteresis which leads to very poor cyclability. Alloy-based negative electrodes have also been investigated, but not extensively. The Obrovac group studied sodium insertion with tin and found that four distinct plateaus are present that gave 847 mAh/g capacity at full sodiation corresponding to $Na_{15}Sn_4$ [48]. Antimony has also shown better than expected cycling performance with sodium compared to Li [52]. 600 mAh/g capacity can be achieved corresponding to the $Na_3Sb$ phase upon full sodiation. This material has a large irreversible capacity, however it cycles better than the lithium counterpart. This issue is likely due to the intermediate phases being amorphous compared to lithium where intermediate phases are crystalline. More recent reports studied different types of phosphorus as high capacity anodes delivering over 1500 mAh/g [53,54]. The

largest hurdle to be overcome with all alloy materials is the fact that they display huge volumetric expansion during cycling which leads to poor cyclability.

The early transition metals, such as Ti and V, were not included as M in $NaMO_2$ when such cathodes were discussed above. This stems from the fact that they can be considered anode materials. The atomic radii of atoms decreases going from the left to the right of the periodic table. As the radius of the element becomes smaller, the electronegativity and ionization energies increase. The electronegativity of atoms in insertion electrodes is vital as it determines the ionic/covalent character of the metal ligand bonds and allows for tuning redox potentials. The ionization energy is important too as it directs the oxidizing/reducing power of the atom. It is easier to remove electrons which sit farther away from the core and leads to lower ionization energies. The 3d cations which possess the same charge have more oxidizing power from the left to the right of the periodic table, due to the decreasing atomic radius. All this together means that sodium removal from sodium early transition metal oxides tends to occur at lower voltages versus sodium (< 2 V). Scandium is too scarce to be used in electrode materials however titanium and vanadium have been studied as anodes. $NaTiO_2$ was first studied by the Delmas group and showed a sloping voltage plateau with an average voltage of 1.2 V versus sodium [55,56]. $NaVO_2$ has a higher voltage of about 1.7 V [57,58]. These voltages classify these as anode materials because their average voltage is < 2 V.

The studies done thus far show that sodium-ion batteries are feasible and may have advantages over lithium-ion [7,8,59]. These advantages could include lower cost, having an abundance of raw materials, and lower environmental impact. The goal herein is to achieve the cost advantages while minimizing any reduction in volumetric energy density.

Sodium-ion batteries are already being commercialized by a UK based company Faradion for certain applications [60].

## 2.3 Layered Structures for Sodium Intercalation

Materials with a layered structure are the focus of this research because they are good ionic conductors. This point is especially critical for sodium-ion materials as sodium has a much larger ionic radius than lithium. A specialized nomenclature to describe $AMO_2$ (A = alkali metal and M = transition metal) materials with layered structures was introduced by Delmas, Fouassier, and Hagenmuller in 1980 [61]. The nomenclature consists of a letter designating the coordination environment of the alkali metal and a number describing the number of transition metal layers in the unit cell. The letter can be either a P (prismatic) or an O (octahedral) in the case of sodium as the alkali metal. For lithium T (tetrahedral) coordination is also possible. The larger size of the sodium-ion prevents it from adopting tetrahedral geometry in layered transition metal oxides according to calculations done by the Ceder group [62]. However, there are instances where sodium is in tetrahedral sites, *e.g.* $Na_2O$. The larger size of sodium also makes it more prone to alkali metal ordering, but thus less prone to cation mixing with transition metals [62]. Therefore the transition metals are always of octahedral coordination in layered $NaMO_2$ oxides and oxygen are at the vertices of the octahedra. Monoclinic distortions commonly occur and are indicated by an apostrophe, as in O'3. Figure 2.3 shows the common P2, O3, and O'3 monoclinic structures.
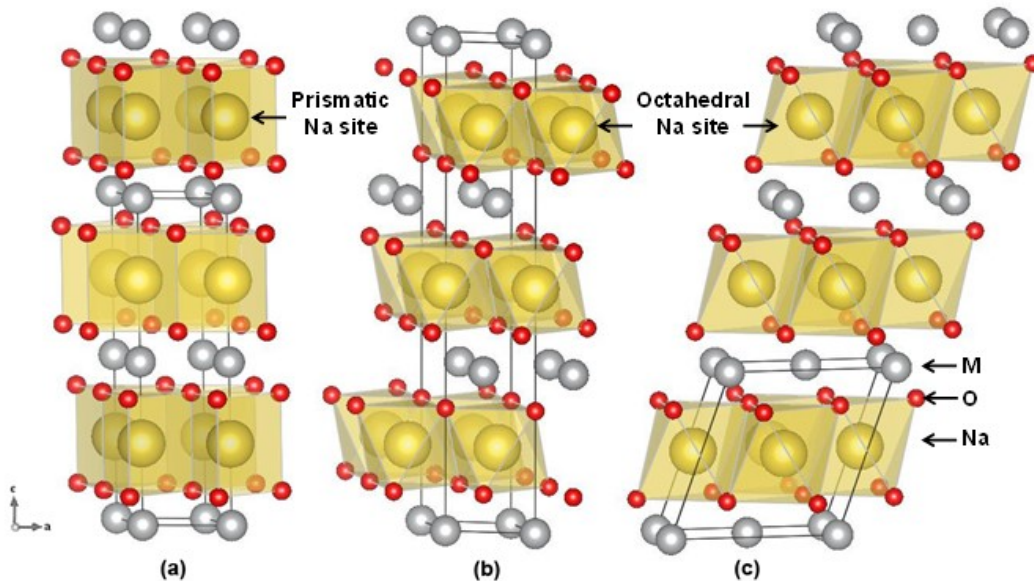
Figure 2.3: Common layered structures for sodium-ion batteries (a) P2, (b) O3, and (c) monoclinic or O'3.

Other common layered structures include O6, O2, and P3. Figure 2.4 shows the structural relationship between the lattice constants of the O'3 (monoclinic) and O3 lattice.
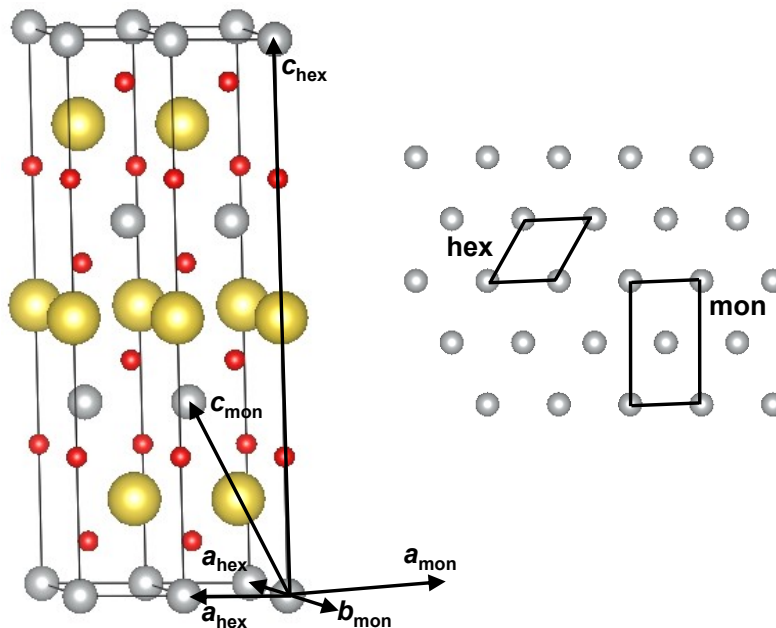


Figure 2.4: Structural relationship between layered O3 (hexagonal) and O'3 (monoclinic) crystal structures.

The O3 structure can become distorted to O'3 by either a slight gliding of the slabs in the $(a, c)$ plane which distorts the sodium sites or by a distortion of the $MO_6$ octahedra due to the Jahn-Teller effect [63].

# CHAPTER 3    EXPERIMENTAL METHODS

In this chapter the synthesis methods of the sodium-ion battery materials will be discussed, along with the process used for incorporating these materials into electrochemical cells. A brief overview of X-ray diffraction (XRD) and electron microprobe methods are also given as these specific characterization techniques have been extensively employed during the course of this research.

## 3.1 Preparation and Heat Treatment

Synthesis of the layered sodium mixed transition metal oxides was done via solid-state reactions. Precursors consisting of a sodium containing compound, which differed depending on the reaction and transition metal oxides used, were weighed out and thoroughly mixed using high energy ball milling in a SPEX 8000 ball mill. This high energy ball milling often causes the precursors to not only mix but react chemically as well. Minimal iron contamination is expected to be present in these samples due to milling in a hardened steel vessel, however this was not assessed. Precursors were milled for a typical period of a half hour to two hours in the ball mill. Generally, a 3:1 ball: sample mass ratio with a typical sample size of six grams and four stainless steel balls of half inch diameter were loaded into the milling vessel, under either inert argon atmosphere or air. Sometimes the powders were pressed into two gram pellets after SPEX milling. Milled powders or pellets were then directly transferred to an alumina boat and placed in a tube furnace equipped with a quartz tube that had fittings on each end to allow control of the gas flow and pressure. The samples were then fired at high temperatures (700 – 1000 °C) in different atmospheres (ambient air, argon, or oxygen) for differing amounts of time (10 – 24 hours). The exact synthesis method is reported in the results section for the individual materials

tested. The heating burns off all the carbon and hydrogen in the samples as carbon dioxide and water. The effect of different atmospheres can lead to different phases forming, as some are oxidizing while others are reducing. Water content in the air is an issue with these sample as most are hygroscopic. Increasing the oxygen partial pressure will avoid sodium loss at the high temperatures of synthesis.

The precursors used in the syntheses were: $Na_2CO_3$ (BioXtra, $\geq$ 99.0% Sigma Aldrich), $Na_2O_2$ (granular, + 140 mesh particle size, 97 %, Sigma-Aldrich), $Na_2O$ (80 %, Aldrich), NiO (-325 mesh, 99 % Alfa Aesar), $Mn_2O_3$ (-325 mesh, 99 %, Sigma Aldrich), $MnO_2$ (*ReagentPlus*®, 60 to 230 mesh, $\geq$ 99%, Sigma Aldrich), $Fe_2O_3$ (powder, <5 μm, $\geq$99%, Sigma-Aldrich), CoO (-325 mesh, Sigma Aldrich), and $TiO_2$ (puriss, 99 to 100.5 %, Sigma-Aldrich). An excess amount of the sodium containing precursors, usually 5 to 10 % weight, was added to compensate for the loss of sodium due to the volatility of sodium containing precursors at the high reaction temperatures. For this reason the stated sodium compositions of these samples are nominal. After heat treatment the samples were either slow cooled or rapidly cooled to room temperature under gas flow by removing the tube from the furnace or quenched in liquid nitrogen to achieve the desired phase of the material. All samples were transferred directly to an argon filled glovebox while still in the furnace tube after the heating step to avoid air exposure, as the samples were found to be hygroscopic. Even those samples heated in air were removed at 200 °C and transferred to an argon glovebox, to avoid water contamination.

## 3.2 X-ray Diffraction

The main technique utilized in this research to characterize material structure was XRD. XRD is a very versatile, non-destructive technique that reveals detailed information

19

about the chemical composition and crystallographic structure of materials [64]. X-rays were discovered by Wilhelm Roentgen in 1895 and thereafter in 1913 these rays were exploited by the Braggs, a father and son duo, applying them to crystals as a characterization technique. This application was made possible by the fact that X-rays wavelengths are on the scale of the atomic spacing in crystals; 0.1 to 100 angstroms.

In simple terms a crystal structure can be described by its unit cell. The unit cell is a regularly repeating unit that can defines the entire bulk crystal structure. The unit cell dimensions can be described by three lattice constants and three lattice angles. These different lattice constants and angles lead to fourteen types of lattices, referred to as the Bravais lattice types. Atoms exist within this framework of a unit cell and are described by their atom positions in terms of the unit cell axes. XRD can be used to identify crystal structures and can reveal whether multiple lattice types or structures are present in a given sample. The occurrence of multiple phases was the main issue when employing the solid-state synthesis method herein.

## 3.2.1 X-ray Generation

For an XRD experiment to be performed X-rays must first be generated. The generation of X-rays is accomplished by electrons that are emitted from a heated filament and then accelerated in a vacuum by a high electric field, on the order of tens of kilovolts, towards a metal anode (a copper anode was used here, other metals such as molybdenum are typical as well). These incident electrons are of such high energy that they interact with the electrons of the metal, knocking them out of the inner shells. This allows higher energy electrons to "drop down" into a lower energy level and fill the void that was left. The

dropping down in energy level results in an emission of energy in the form of X-ray radiation as shown in Figure 3.1.
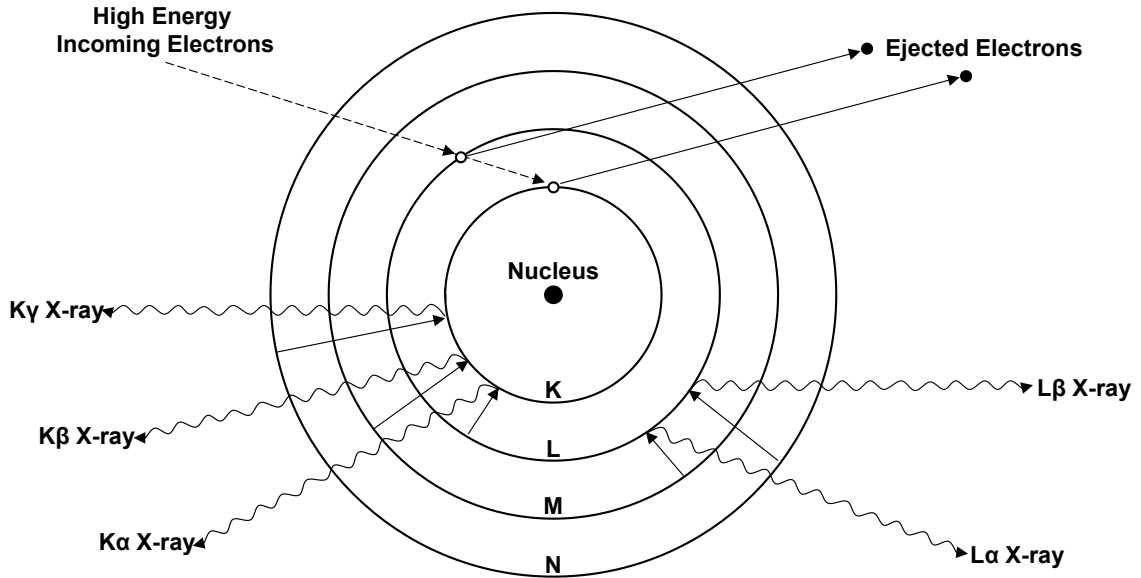


Figure 3.1: X-ray radiation generated by incident electrons.

A particular wavelength emission is selected by a monochromator. For our experiments Cu Kα radiation was used. It contains two wavelengths, a strong emission (K$\alpha_1$ at 0.154056 nm) and a weaker emission, by exactly two times (K$\alpha_2$ at 0.154439 nm) [64]. Peaks resulting from the diffraction of both of these wavelengths are present in well-resolved diffraction patterns.

## 3.2.2 Bragg Diffraction

Incident X-ray radiation, once generated, is applied to a sample that often possesses a crystal structure or lattice, however amorphous and liquids can also be studied. A crystal lattice is a regular three-dimensional distribution (cubic, rhombic, monoclinic, etc.) of atoms in space. The lattice of atoms can be thought of as residing in a series of parallel planes separated from one another by a distance $d$. This distance will vary according to the

structure of the material. Planes can and do exist in a number of different orientations for any crystal, each with its own specific *d* spacing. These *d* spacings are on the same order of magnitude as the wavelength of incident X-ray radiation, which causes these waves to diffract. The resulting diffraction pattern helps one to determine the exact structure of a sample. The structure determination is possible with the use of Bragg's Law, which is depicted in Figure 3.2.
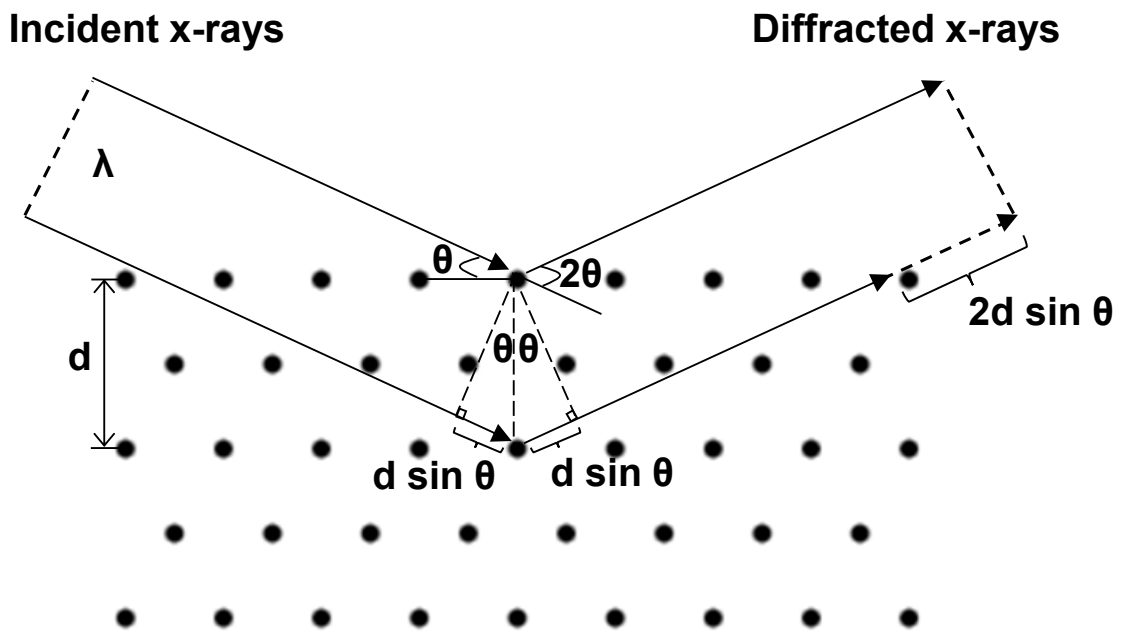


Figure 3.2:  Bragg Diffraction from lattice planes in a crystal structure.

X-rays can be scattered from the top plane of a crystalline material or be transmitted through the sample to be scattered by planes that are deeper in the structure. This causes the beam reflected from the sample to have multiple phases that can interfere destructively or constructively with one another. The interference depends on the distance of the lattice spacing. This can be summed up using the equation for Braggs' Law,

$$2\,d\,\sin\theta = n\,\lambda,$$

where $n$ is an integer, $\lambda$ is the wavelength of the incident wave of X-rays, $d$ is the spacing between the planes in the crystal lattice, and $\theta$ is the angle between the incident X-rays and the diffracting planes. A diffraction pattern is obtained by measuring the intensity of scattered X-ray waves as a function of scattering angle. Very strong intensities known as Bragg peaks are obtained at specific scattering angles in the diffraction pattern when scattered waves satisfy the Bragg condition. These Bragg peaks allow the plane spacing, $d$, to be determined. For example Braggs' law can be used to obtain the lattice spacing of a particular simple cubic system through the following relation,

$$d = \frac{a}{\sqrt{h^2 + k^2 + l^2}}$$

where $a$ is the lattice constant of the unit cell of the cubic crystal and $h$, $k$, and $l$ are the Miller indices of the specific Bragg plane. Miller indices are a notation system in crystallography that consists of three integers which describe the group of planes in question. The $h$, $k$, and $l$ values are actually the reciprocal of the fractional coordinates where the plane intercepts the $x$, $y$, and $z$ axes. There are similar but more complex relations for all other crystal structure types [64].

The obtained experimental XRD pattern can also be compared to a database for phase determination (qualitative analysis). Further characterization can be done using Rietveld refinement, a technique developed by Hugo Rietveld in 1967, which uses a least squares approach for quantitative analysis. This approach takes a theoretical line profile

23

and changes it incrementally until it matches as closely as possible the measured or experimental profile. This allows for the determination of precise crystallographic structural information, such as atom positions, lattice constants, and site occupations. A powder XRD calculation of the total peak intensities, $I$, takes into account five factors as follows,

$$I(\theta) = I_0 \, P(\theta) \, L(\theta) \, F^2(hkl) \, M(hkl) DW(hkl)$$

(3.3)

where $I_o$ is the intensity of the incident radiation, $P(\theta)$ is the polarization factor, $L(\theta)$ is the Lorentz factor, $F^2(hkl)$ is the geometric structure factor, $M(hkl)$ is the multiplicity factor, and $DW(hkl)$ is the Debye-Waller factor [65]. These take into account the $\theta$ dependence of the peak intensity (both polarization and Lorentz factor), the interference between atoms within the unit cell, families of planes which have the same $d$-spacings, and the thermal vibration of atoms respectively [64]. All Rietveld refinement done in this work used the computer program Rietica to fit experimental data [66]. This program is available for free download online. Structures were also visualized in another computer program called Vesta and all figures depicting crystal structures were drawn using Vesta [67].

## 3.2.3 X-ray Diffraction Measurements

The crystallographic structures of the samples were determined by analysis with a Rigaku powder diffractometer X-ray system equipped with both a scintillation and linear detector. The scintillation detector with a diffracted beam monochromator was used to measure XRD patterns of powder samples and *ex situ* XRD samples of electrodes. A D/TeX Ultra linear detector with K-beta filter was used for *in situ* XRD measurements. A

second diffractometer, a Siemens D500 powder diffractometer, was also sometimes employed for the work with powder samples. Both are equipped with a Cu target X-ray tube and a Bragg-Brentano θ:2θ geometry. A filament current of 30 mA and an accelerating voltage of 40 kV were typically used to generate the X-rays. For XRD measurements, because most of the powder samples were hygroscopic they were loaded into a gas tight X-ray sample holder (DPM Solutions, Hebbville NS). Figure 3.3 shows the air sensitive sample X-ray holder.
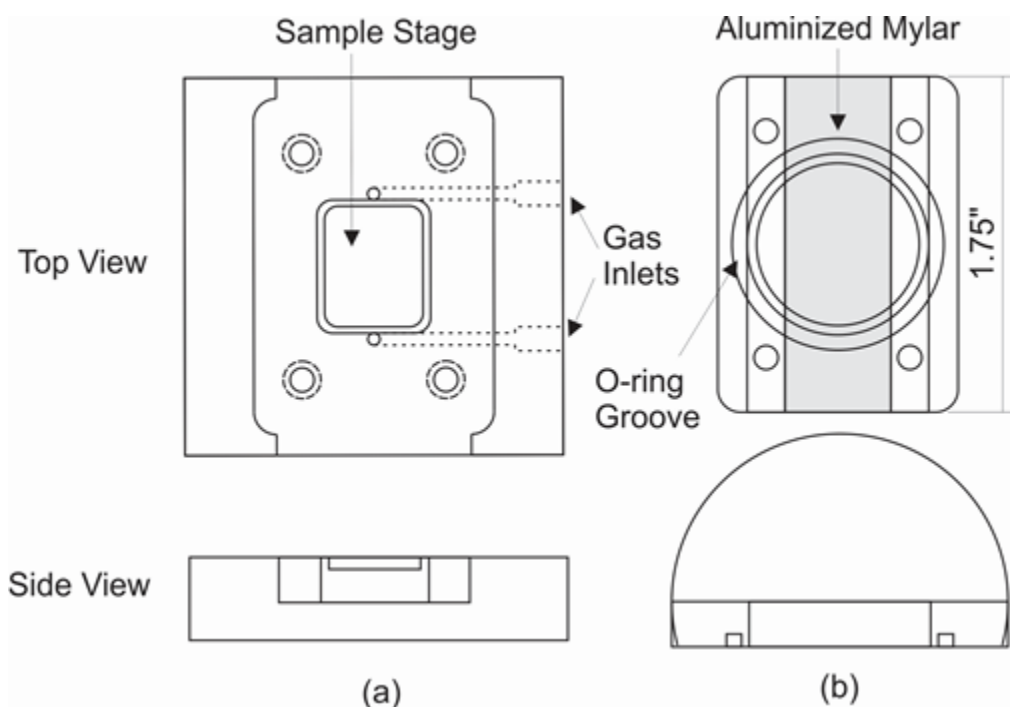


Figure 3.3: The gas tight X-ray sample holder with a top and side view of both the base (a) and the cap (b) that were held together with an O-ring and four hex screws. The cap has an aluminized Mylar window that allows X-rays to penetrate.

The sample holder had an aluminized Mylar window mounted in an arc such that it was perpendicular to the incident and scattered X-ray beam and did not contribute to the measured XRD patterns. A continuous flow of helium gas was provided through the sample holder via quick connect fittings during diffraction measurements to increase

25

counts.  X-ray diffraction spectra were collected for each sample at a typical scattering angle range of 10 to 80 degrees with a step of 0.05 degrees and a ten second dwell time.

## 3.3 Electron Microprobe Measurements

An electron microprobe was often utilized to further characterize samples that were produced.  An electron microprobe is used to non-destructively determine the chemical composition of small sample sizes, in this case crystalline powders.  The synthesized samples were bombarded with a beam of high energy electrons (5 – 30 keV).  The high energy electrons interact with the electrons of the atoms in the powder sample and cause X-rays to be emitted at wavelengths characteristic of the elements being analyzed (like the Cu target used for X-ray generation). The different energies of the X-rays can provide the identification of the atoms whereas the intensities of the specific X-rays is related to the concentrations of the different elements present.   This allowed both the identification and abundances of elements present within the small powder sample spots to be determined. The electron microprobe analysis is therefore both a qualitative and quantitative study tool.

A Phenom G2-pro scanning tabletop electron microscope (SEM, Nanoscience, Arizona) was used to determine particle size and morphology of the powder samples from images.  Using the SEM posed several challenges when powder samples were analyzed. Sample mounting can be difficult and special techniques using double sided carbon tape had to be employed to get a flat sample and avoid loose powder.  The sample must also be sufficiently conductive to avoid the charge effect, which can cause images to be extremely distorted.  Often a thin film of a highly conductive metal is used for this purpose to carry

excess charge away from the specimen.  As a result of these challenges the SEM data can have a significant errors associated with them.

## 3.4 Electrode Fabrication

Once the synthesized powders were characterized via XRD and electron microprobe analysis they were made into composite electrodes for further testing. Electrodes were made in an argon atmosphere by combining the active material, a carbon black conductive diluent (Super P, Erachem Europe), and a PVdF binder (polyvinylidene fluoride, Kynar HSV 900) in an 8:1:1 weight ratio.  An adequate amount of N-methyl-2-pyrrolidone (Sigma Aldrich, anhydrous 99.5%) was added to the components until a desired viscosity was achieved.  The mixture was then thoroughly mixed with two tungsten carbide balls in a Retsch PM200 rotary mill (100 rpm, 1 hour) to create a uniform black slurry.  The slurry was then coated onto aluminum foil using a 0.006 inch spreader bar and dried under vacuum at 120 °C for two hours.  Circular electrodes, area 2 cm$^2$, were punched from the resulting coatings.

## 3.5 Electrochemical Studies

The performance of synthesized materials for application in sodium-ion batteries was analyzed using half-cell type coin cells with a Maccor cycler.  Coin cell preparation was carried out in an argon filled glove box.  For the negative electrode, thin sodium metal disks were used.  These disks were punched from thin foil that was rolled from a sodium ingot (Sigma Aldrich, ACS reagent grade), since sodium foil is not readily available. The surface of sodium ingot, was first scraped clean in an argon filled glovebox to remove the

outer oxide coating. A small ingot was then placed in a plastic bag and passed through a PEPE Tools® foil roller multiple times, as the roller distance was decreased. This was repeated until the roller distance, as measured by a feeler gauge, corresponded to a foil thickness of approximately 0.015 inches.

The electrolyte used was 1 M $NaPF_6$ (Sigma Aldrich 98%) dissolved in propylene carbonate (Novolyte Technologies). Two Celgard 3501 and one BMF (blown microfiber separator, 3M Company) were used as separators. BMF was used to improve cycling over Celgard® separator alone by simultaneously increasing the distance between electrodes, while providing a more even stack pressure. Figure 3.4 shows the components of the sodium half-cell.
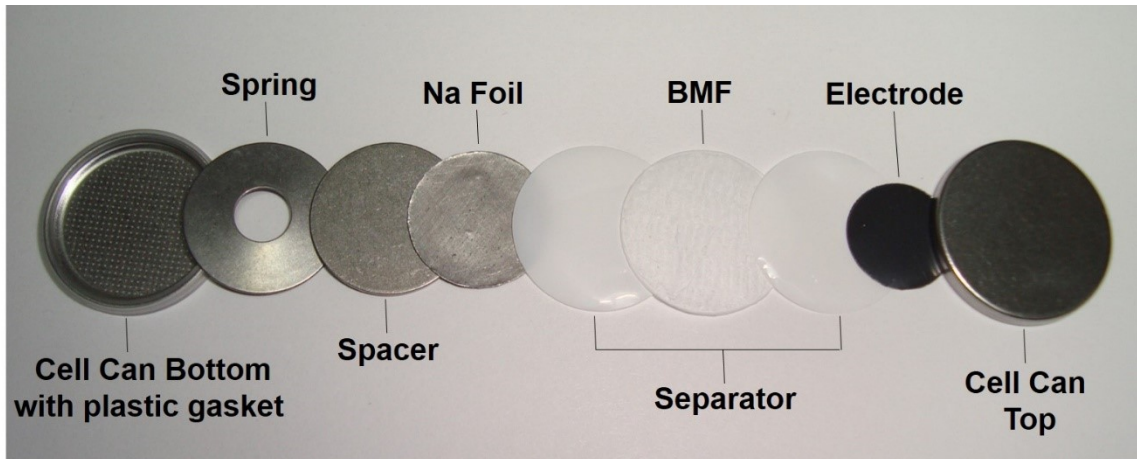


Figure 3.4: Sodium coin cell assembly.

Cells were tested on a Maccor Series 4000 Automated cycler and were cycled at 30 °C at a constant current of C/10, calculated based on the capacity for each separate active material. Cycling was done for different voltage windows, depending on the electrode material. Low voltage cycling was typically done from 5 mV to 2 V and high voltage cycling from 2 V to 4.3 V.

# CHAPTER 4      CATHODE MATERIALS BASED ON $NaNi_xMn_{1-x}O_2$

# $(0 \leq x \leq 1)$

## 4.1 Introduction

The $NaNi_xMn_{1-x}O_2$ ($0 \leq x \leq 1$) system was studied for use as cathode materials in sodium-ion battery applications. The motivation for studying this series was that mixed transition metals can potentially avoid multiple plateaus and $NaMO_2$ with M = Ni or Mn should have high voltages versus sodium metal. These transition metals are also deemed suitable for batteries from the periodic table constructed in Chapter 1.

As mentioned in the introduction, the $NaMO_2$ type oxides generally form layered structures quite easily due to the large ionic size of $Na^+$, which reduces electrostatic repulsion between the oxide layers [68]. This is not always true in the case of $LiMO_2$ oxides, which can be susceptible to cation mixing or conversion to spinel structures. For example, the analogous layered $LiNi_{0.5}Mn_{0.5}O_2$ has been studied as a cathode material for lithium-ion batteries, however it suffers from cation mixing [69–71]. This is due to the similarity of ionic size of $Li^+$ and $Ni^{2+}$ [15]. However, in $NaNi_xMn_{1-x}O_2$ cation mixing between sodium and the transition metals does not occur, as sodium has a significantly larger ionic radius than the transition metal ions, making cation mixing energetically unfavorable. Due to the extra stability of layered $AMO_2$ oxides with large alkali metal cations (A), they can often accommodate significantly more deficiency in the alkali metal layer, when A is not lithium [68]. This allows such materials to have a high capacity while still maintaining their structural integrity. The effect of structural stability is amplified when more than one transition metal is incorporated in the M layer and higher capacities are obtainable [40].

29

A number of studies have investigated compositions that fall within the $NaNi_xMn_{1-x}O_2$ series and their use as cathodes in sodium ion batteries, however no systematic study of this system has been reported. Parant et al. studied the structures of $Na_xMnO_2$ (x = 0.2, 0.40, 0.44, 0.70, 1) made by solid-state methods [72]. $NaMnO_2$ was found to form a low temperature monoclinic $\alpha$-$NaMnO_2$ phase (which is denoted here as O'3 $NaMnO_2$), and a high temperature orthorhombic phase ($\beta$-$NaMnO_2$). Mendiboure et al. investigated the structural transitions induced by electrochemical desodiation of $NaMnO_2$ bronzes in 1M $NaClO_4$ in PC electrolyte [16]. They found that for $Na_{0.70}MnO_2$ the P2 structure is maintained from $0.45 \leq x \leq 0.85$, while both the O'3 $\alpha$-$NaMnO_2$ and $\beta$-$NaMnO_2$ show two structural transitions during cycling. Ma et al. measured the electrochemical performance of O'3 $NaMnO_2$ in 1M $NaPF_6$ in EC:DMC electrolyte [17] and obtained significantly higher capacities compared to Mendiboure et al. The voltage curve of O'3 $NaMnO_2$ was found to comprise many pronounced features with strong voltage steps and plateaus indicative of phase transitions. The sequence of phase transitions during charge and discharge were found not to be the same, indicating that the charge and discharge processes go through different reaction paths. However, this hysteresis was found to be reversible. After 20 charge/discharge cycles 132 mAh/g capacity was retained from a 185 mAh/g first discharge capacity [17].

The electrochemistry of O'3 $NaNiO_2$ has been studied by Braconnier et al. in 1M $NaClO_4$ in PC electrolyte [22]. Only 0.2 Na could be removed during electrochemical desodiation. Recently Vassilaras et al. reinvestigated the electrochemistry of O'3 $NaNiO_2$ in 1M $NaPF_6$ in EC:DMC electrolyte and achieved a reversible discharge capacity of 120

mAh/g (corresponding to the removal of about 0.5 Na) [27]. The voltage curve of O'3 NaNiO$_2$ was found to comprise a number of plateaus which are completely reversible.

Paulsen and Dahn studied the layered manganese bronzes, Na$_{2/3}$[Mn$_{1-x}$M$_x$]O$_2$ with the P2-structure [73]. Na$_{2/3}$[Mn$_{1-x}$Ni$_x$]O$_2$ could be made phase pure at compositions up to x = ⅓. Higher nickel contents resulted in phases coexisting with NiO. It was reasoned that this behavior could be understood if Ni$^{2+}$ replaces Mn$^{3+}$ to make Na$^+_{2/3}$[Mn$^{3+}_{1-3x}$Mn$^{4+}_{2x}$Ni$^{2+}_x$]O$_2$, then the composition limit is reached at x = ⅓. For compositions with x < 1/5, the oxidation state of Mn is less than 3.5, which results in an orthorhombic distortion of the P2 structure due to the co-operative Jahn-Teller effect. At compositions with x > 1/5, an undistorted P2 structure was obtained.

Lu and Dahn studied the electrochemical extraction and insertion of sodium in P2-Na$_{2/3}$Ni$_{1/3}$Mn$_{2/3}$O$_2$ by *in situ* x-ray diffraction [31]. They found that the Na can be completely extracted from this material and reversibly inserted again. When x > 1/3 the structure is P2. At x = 1/3 a small amount of O2 structure is observed. For x < 1/3 the structure adopts the P2 structure, with some minor O2 and Ni$_{1/3}$Mn$_{2/3}$O$_2$ phases also present. O3 NaNi$_{1/2}$Mn$_{1/2}$O$_2$ has been studied extensively by Komaba et al. [41,42,74]. This material has a first discharge capacity of 185 mAh/g, between 2.2 − 4.5 V and a density of 4.59 g/mL. This corresponds to a volumetric energy density of 2700 Wh/L vs Na, which is similar to the energy density of LiNi$_{1/3}$Mn$_{1/3}$Co$_{1/3}$O$_2$ vs Li. However, the reversibility of O3 NaNi$_{1/2}$Mn$_{1/2}$O$_2$ cycled in this voltage range is poor. If the upper voltage window is narrowed to 3.8 V then 125 mAh/g is achieved with good capacity retention. During cycling the O3 starting material changes to the O'3, P3, P'3, and then P3" structures.

The high capacities and stable cycling obtained in cathodes containing Ni and Mn make such electrodes attractive for use in commercial applications. To more fully explore the properties of these materials a synthetic, structural and electrochemical study of the entire $NaNi_xMn_{1-x}O_2$ ($0 \le x \le 1$) system is needed, and was undertaken herein. Using a number of synthetic conditions, it was found that phase pure materials could only be obtained for $x = 0$, $0.25 \le x \le 0.66$ and $x = 1$. The phases obtained during synthesis depended strongly on the precursor materials and the oxygen partial pressure during the heating step. This is the first report of the single-phase oxides where $x = 0.25$ and $x = 0.66$. The electrochemical performance of phase pure materials was evaluated in sodium cells. These materials were found to reversibly intercalate sodium and have a high tolerance towards sodium vacancies, leading to high gravimetric capacities and energy densities.

## 4.2 Synthesis of the Layered Oxides

$NaNi_xMn_{1-x}O_2$ materials were prepared via solid-state reactions. Phase pure samples proved difficult to produce. Upwards of 300 samples were synthesized in order to determine synthesis conditions that would give phase pure samples. It was found that the synthesis conditions strongly affected the phases obtained, including the precursor material composition, the mixing and/or grinding method, powder preparation (pelletization), heating temperature, heating atmosphere, and quenching rate. The precursors used in these syntheses were: $Na_2CO_3$ (BioXtra, $\ge 99.0\%$ Sigma Aldrich), NiO ($-325$ mesh, 99 % Alfa Aesar), $Mn_2O_3$ (-325 mesh, 99 %, Sigma Aldrich), $MnO_2$ (*ReagentPlus*[®], 60 to 230 mesh, $\ge 99\%$, Sigma Aldrich), and $Na_2O_2$ (granular, + 140 mesh particle size, 97 %, Sigma-Aldrich). This method differs from previous reports, which used mixed transition metal hydroxides as precursors [31,42]. As mentioned previously

an excess amount of the sodium containing precursors (usually 10 % weight) was added to compensate for the loss of sodium due to its volatility at the high reaction temperatures.

Different precursor combinations and heating conditions were found to be the most effective for obtaining phase pure samples, depending on the composition range in $NaNi_xMn_{1-x}O_2$. For $0 \leq x \leq 0.05$, $Na_2CO_3$, $NiO$, and $MnO_2$ were ball milled for a half hour and the powder was then fired at 800 °C in argon for 10 hours. For $0.25 \leq x \leq 0.66$, $Na_2CO_3$, $NiO$ and $Mn_2O_3$ were ball milled for one hour and pelletized before heating in air at 850 °C for 24 hours, followed by quenching in liquid nitrogen. Samples with compositions in the range of $0.95 \leq x \leq 1$ used $Na_2O_2$, $NiO$ and $Mn_2O_3$ as precursors that were ball milled for a half hour and then fired in oxygen at 700 °C for 12 hours. Table 4.1 summarizes the three synthesis methods that resulted in phase pure products for the various composition ranges. These synthesis methods will be referred to as Method A, B and C, as denoted in Table 4.1. After synthesis the samples were transferred directly in an argon filled glovebox to avoid air exposure, as the samples were found to be hygroscopic. All subsequent powder handling (X-ray measurement, electrode and coin cell preparation) was performed under an inert atmosphere.

Table 4.1 Synthesis conditions that were utilized to produce pure phase $NaNi_xMn_{1-x}O_2$ samples.

| Method | precursors | atmosphere | Annealing temperature (°C) | Annealing time (hours) |
|--------|-----------|------------|-------------|-------------|
| A | $Na_2CO_3$, $NiO$, $MnO_2$ | Argon | 800 | 10 |
| B | $Na_2CO_3$, $NiO$, $Mn_2O_3$ | Air | 850 | 24 |
| C | $Na_2O_2$, $NiO$, $Mn_2O_3$ | Oxygen | 700 | 12 |

Figure 4.1 shows an SEM image of $NaNi_xMn_{1-x}O_2$ with $x = 2/3$, which is typical of the samples made here.  The primary particles have a thin hexagonal plate like morphology and are about 1 to 2 μm in size.
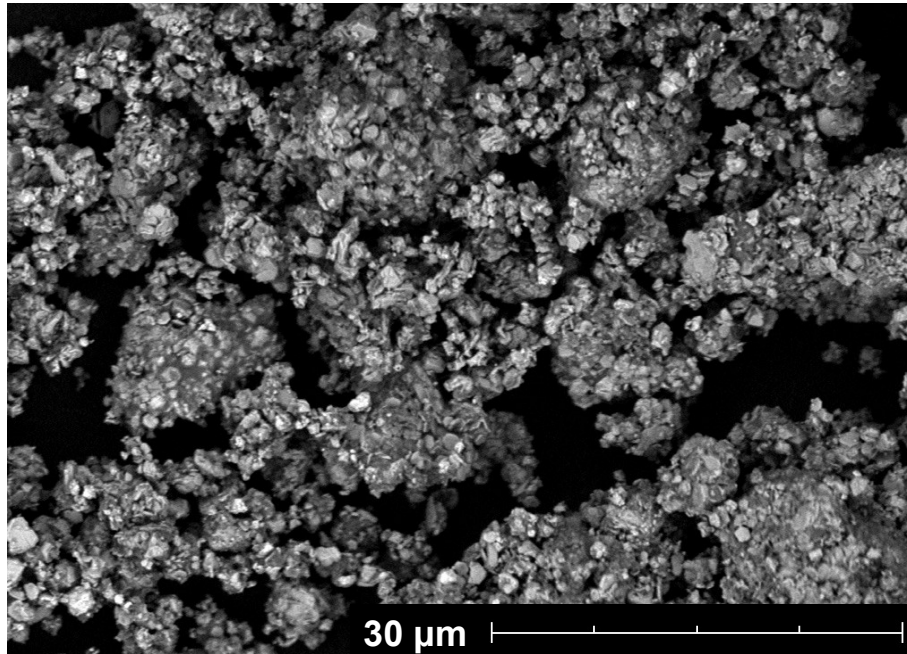


Figure 4.1 SEM image of $NaNi_{2/3}Mn_{1/3}O_2$, showing particle size and morphology.

Figure 4.2 to Figure 4.4 show the XRD patterns of samples prepared by methods A, B and C, respectively.  All diffraction patterns of layered phases could be refined using either a monoclinic (O'3 type, C2/m), rhombohedral (O3 type, $R\bar{3}m$) or hexagonal (P2 type, $P6_3/mmc$) space group.  In some cases a NiO impurity was detected as peaks near 43°. XRD patterns indicative of phase pure samples are highlighted in Figure 4.2 to Figure 4.4.
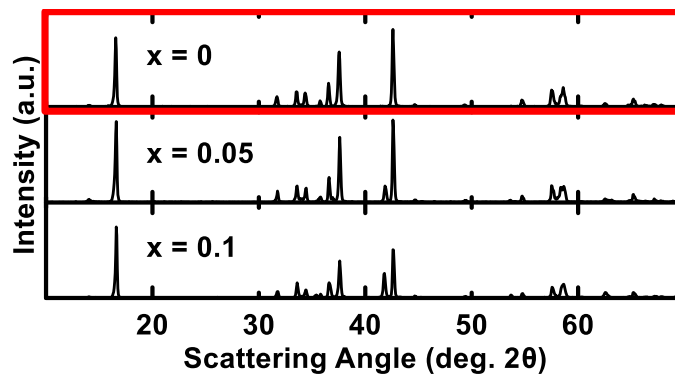
Figure 4.2 X-ray diffraction patterns for samples prepared by method A. The red box highlights phase-pure samples.
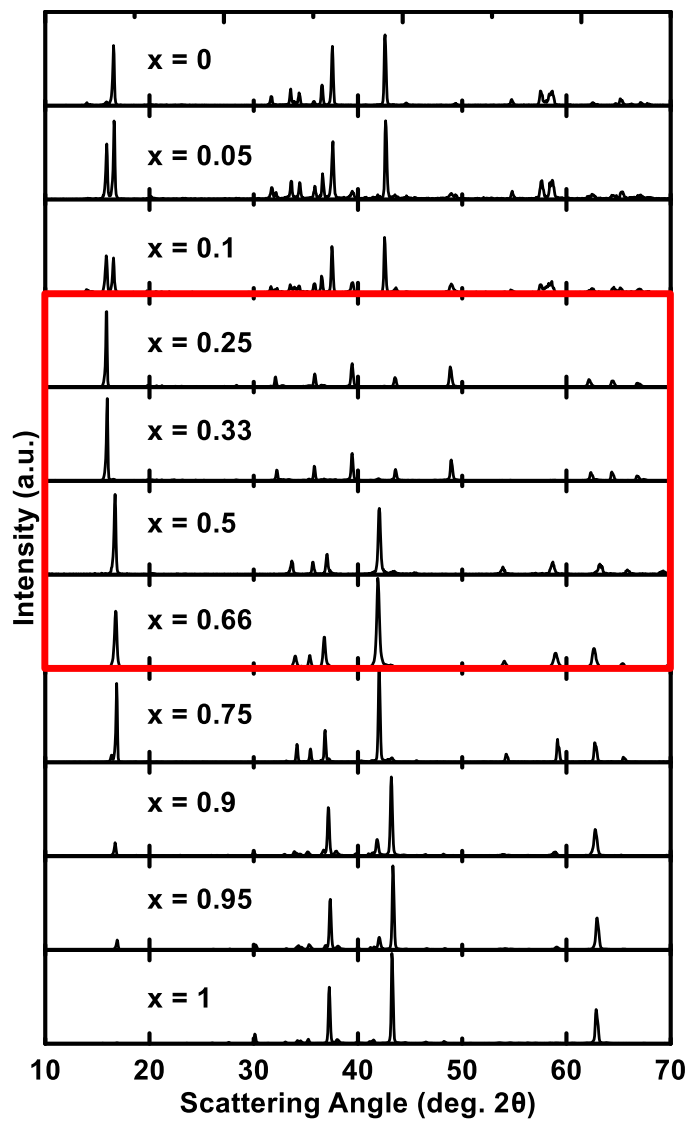


Figure 4.3 X-ray diffraction patterns for samples prepared by method B. The red box highlights phase-pure samples.
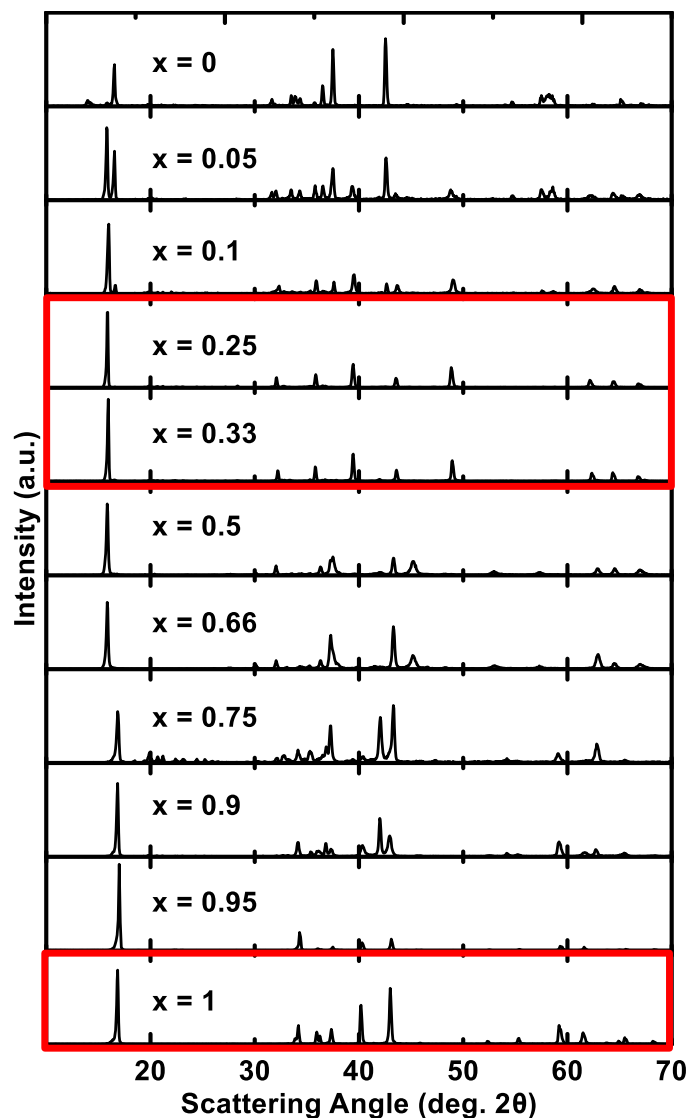
Figure 4.4 X-ray diffraction patterns for samples prepared by method C. The red box highlights phase-pure samples.

Figure 4.5 summarizes the phases observed for samples prepared by methods A, B and C as a function of x in $NaNi_xMn_{1-x}O_2$. Method A was the only method used that resulted in phase pure O'3 $NaMnO_2$, as shown in Figure 4.2. However, this method did not result in phase pure samples for x > 0. Instead, increasing the nickel content in the range of $0.05 \leq x \leq 0.25$, led to a monoclinic structure mixed with a distorted P2 structure.
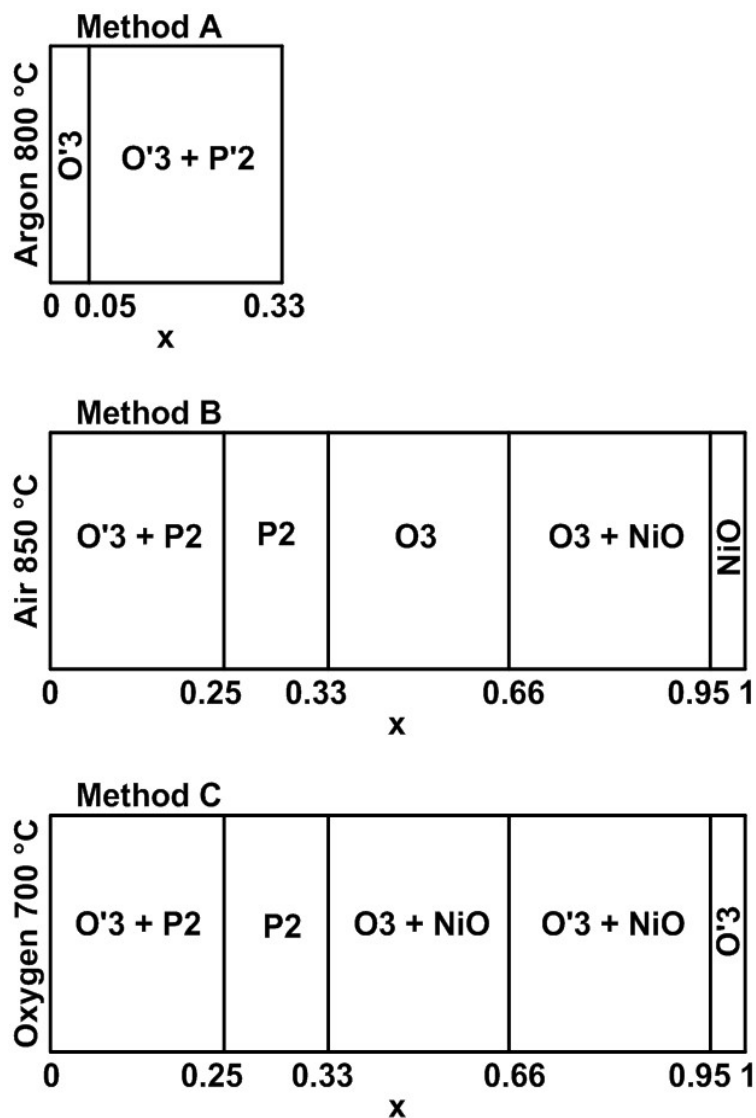
Figure 4.5 A pseudo-binary phase diagram of the $NaNi_xMn_{1-x}O_2$ system, for samples prepared by the three synthesis methods as indicated in Table 4.1.

Method B resulted in phase pure samples having the P2 structure for $0.25 \leq x \leq$ 0.33, as shown in Figure 4.3. In addition, phase pure samples having the O3 structure were obtained for x = 0.5 and 0.66. Samples with higher nickel content contained increasing amounts of NiO in addition to the O3 phase. When x = 1 only a NiO phase was present. This result is likely a consequence of significant sodium evaporation, in the form of sodium oxide, from the sample / precursors during the heating step in air. Sodium evaporation is

related to the synthesis temperature and length of heating time. Higher synthesis temperatures are needed for product formation, however when temperatures of 900 °C or above are used significant sodium evaporation occurs and a NiO phase is observed.  If longer heating times (> 24 hours) are used sodium evaporation is also increased and in many cases no ordered layered phases are formed.

When samples were prepared using method C, phase pure samples having the P2 structure were obtained for $0.25 \leq x \leq 0.33$, as shown in Figure 4.4.  Phase pure O'3 $NaNiO_2$ of the O'3 type was also obtained when $x = 1$.  Method C was the only method used that resulted in phase pure O'3 $NaNiO_2$.  Outside these composition ranges, method C did not result in phase pure samples.  Samples with $0.33 < x < 0.66$ consisted of a mixture of O3 $NaNi_xMn_{1-x}O_2$ and NiO, while samples with $0.66 < x < 1$ consisted of O'3 $NaNi_xMn_{1-x}O_2$ and NiO.  The phase boundary at $x = 0.66$ is bothersome as NiO is observed on either side of the boundary. This appears to violate the Gibbs phase rule for a binary system, but sodium evaporation adds another degree of freedom to the system.

By selecting one of the methods, A, B, or C, phase pure $NaNi_xMn_{1-x}O_2$ could be made for $x = 0$, $0.25 \leq x \leq 0.66$, and $x = 1$.  A two-phase region exists between O'3 $NaMnO_2$ and P2 $NaNi_{0.25}Mn_{0.75}O_2$, while the $0.66 < x < 1$ composition range seems to lie in a three-phase $NaNi_{0.66}Mn_{0.33}O_2$ - NiO - NaNiO2 coexistence region in these synthesis conditions. It is believed the co-operative Jahn Teller distortion in the O'3 $NaMnO_2$ and O'3 $NaNiO_2$ end members of this composition series induces phase separations with non-distorted phases, rather than forming intermediate phases with internal stresses.

Rietveld refinements were performed on all samples to obtain lattice constants. Examples of these refinements are shown in Figure 4.6 and Figure 4.7 for the compositions with x = 0.66 and 0.25, respectively.
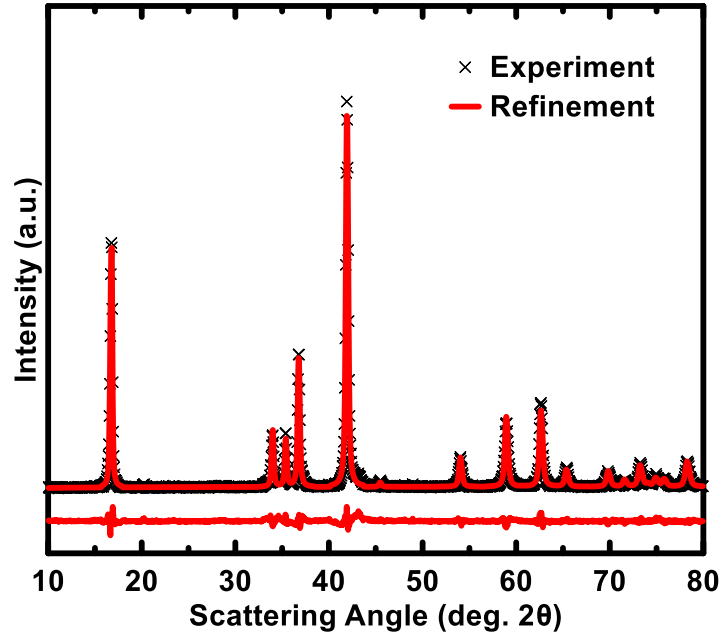


Figure 4.6 XRD pattern and Rietveld refinement of phase pure $NaNi_{0.66}Mn_{0.33}O_2$. The refined parameters are summarized in Table 4.2.
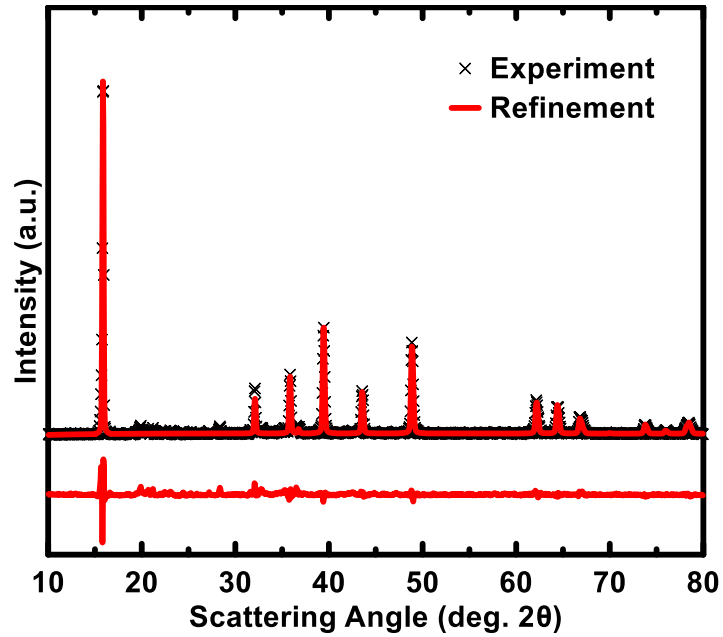


Figure 4.7 XRD pattern and Rietveld refinement of the phase pure $NaNi_{0.25}Mn_{0.75}O_2$. The refined parameters are summarized in Table 4.3.

The crystallographic data for these compositions are summarized in Table 4.2 and Table 4.3,

respectively. For x = 0.66 the O3 α-NaFeO$_2$ (space group R$\bar{3}$m) structure type was used to refine

the XRD pattern. In the refinement Na and Ni were allowed to mix, however the degree of cation

mixing was found to be only 0.7 %. This result indicates that there was relatively no cation

mixing, as suspected. This can be attributed to the difference in ionic radius of Na$^+$ (1.02 Å) and

Ni$^{2+}$ (0.69 Å), which would tend to make cation mixing unfavorable [15]. For x = 0.25, the P2 β-

RbScO$_2$ structure type (space group P6$_3$/mmc) was used to refine the XRD measurements. The

lattice parameters and site occupancies agree with what has been reported by Delmas and Werner

[75].

Table 4.2 Rietveld refinement results for the NaNi$_{0.66}$Mn$_{0.33}$O$_2$ phase.

| NaNi$_{0.66}$Mn$_{0.33}$O$_2$ (R$\bar{3}$m) | | | | | |
|---|---|---|---|---|---|
| atom | site | x | y | z | occupancy |
| Na$_1$ | 3b | 0 | 0 | 0.5 | 0.993(2) |
| Na$_2$ | 3a | 0 | 0 | 0 | 0.007(6) |
| Ni$_1$ | 3a | 0 | 0 | 0 | 0.659(9) |
| Ni$_2$ | 3b | 0 | 0 | 0.5 | 0.007(1) |
| Mn | 3a | 0 | 0 | 0 | 0.333(1) |
| O | 6c | 0 | 0 | 0.2(1) | 2.015(5) |
| Cell parameters | a | b | c | | |
| | 2.960(1) | 2.960(1) | 15.81(2) | R-factor | 2.18 |
| | α | β | γ | | |
| | 90 | 90 | 120 | | |
| Bond distances | | | Bond angles | | |
| d(Na-O) | 2.34 | | ∠O-Na-O | | 101.6, 78.4 |
| d(M-O) | 2.00 | | ∠O-M-O | | 84.3, 95.7 |

Table 4.3 Rietveld refinement results for the $NaNi_{0.25}Mn_{0.75}O_2$ phase.

| $NaNi_{0.25}Mn_{0.75}O_2$ (P6$_3$/mmc) | | | | | |
|---|---|---|---|---|---|
| atom | site | x | y | z | occupancy |
| Na$_1$ | 2b | 0 | 0 | 0.25 | 0.243(8) |
| Na$_2$ | 2d | 0.33 | 0.66 | 0.25 | 0.354(1) |
| Ni | 2a | 0 | 0 | 0 | 0.250(2) |
| Mn | 2a | 0 | 0 | 0 | 0.750(5) |
| O | 4e | 0.66 | 0.33 | 0.090(1) | 2.031(1) |
| Cell parameters | a | b | c | | |
| | 2.891(7) | 2.891(7) | 11.15(1) | R-factor | 4.59 |
| | $\alpha$ | $\beta$ | $\gamma$ | | |
| | 90 | 90 | 120 | | |
| Bond distances | | | Bond angles | | |
| d(Na-O) | 2.42 | | $\angle$O-Na-O | | 92.7, 73.4 |
| d(M-O) | 1.96 | | $\angle$O-M-O | | 85.3, 94.7 |

In chapter 2 structural relationship between the O'3 and O3 unit cells was shown. The monoclinic distortion of the O3 structure occurs due to the presence of Jahn-Teller ions. When the monoclinic structures with x = 0 and 1 were refined, two separate M-O bond lengths in the MO$_6$ octahedra were observed, which is characteristic of the $Mn^{3+}$ ($d^4$ high-spin) and $Ni^{3+}$ ($d^7$ low-spin) Jahn-Teller ions. $NaMnO_2$ has Mn-O bond lengths of 1.93 Å (x4) and 2.40 Å (x2). $NaNiO_2$ has Ni-O bond lengths of 2.02 Å (x4) and 2.22 Å (x2). These distortions will result in variation from the ideal hexagonal $a/b$ ratio of $\sqrt{3}$ (1.732) and $\beta$ angle of 109.11°, leading to a monoclinic distortion of the layered structure. This is seen clearly from the lattice parameters of the $NaMnO_2$; $a = 5.67$ Å, $b = 2.86$ Å and $\beta$ angle = 113.2, where $a/b = 1.98$. These are similar to results reported by the Ceder group [17,27]. Table 4.4 summarizes the cell parameters that were used to fit all of the as prepared single phase samples. Values from past studies are also included and they are in close approximation to those found in this work.

Table 4.4 Rietveld refinement results for NaNi$_x$Mn$_{1-x}$O$_2$ samples, with literature results, where available, for comparison.

| x | Space group | a | b | c | β | M-O bond distance |
|---|---|---|---|---|---|---|
| 0 | C2/m | 5.67, 5.672[17] | 2.86, 2.856[17] | 5.80, 5.807[17] | 113.2, 113.2[17] | 1.93, 2.40 1.94, 2.39[17] |
| 0.25 | P6$_3$/mmc | 2.89 | - | 11.15 | - | 1.96 |
| 0.33 | P6$_3$/mmc | 2.89 | - | 11.07 | - | 2.002 |
| 0.5 | R$\overline{3}$m | 2.94, 2.968[41] | - - | 15.99, 15.909[41] | - - | 2.159 - |
| 0.66 | R$\overline{3}$m | 2.96 | - | 15.81 | - | 2.00 |
| 1 | C2/m | 5.34, 5.322[27] | 2.85, 2.845[27] | 5.62, 5.584[27] | 110.5, 110.467[27] | 2.02, 2.22 1.932, 2.177[27] |

Figure 4.8 shows the lattice parameters of the phase pure NaNi$_x$Mn$_{1-x}$O$_2$ compositions obtained as a function of x. In order to make comparisons all structures were indexed according to the hexagonal O3 lattice using the following relations:

$$O'3 \rightarrow O3: \quad a_1 = \sqrt{\left(\frac{a_m}{2}\right)^2 + \left(\frac{b_m}{2}\right)^2}; \ a_2 = b_m; \ c = 3c_m \sin \beta \qquad (4.1)$$

$$P2 \rightarrow O3: \quad a = b = a_{P2}; \ c = \frac{3}{2}c_{P2} \qquad (4.2)$$

where $a$, $b$, and $c$ are lattice constants with respect to the O3 unit cell, $a_m$, $b_m$, $c_m$ and $\beta$ are the O'3 unit cell parameters and $a_{P2}$, $b_{P2}$, $c_{P2}$ are the P2 unit cell parameters. Using this formalism, the O'3 lattice will have two non-equivalent $a$ lattice constants, denoted as $a_1$ and $a_2$. Lattice constants from previous studies are also plotted on Figure 4.8, and are in good agreement with results herein. Generally, as x increases $a$ increases and $c$ decreases. Some discontinuities in these parameters are present at the structural phase boundaries.
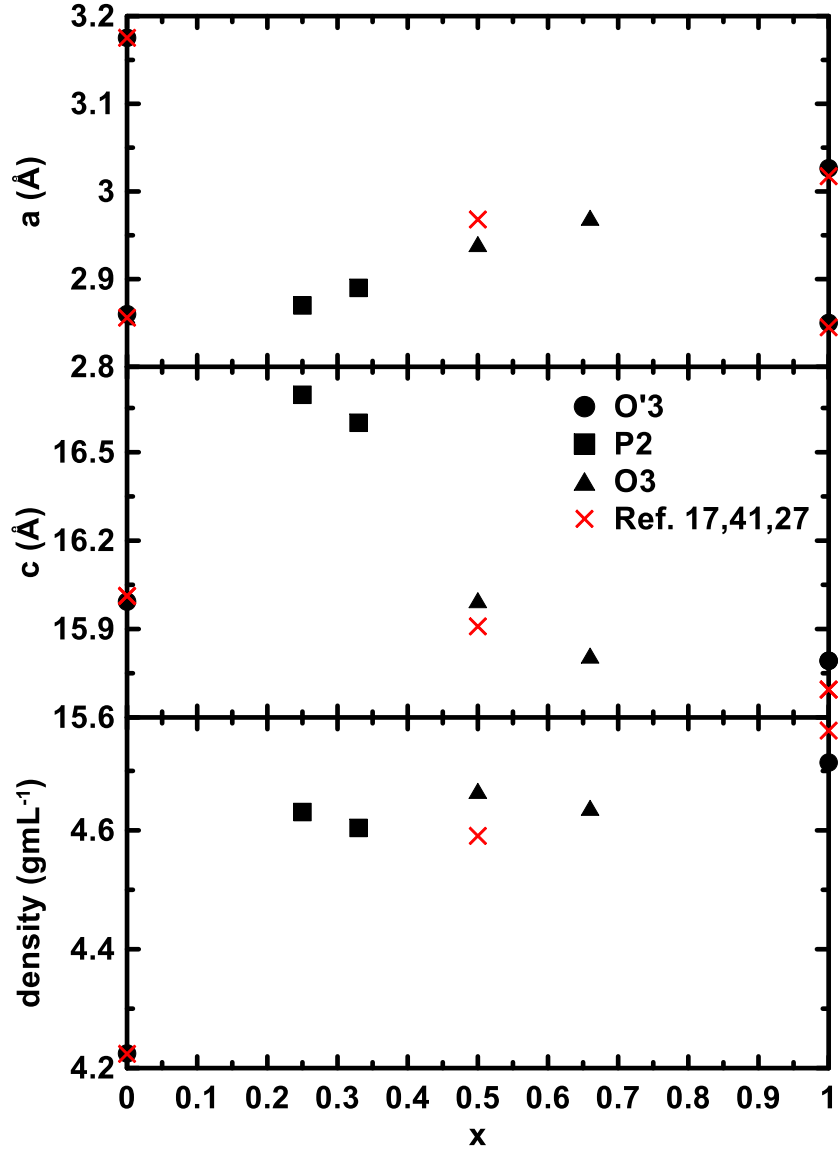
Figure 4.8 Evolution of the lattice parameters *a* and *c*, as well as the density of NaNi$_x$Mn$_{1-x}$O$_2$ as a function of x.  All lattice parameters are expressed in terms of the O3 structure, as described in the text.

To understand the trends in the lattice constants and structural changes it is first convenient to assume the transition metal oxidation states are as follows:

$$\text{NaMn}^{3+}_{1-2x}\text{Mn}^{4+}_x\text{Ni}^{2+}_x\text{O}_2;\ 0 \leq x \leq \tfrac{1}{2} \tag{4.3}$$

$$\text{NaNi}^{3+}_{2x-1}\text{Mn}^{4+}_{1-x}\text{Ni}^{2+}_{1-x}\text{O}_2;\ \tfrac{1}{2} \leq x \leq 1. \tag{4.4}$$

43
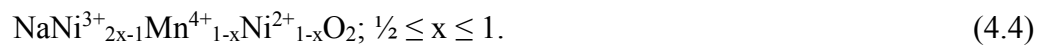
This formulism can explain the different phases observed, as shown in Figure 4.5. When x = 0, all the manganese is present as $Mn^{3+}$, resulting in a co-operative Jahn-Teller distortion and $NaMnO_2$ having a monoclinic phase. Typically such a distortion persists while the average oxidation state remains below 3.5, as it does in $Na_{2/3}[Mn_{1-y}Ni_y]O_2$ for $0 < y < 1/6$, in which a distorted P'2 structure is formed [73]. Such a distorted P'2 phase was not observed here. Although the average oxidation state of Mn is below 3.5 for x < ⅓, the system prefers to form a two-phase region between monoclinic $NaMnO_2$ and an ideal P2 structure for 0 < x < ¼. For ⅓ < x < ⅔ the lattice remains fully symmetric as the O3 phase. For ⅔ < x < 1 the system again prefers adopting a two-phase state as a response to increasing amounts of the $Ni^{3+}$ Jahn-Teller ion, instead of adopting a structure in which both Jahn-Teller distorted ions and symmetric ions coexist.

The change in the *a* lattice constant is typically attributed to the difference in radii of the different ions in the transition metal layer. In this case where *a* increases with increasing Ni content this argument cannot be made because as x increases each $Mn^{3+}$ (0.645 Å) is replaced by a $Ni^{2+}$ (0.69 Å) and a $Mn^{4+}$ (0.53 Å), which have a lower average ionic radius [15]. The variation in the *c* lattice constant with x is likely due to the packing efficiency between the different structures. The O'3 and O3 all have similar *c* values while the less efficient packing of the P2 structures cause them to have much higher *c* lattice constants. Overall the changes in lattice the constants result in the little changes in the density for the P2 and O3 compositions ($0.2 \leq x \leq 0.67$), which is about 4.63 g/mL in this range of x. The density of $NaMnO_2$ is much less, 4.23 g/mL, presumably due to the large monoclinic distortion in the structure [17].

## 4.3 Electrochemistry

Electrodes for electrochemical measurements were made as previously described in Sections 3.4 and 3.5. Cells were cycled between 1.8 V and 4.3 V at a constant current of C/10, calculated based on the theoretical capacity corresponding to the removal of all of the sodium from the positive electrode. Figure 4.9 shows the voltage curves of the phase pure $NaNi_xMn_{1-x}O_2$ materials that were prepared. There are several plateaus which appear for each composition and they are similar for both charge and discharge (except for the first charge in some compositions), indicating reversible processes. The step like character of the many plateaus is expected for these sodium containing materials [76]. In general sodium intercalation materials tend to have more phase transitions than the lithium containing ones. This difference is likely due to interactions between the larger $Na^+$ ions which produce ordering interactions.

Many of the compositions in the $NaNi_xMn_{1-x}O_2$ series display high first discharge capacities. The highest first discharge capacity was for x = 0.66, with a capacity of ~ 190 mAh/g. All of these materials have high first cycle irreversible capacities, except for x = 0.33 and 0.5. Electrolyte decomposition above 4 V could contribute to these high irreversible capacities, which can be somewhat supressed when the upper voltage limit is lowered. NMR studies could be performed after cycling to determine whether electrolyte decomposition has occurred.
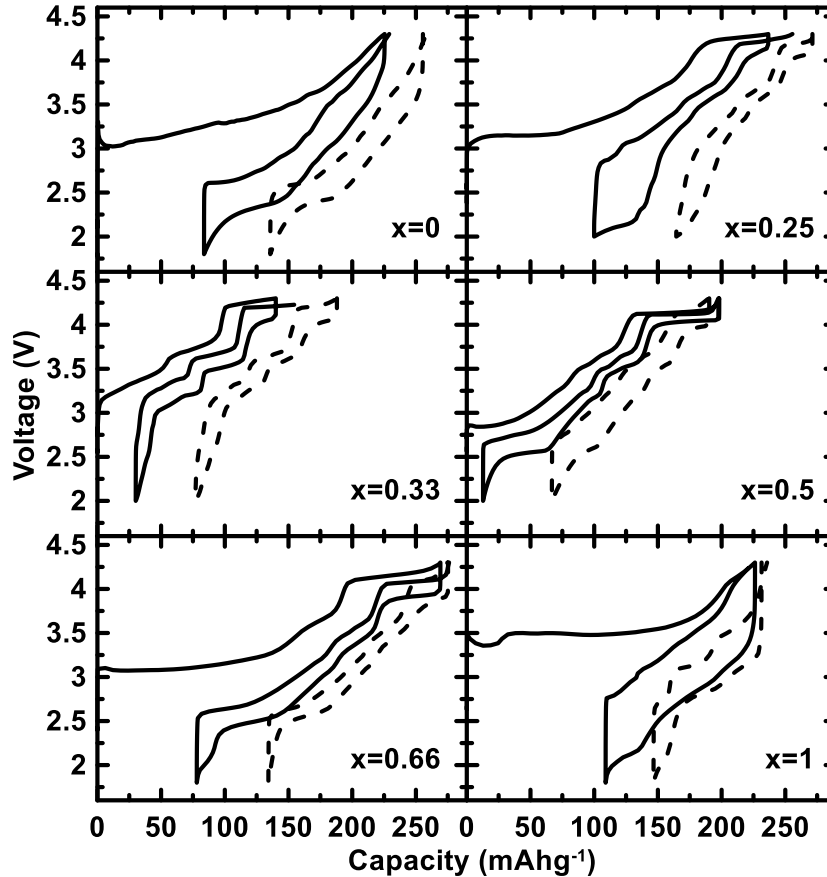
Figure 4.9 Voltage curves of $NaNi_xMn_{1-x}O_2$ at C/10 cycling rate and 30°C. The voltage curves of the 10th cycle are shown as dotted lines.

Figure 4.10 shows the specific discharge capacities with cycle number for $NaNi_xMn_{1-x}O_2$ cycled between 1.8 and 4.3 V. All compositions, except x = 1, had capacities greater than 100 mAh/g over for 20 cycles, but had severe capacity fade. For compositions where there exist results in the literature these findings show good agreement [17,27,42]. When cycled in this voltage range, the volumetric energy densities of $NaNi_xMn_{1-x}O_2$ ranged from 1650 to 2705 Wh/L. The highest volumetric energy density of 2705 Wh/L was achieved for x = 0.66, with 190 mAh/g capacity and an average discharge voltage of 3.07 V. This approaches the energy density of Li-ion cathodes (e.g. ~2900 Wh/L for $LiNi_{1/3}Mn_{1/3}Co_{1/3}O_2$) and is among the highest reported volumetric energy densities for Na-ion battery electrodes.
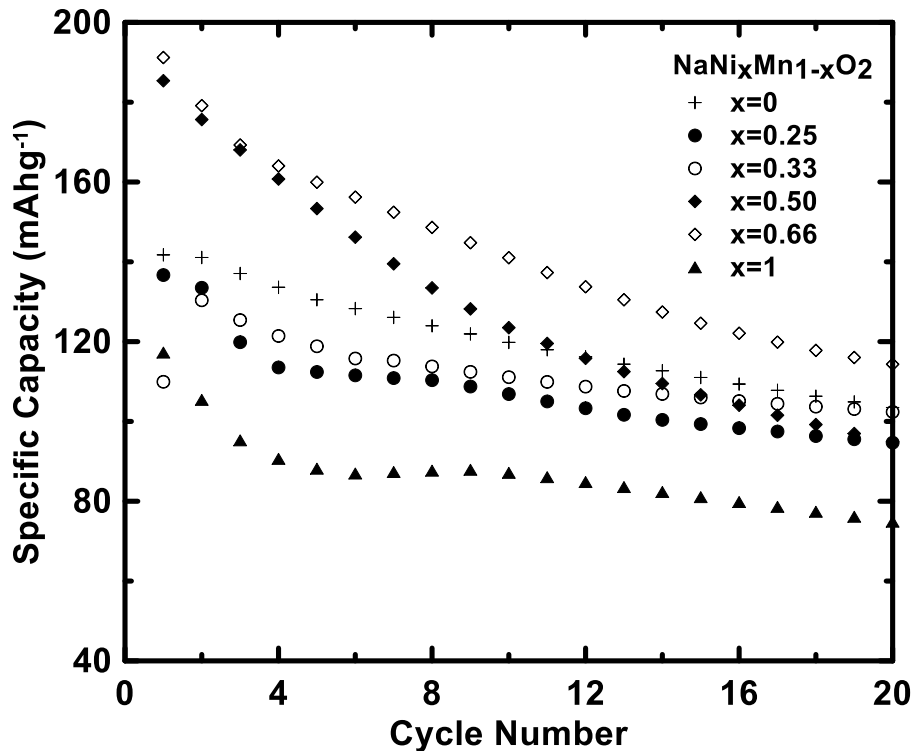
Figure 4.10 The discharge capacities versus cycle number for NaNi$_x$Mn$_{1-x}$O$_2$. Cells were cycled at C/10 at 30°C between 1.8 and 4.3 V.

Cycling behavior is marginally improved when the voltage windows are narrowed. An example of this is Figure 4.11 which shows the cycling behavior of NaNiO$_2$, for different voltage windows. The improved cycling may be due to the structural stability that is gained when not all of the Na is removed from the structure or to a reduction in electrolyte decomposition reactions at high voltages or simply may result because less capacity is being accessed at the Na counter electrode.
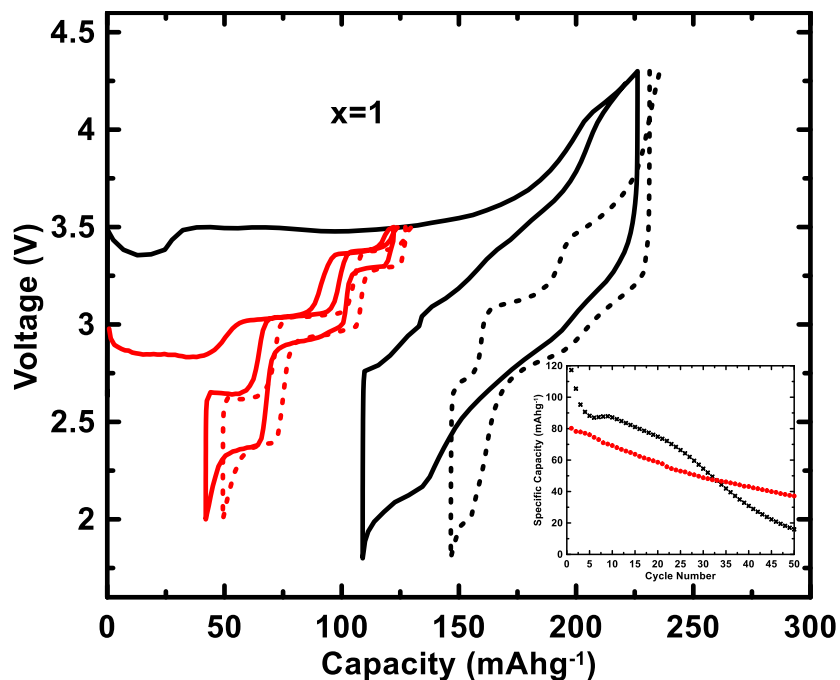
Figure 4.11 Voltage curves of NaNiO$_2$ at C/10 cycling rate and 30°C between 2 – 3.5 V (red) and 1.8 – 4.3 V (black). The inset shows the capacity versus cycle number.

## 4.4 Conclusions

Phase pure layered NaNi$_x$Mn$_{1-x}$O$_2$ (where x = 0, 0.25, 0.33, 0.5, 0.66, and 1) were synthesized via solid-state reactions. Different synthesis conditions were required, depending on the composition, to obtain phase pure compositions. Phase diagrams were determined for each syntheses method. These materials have a monoclinically distorted O'3 structure (x = 0, 1), P2 structure (0.25 ≤ x ≤ 0.33) or an O3 structure (0.5 ≤ x ≤ 0.66). Excepting for x = 0, all compositions have high densities, above 4.6 g/mL. All compositions have high reversible capacities when cycled between 1.8 and 4.3 V. The x = 0.66 composition had the highest first discharge capacity of ~ 190 mAh/g and highest volumetric energy density of 2705 Wh/L. This is one of the highest energy densities reported for Na-ion cathode materials. However, all compositions had poor cycling

48

performance. Further improvements, such as electrolyte optimization, are required for materials in this series to be utilized in practical cells.

# CHAPTER 5    CATHODE AND ANODE MATERIALS BASED ON Na$_x$Ni$_{x/2}$Ti$_{1-x/2}$O$_2$ ($0.5 \leq x \leq 1.0$)

## 5.1 Introduction

The Na$_x$Ni$_{x/2}$Ti$_{1-x/2}$O$_2$ series was studied as both a positive and negative electrode material, as it contains nickel as well as titanium atoms in its transition metal layer.  The nickel (II) redox reaction should occur at a high voltage and the titanium (IV) at low voltage.  Many sodium-ion cathode materials have been proposed, most of which are based on layered sodium transition metal oxide materials.  Cathode materials with high energy density based on abundant, low cost raw materials have been reported [33,37,40,42] and the NaNi$_x$Mn$_{1-x}$O$_2$ system reported previously fall in this category.   These cathode materials could enable high energy density commercial sodium-ion batteries, if paired with a practical anode material.  Unfortunately practical high energy density anode materials for sodium-ion batteries have proven much harder to achieve.  A layered true intercalation material for the anode could be the answer for a practical sodium negative electrode, such as modified low voltage titanium and vanadium containing sodium metal oxides.

Metal oxide intercalation hosts have been studied extensively as negative electrodes for Li-ion batteries.   While most transition metal oxides (TMO) decompose via displacement/conversion reactions below about 1.5 V vs. Li, vanadium and titanium oxides can be stable at 0 V vs. Li and reversibly intercalate lithium at low voltages [77,78].  While bulk LiVO$_2$ particles have a high energy density and a low average voltage (0.1 V vs. Li), titanates generally operate at about 1.6 V vs. Li and are insulating or have poor lithium diffusion [77,79,80].  This requires the use of nano-sized particles to enable intercalation and results in a comparatively low volumetric energy density [81].

The voltage of TMOs in sodium cells is predicted to be generally less than that in Li cells [62]. This voltage difference tends to make sodium-ion cathode energy densities lower than Li-ion cathodes. However, the opposite is true for negative electrodes, where the low intercalation voltage of sodium into TMOs would tend to make their energy density higher. Recently, $Na_2Ti_3O_7$, which has a potential between 1.0 to 1.6 V vs. Li, has been shown to reversibly intercalate sodium at only 0.3 V with a gravimetric capacity of 178 mAh/g [49]. This corresponds to a volumetric capacity of around 600 Ah/L. However, as is typical of titanates, $Na_2Ti_3O_7$ requires ball milling with a large amount of carbon to enable reversible cycling, resulting in a low density and high surface area electrode.

If titanates could be made conductive, like $LiVO_2$, bulk intercalation might occur. One method to make titanates conductive is to add other first-row transition metals [82]. In lithium cells this would likely be a poor strategy as the addition of other first-row transition metals to titanates would likely cause the lithiation voltage to increase unacceptably and further cause displacement type reactions to occur at low voltages. However, for sodium-ion cells, it might be a very good strategy in which to design bulk particles that can intercalate sodium-ions at low voltages.

Using this strategy, sodium insertion into $Na_xNi_{x/2}Ti_{1-x/2}O_2$ ($0.5 \leq x \leq 1.0$) was investigated. The $Na_{2/3}Ni_{1/3}Ti_{2/3}O_2$ composition in this series has recently been studied as a bi-functional electrode material by Shanmugam and Lai [83]. Studies of sodium nickel titanates for Na-ion batteries had previously focused on cathode materials [84–86]. Unlike the pure titanates, materials in this series were found to have the ability to reversibly intercalate sodium into bulk, crystalline $Na_xNi_{x/2}Ti_{1-x/2}O_2$ powders at an average voltage of about 0.7 V with low hysteresis. The $Na_xNi_{x/2}Ti_{1-x/2}O_2$ series was found to be structurally

51

stable at 0 V vs. Na. The use of transition metal titanates presents a new strategy towards making negative electrodes for sodium-ion cells, from which high energy density bulk intercalation materials may be developed.

## 5.2 Experimental

To prepare $Na_xNi_{x/2}Ti_{1-x/2}O_2$ ($0.5 \leq x \leq 1.0$), $Na_2CO_3$ (BioXtra, $\geq$ 99.0% Sigma Aldrich), NiO (−325 mesh, 99 % Alfa Aesar), and $TiO_2$ (puriss, 99 − 100.5 %, Sigma-Aldrich) were ball milled for a half hour and the powder was then fired at 900 °C in argon for 10 hours. As always, a 10 % excess by weight of $Na_2CO_3$ was used to compensate for the loss of sodium due to its volatility at high reaction temperatures. After synthesis, samples were transferred directly to an argon filled glove box without air exposure, as the materials are hygroscopic.

$Na_xNi_{x/2}Ti_{1-x/2}O_2$ ($0.5 \leq x \leq 1.0$) samples were characterized by XRD using a Rigaku Ultima IV X-Ray Diffractometer equipped with a Cu anode X-ray tube and dual detectors. A scintillation detector with a diffracted beam monochromator was used to measure XRD patterns of powder samples and *ex situ* XRD samples of electrodes. A D/TeX Ultra linear detector with K-beta filter was used for *in situ* XRD measurements. Electrochemical cells were constructed as previously described in section 3.4 and cycled on a Maccor Series 4000 Automated cycler. Cells were cycled at a constant current of C/10, calculated based on a 100 mAh/g capacity for low voltage cycling from 0.005 to 2 V and 200 mAh/g for cycling from 0.3 to 4.3 V. Some high voltage cycling was done between 1.8 and 4.3 V too assuming 100 mAh/g.

*In situ* coin cell type cells were constructed using the same procedure as previously described in section 3.4, except the top cell can had a circular aperture cut in it to receive

a thin Be window, as Be is transparent to X-rays.  An electrode was then made directly onto the Be window, using the coating procedure described already in section 3.4.  The Be window was then affixed in the cell can using Roscobond, a pressure-sensitive adhesive (Rosco).  After the cell was crimped shut, the cell can .was sealed using Torr Seal epoxy resin (Varian).  *In situ* cells were cycled at a rate of C/10 between 0.005 and 2 V assuming a capacity of 100 mAh/g.

Coin cells for *ex situ* XRD studies were prepared as described in section 3.5, but once cycling they were stopped at different states of charge.  Electrodes for *ex situ* XRD measurements were then recovered from these cells in an argon glove box, and the electrode coating was scraped off the current collector and washed with dimethyl carbonate (DMC, Novolyte Technologies).  The DMC was then removed by evaporation in a vacuum. The recovered electrode coating was then transferred to a zero-background silicon wafer and sealed in the gas tight sample holder under flowing helium gas for the *ex situ* XRD measurements.

Figure 5.1 shows an SEM image of the as prepared powder $Na_{0.6}Ni_{0.3}Ti_{0.7}O_2$ sample.  The particle size ranges from 2 to 10 μm with a plate type morphology, which is typical of all the samples in the $Na_xNi_{x/2}Ti_{1-x/2}O_2$ ($0.5 \leq x \leq 1.0$) series.
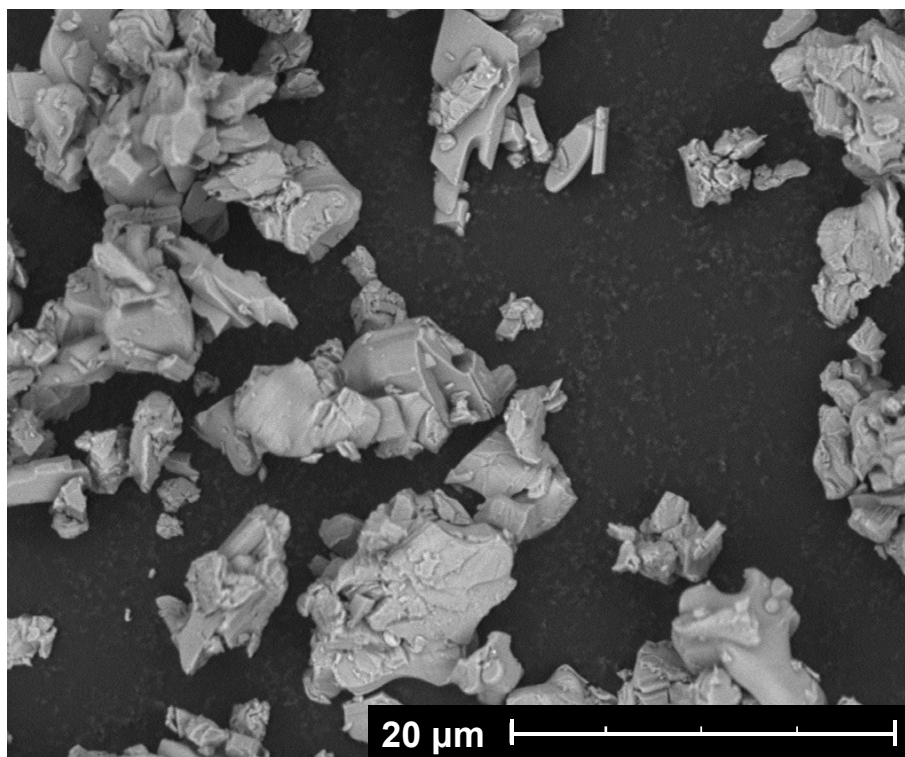
Figure 5.1 SEM image showing $Na_{0.6}Ni_{0.3}Ti_{0.7}O_2$ particles as prepared by solid-state synthesis.

Figure 5.2 shows the XRD patterns of the $Na_xNi_{x/2}Ti_{1-x/2}O_2$ series in the range of $0.5 \leq x \leq 1.0$. Samples with $1 > x \geq 0.75$ were phase pure with the O3 structure (using the notation by Delmas) [61]. A phase pure sample could not be obtained for $x = 1.0$. An impurity phase of NiO was present, despite many efforts to alter the sintering temperature, time, and oxygen partial pressure. Samples with $0.66 < x < 0.6$ were phase pure with the P2 structure. There is a region of P2 and O3 coexistence at $x = 0.7$. Below $x = 0.6$ multiple unidentified phases are present. It is thought that at such low x values there are not enough sodium ions present to maintain the layered framework. These results are consistent with those of Shin and Yi [87].
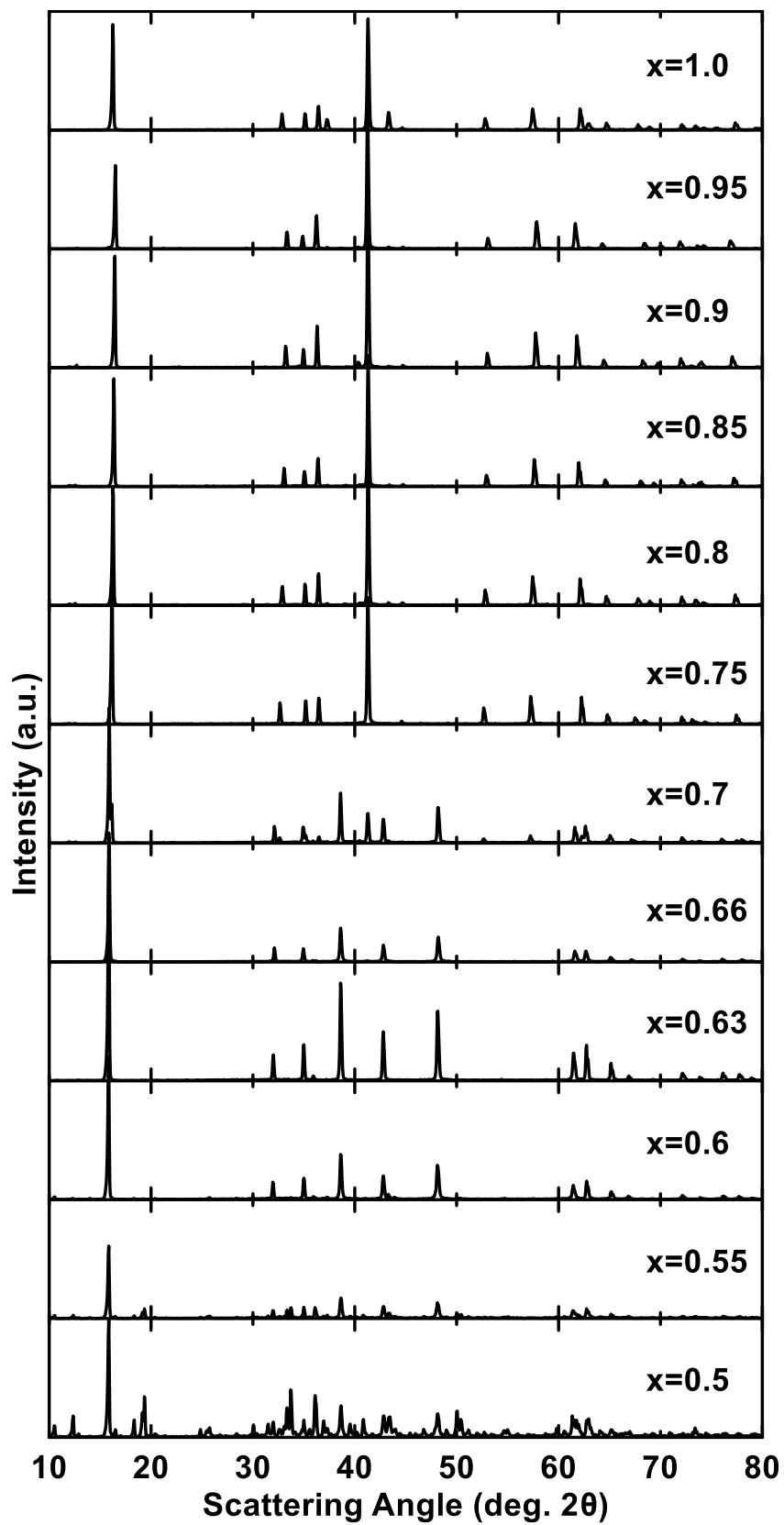
Figure 5.2 XRD patterns for the $Na_xNi_{x/2}Ti_{1-x/2}O_2$ series from $0.5 \leq x \leq 1.0$.

Rietveld refinement was conducted for the XRD patterns of all of the samples that were composed of P2 or O3 phases exclusively ($0.6 \leq x \leq 0.95$). The Bragg R factors for all the refinements were less than 4.00 %. As an example, Figure 5.3 shows the experimental XRD pattern of $Na_{0.6}Ni_{0.3}Ti_{0.7}O_2$ and the pattern calculated by Rietveld refinement of the P2 structure.
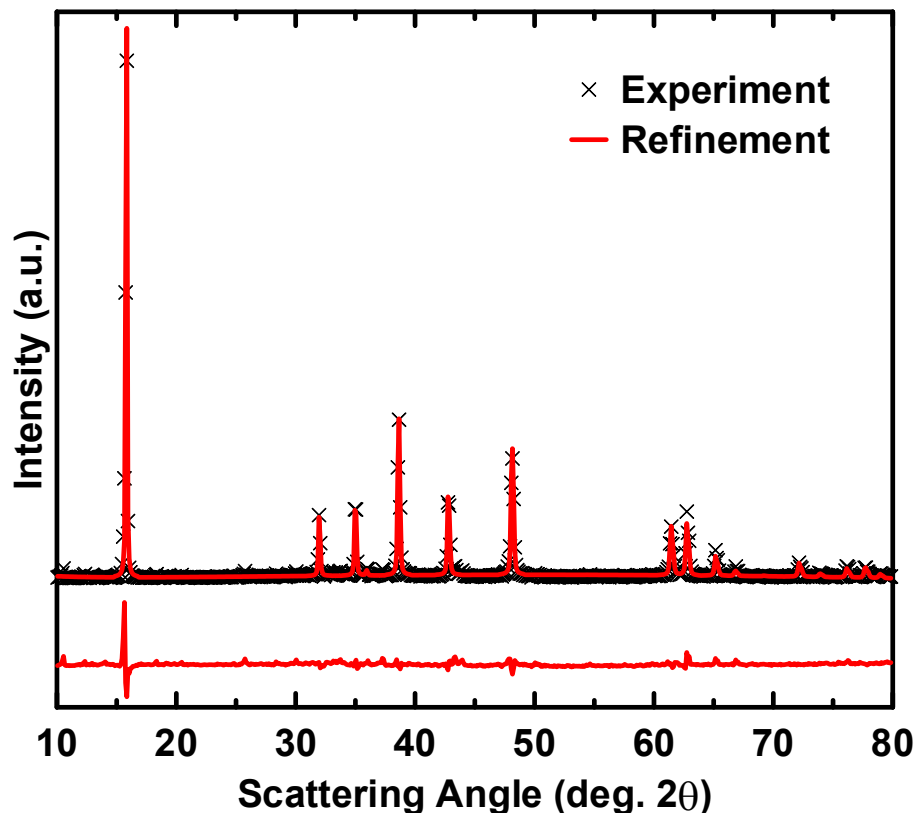


Figure 5.3 XRD pattern and Rietveld refinement of $Na_{0.6}Ni_{0.3}Ti_{0.7}O_2$.

The crystallographic parameters used for the refinement are listed in Table 5.1. The ordered layered structure of the sodium deficient materials with the P2 structure is illustrated in Figure 5.4. The transition metals and sodium occupy alternating layers of octahedral and prismatic sites, respectively, with vacancies occurring in the sodium layer.

Table 5.1 Parameters used to refine the pristine $Na_{0.6}Ni_{0.3}Ti_{0.7}O_2$ P2 structure.

| $Na_{0.6}Ni_{0.3}Ti_{0.7}O_2$ ($P6_3/mmc$) | | | | | |
|---|---|---|---|---|---|
| atom | site | x | y | z | occupancy |
| $Na_1$ | 2b | 0 | 0 | 0.25 | 0.1700(1) |
| $Na_2$ | 2d | 0.33 | 0.66 | 0.25 | 0.4121(7) |
| Ni | 2a | 0 | 0 | 0 | 0.3 |
| Ti | 2a | 0 | 0 | 0 | 0.7 |
| O | 4e | 0.66 | 0.33 | 0.093(8) | 2.0053(2) |
| Cell parameters | a | | b | c | |
| | 2.958(8) | | 2.958(8) | 11.18(9) | |
| | α | | β | γ | R-factor    2.71 |
| | 90 | | 90 | 120 | |
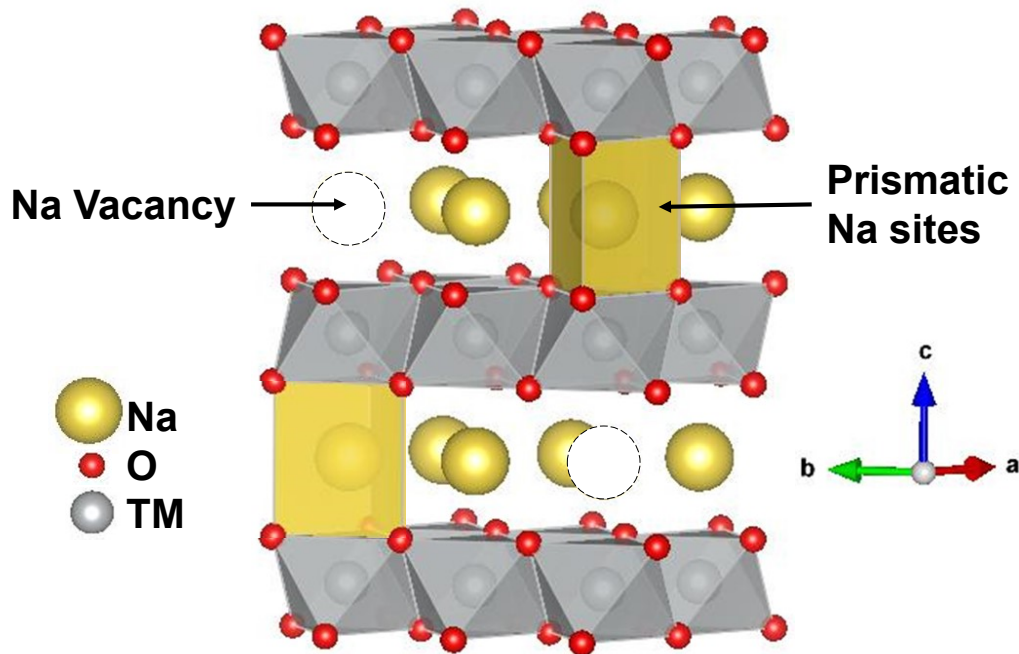


Figure 5.4 Structure of the P2 layer-type oxide.  Sodium prismatic sites are shown and sodium vacancies are displayed by dotted circles.

Figure 5.5 shows how the lattice constants *a* and *c* change with respect to x.  In order to compare the *c* lattice constants of the P2 and O3 structures, the *c* lattice constants of the P2 structures were multiplied by a factor of 3/2.  At x = 0.7 the P2 and O3 phases coexist, resulting in two values of lattice constants for this composition.
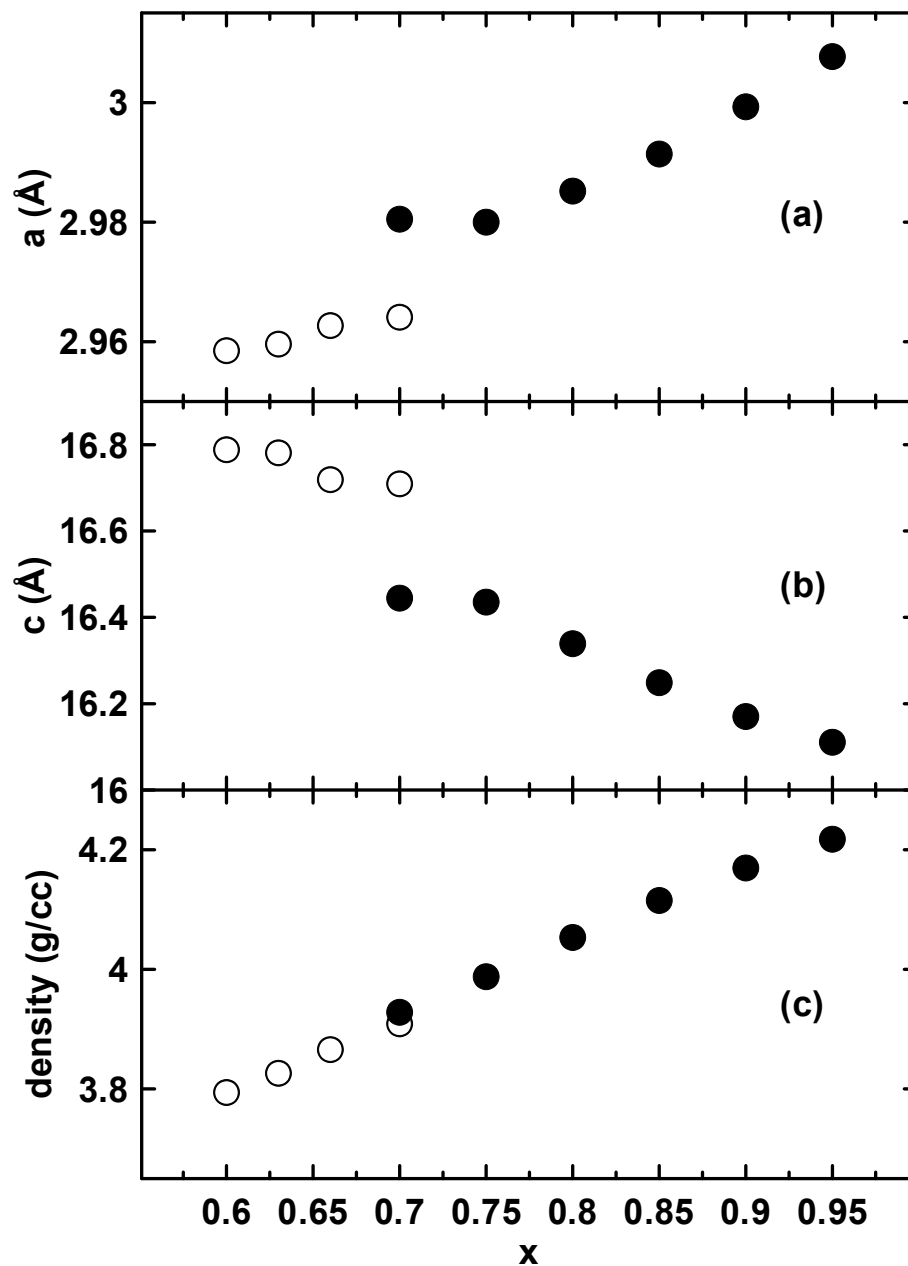
Figure 5.5 Lattice constants and the density of the $Na_xNi_{x/2}Ti_{1-x/2}O_2$ series of oxides where layered phases were observed. The lattice constants $a$ and $c$ are shown in panels (a) and (b), respectively, and the density is shown in panel (c). P2: open circles, O3: solid circles.

These lattice constant values are in good agreement with structural work done on these materials by Shin and Yi [87]. As x is increased the lattice constant $a$ increases, while $c$ decreases, and, furthermore, there is a discontinuity in the lattice constants in the transition from P2 to O3. The increase in $a$ with x can be attributed to the smaller ionic

radius of $Ti^{4+}$ compared to $Ni^{2+}$ [15], while the decrease in the $c$ lattice constant with x is likely due to the decrease in electrostatic repulsion between oxygen layers as vacancies in the Na layers are filled.  Because the $a$ lattice constant increases, while the c lattice constant decreases with x, the unit cell volume changes very little over the entire series.  As a result the density increases with x, as shown in Figure 5.5 (c), as the unit cell mass increases with increasing sodium content.

## 5.3 Electrochemistry

Figure 5.6 shows the voltage curve of cells with three compositions in the $Na_xNi_{x/2}Ti_{1-x/2}O_2$ series, namely x = 0.95, 0.75, and 0.6 vs. Na.  Here positive capacity is defined as when sodium is added in excess of the material's initial sodium composition. Negative capacity occurs when sodium has been removed so that the materials sodium composition is less than it was initially.  This can easily be seen from the upper x-axis in Figure 5.6 where the sodium composition y in $Na_{x+y}Ni_{x/2}Ti_{1-x/2}O_2$ is labelled.  The cells were initially charged (desodiation) to 4.3 V, then discharged to 0.3 V, and then charged to 4.3 V again.
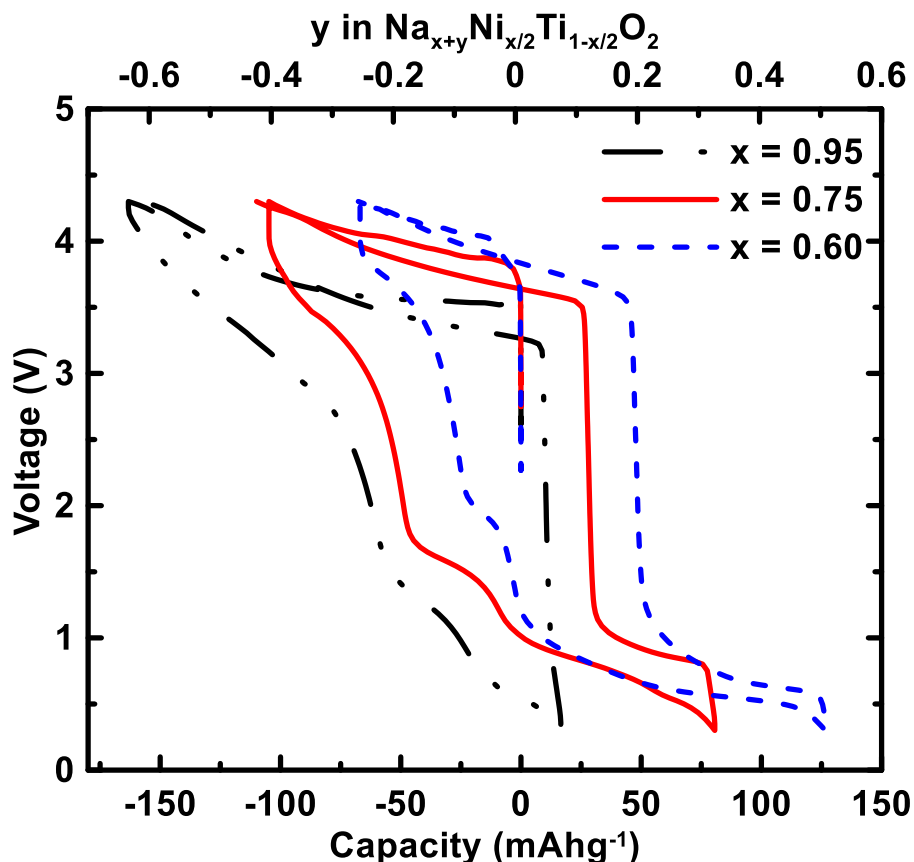
Figure 5.6 Voltage curves of $Na_xNi_{x/2}Ti_{1-x/2}O_2$ oxides with x = 0.95, 0.75, and 0.60 phases between 0.3 and 4.3 V. The sodium content change during cycling is indicated on the top axis as y in $Na_{x+y}Ni_{x/2}Ti_{1-x/2}O_2$.

For all three materials, a single sloping plateau at about 3.5 V was observed during the initial charge. During the subsequent discharge, three sloping plateaus are observed at about 3.5 V, 1.5 V and 0.7 V. The lowest plateau occurs at positive capacities. All the plateaus were found to be highly reversible and reappear during subsequent cycles. Large voltage hysteresis is present for all the plateaus, except the lowest voltage plateau, which has only about 0.1 V hysteresis, which is suggestive of intercalation. This is remarkable, since conversion type reactions in oxides typically occur in transition metal oxides below 1 V [51]. The presence of titanium may be stabilizing the structure at low voltages.

Figure 5.7 shows the voltage curves for $x = 0.66$ and 0.95 when the voltage is restricted to 1.8 and 4.3 V for the first two cycles. Huge voltage hysteresis is present and as a result poor cycling is observed. As $x$ is decreased the high voltage plateau during charge decreases in capacity. This result is consistent with there being less sodium available for desodiation in $Na_xNi_{x/2}Ti_{1-x/2}O_2$ as $x$ is decreased.
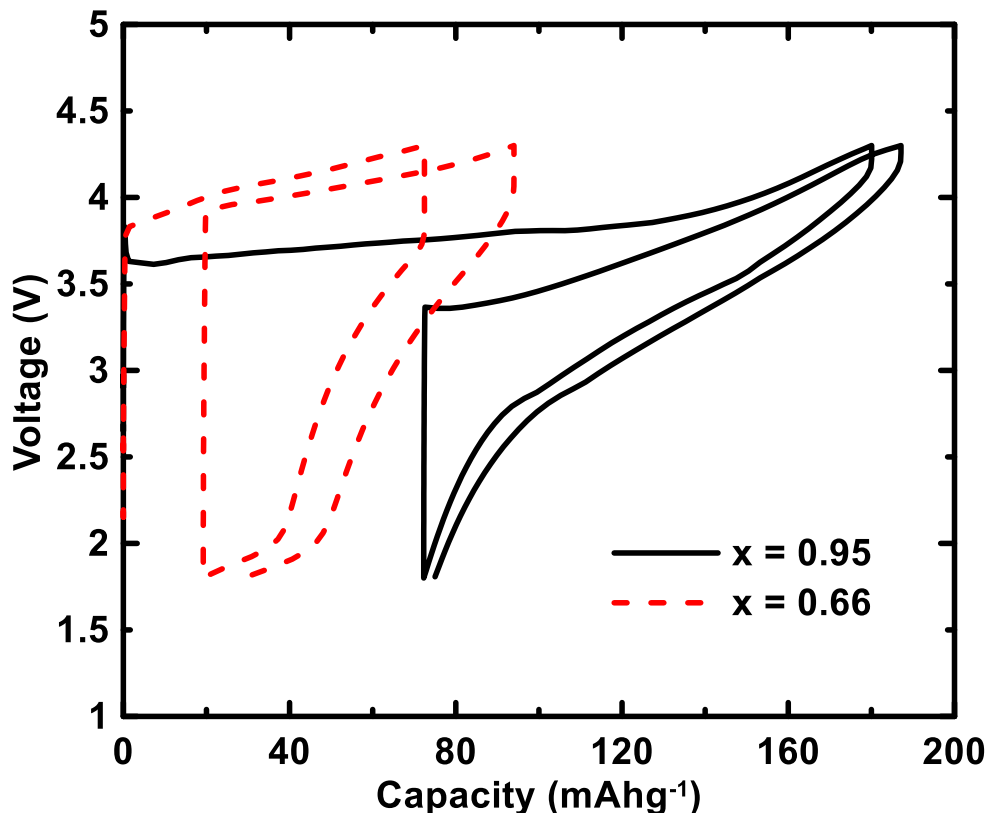


Figure 5.7 Voltage curves of the $Na_xNi_{x/2}Ti_{1-x/2}O_2$ oxides with $x = 0.95$ and 0.66 phases between 1.8 and 4.3 V.

At the same time as the high voltage plateau decreases, the lowest voltage plateau increases in capacity as $x$ is decreased. This plateau is associated with providing the material with more sodium than it had initially. During discharge on this plateau sodium is being accommodated into the vacancies in the $Na_xNi_{x/2}Ti_{1-x/2}O_2$ sodium layer (as is confirmed by *in situ* XRD below). Therefore the increasing capacity of this plateau with decreasing $x$ is

consistent with the number of sodium vacancies in $Na_xNi_{x/2}Ti_{1-x/2}O_2$ increasing with decreasing x.  To confirm this model, the capacity of the lower voltage plateau during charging up to 2 V versus the number of vacancies (1-x) is plotted in Figure 5.8 for the entire $Na_xNi_{x/2}Ti_{1-x/2}O_2$ series.  Also shown is the theoretical capacity based on each inserted sodium occupying one vacancy in the lattice.  The experimental results are in good agreement with theoretical capacities, although they are consistently lower by ~5 mAh/g, which could be due to parasitic sodium consuming side reactions that occur with the electrolyte.
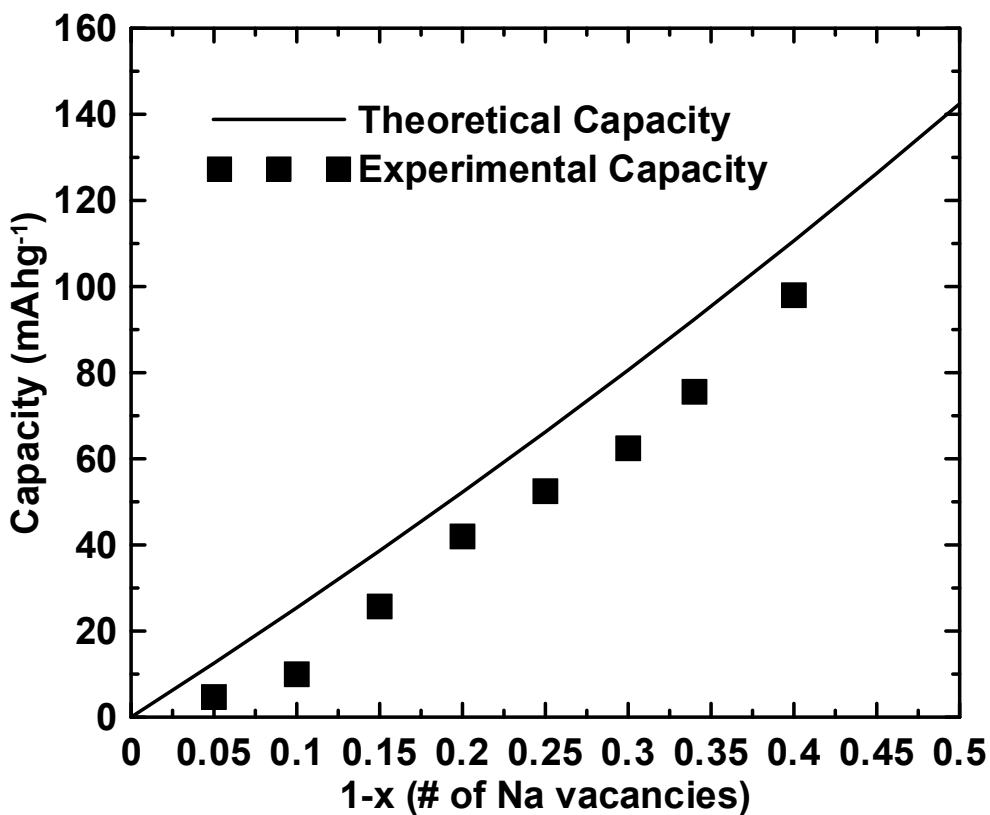


Figure 5.8 Gravimetric capacity of the lower voltage plateau during charging up to 2 V of the $Na_xNi_{x/2}Ti_{1-x/2}O_2$ oxides versus the number of sodium vacancies (1-x).  The theoretical low voltage capacity, based on the number of Na vacancies, is shown by the solid line.

The low voltage and low hysteresis of the low voltage plateau is interesting for negative electrode material applications in sodium cells, especially for those materials with

low values of x. Therefore the cycling characteristics on the low voltage plateau was investigated. Figure 5.9 shows the voltage curve of a $Na_{0.6}Ni_{0.3}Ti_{0.7}O_2$ vs. sodium cell that was initially discharged and cycled between 5 mV and 2 V at a rate of C/10 and 30 °C. This voltage range restricts cycling to the low voltage plateau. The voltage curve exhibits a large first cycle irreversible capacity and a reversible capacity of about 104 mAh/g (or 394 Ah/L), which is proximate to the theoretical value of 110 mAh/g for the capacity that can be accommodated by the Na vacancies in $Na_{0.6}Ni_{0.3}Ti_{0.7}O_2$. The average voltage during desodiation was 0.7 V. The volumetric capacity of $Na_{0.6}Ni_{0.3}Ti_{0.7}O_2$ is slightly less than that of hard carbon (450 Ah/L). To increase the capacity further would require the inclusion of more vacancies (lower values of x in $Na_xNi_{x/2}Ti_{1-x/2}O_2$). For instance, the theoretical capacity increases to 540 Ah/L when x = 0.5. However, when x < 0.6, phase pure layered samples could not be obtained and the capacity suffers.
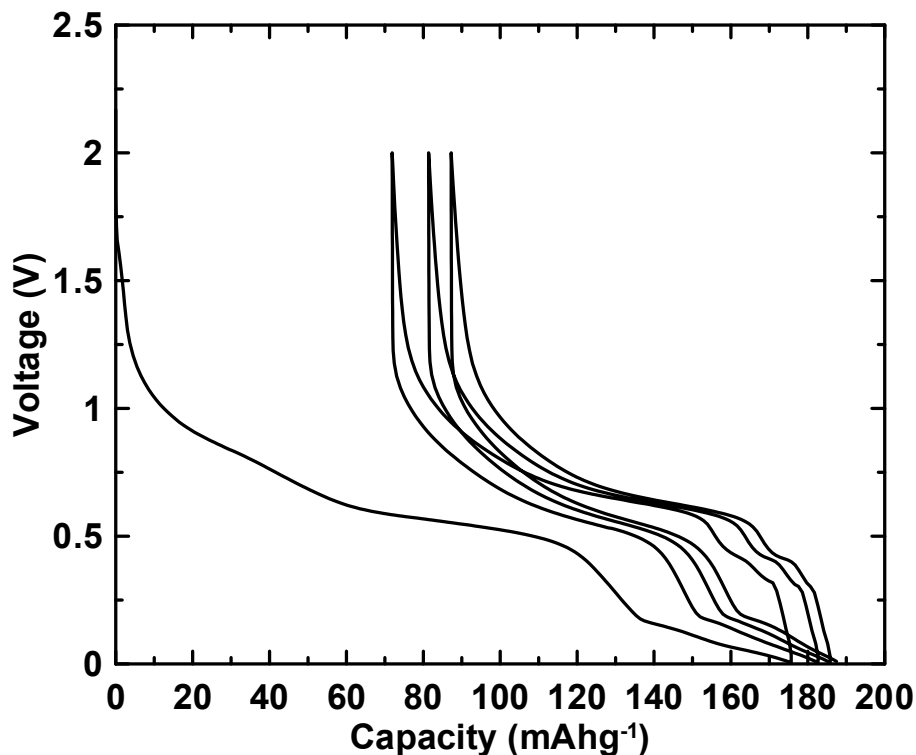


Figure 5.9 Voltage curve of $Na_{0.6}Ni_{0.3}Ti_{0.7}O_2$.

Figure 5.10 shows the capacity versus cycle number of the cell shown in Figure 5.9. The cell exhibits a linear fade over 50 cycles and a maximum Coulombic efficiency of only 99.01 %. These characteristics need to be improved for such materials to be used in practical application.
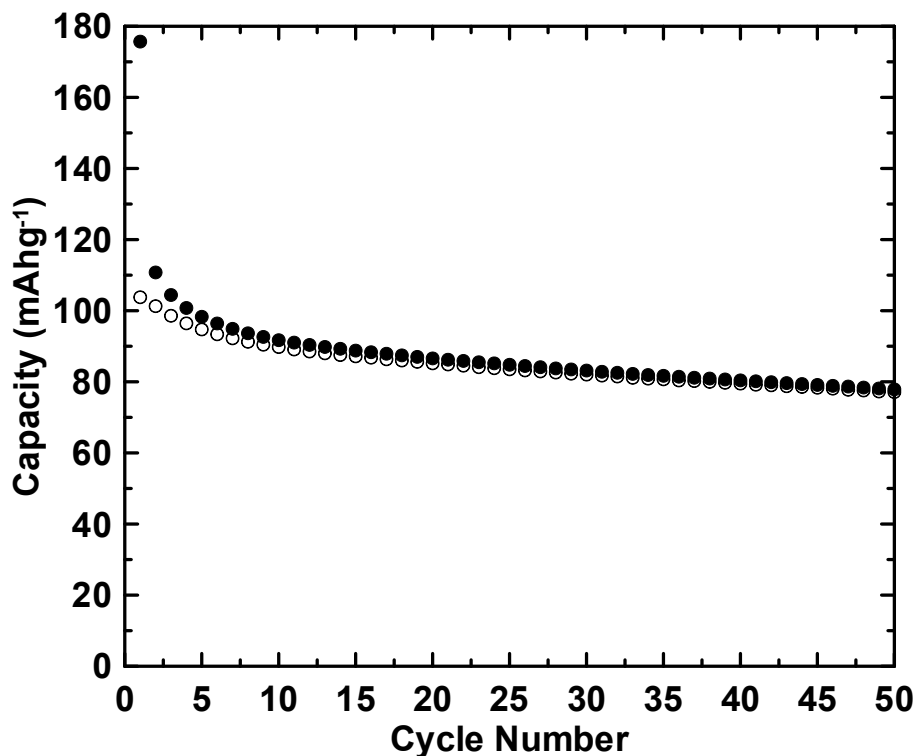


Figure 5.10 Capacity versus cycle number of $Na_{0.6}Ni_{0.3}Ti_{0.7}O_2$ over 50 cycles.

The features in the $Na_{0.6}Ni_{0.3}Ti_{0.7}O_2$ voltage curve shown in Figure 5.9 can be more readily seen in the differential capacity plot shown in Figure 5.11. Features in the differential capacity change during cycling. The first discharge has four peaks, with the first peak at 0.85 V disappearing during cycling. The first peak is likely due to irreversible capacity during the formation of the initial SEI layer. Other peaks evolve slightly during cycling until there are three peaks during charge and three during discharge. This irreversible change is likely the reason for the sharp drop in capacity in early cycles. In

64

order to correlate the features in the differential capacity with structural changes, *in situ*

XRD experiments were performed.
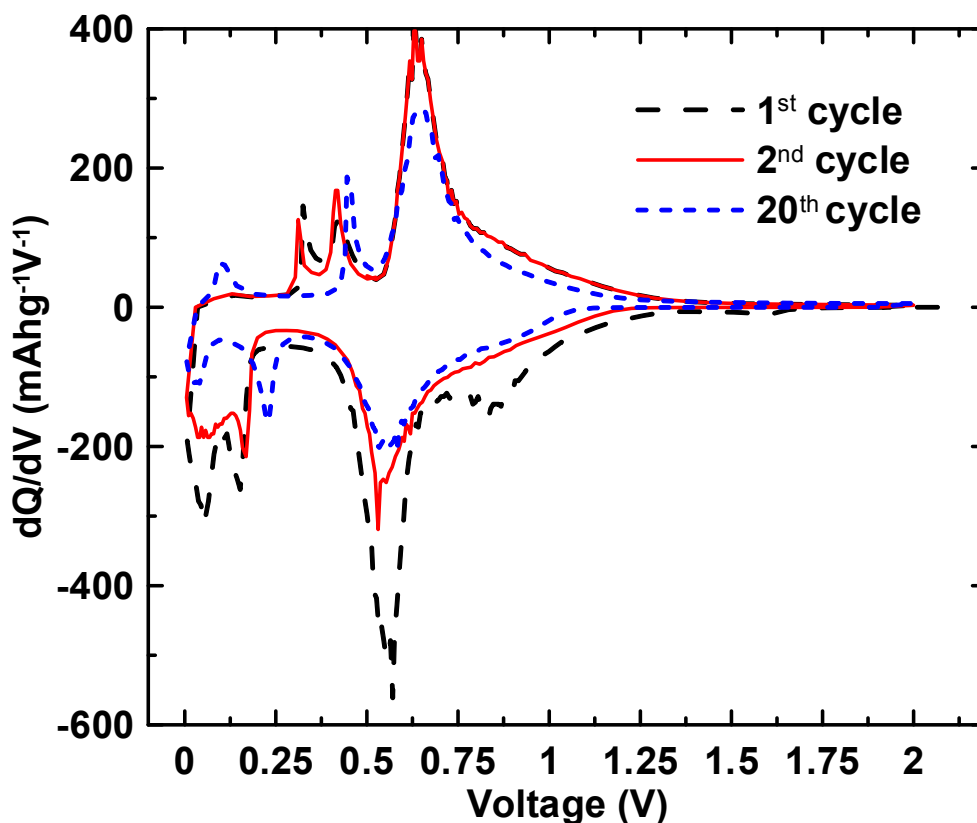


Figure 5.11 The differential capacity of $Na_{0.6}Ni_{0.3}Ti_{0.7}O_2$.

Figure 5.12 shows the XRD patterns of a $Na_{0.6}Ni_{0.3}Ti_{0.7}O_2$ *in situ* XRD cell during

the first 1.5 cycles between 5 mV and 2.0 V. Some of the peaks in the XRD patterns are

caused by the Be window, with BeO on its surface, and cell parts for the *in situ* cell. These

peaks do not shift during the charge and discharge process and are indicated in Figure 5.12.

The initial XRD pattern is that of the phase pure $Na_{0.6}Ni_{0.3}Ti_{0.7}O_2$. During cycling only

shifts in peak positions were observed and the electrode material remains in the P2 structure

throughout the entire charging and discharging process. This is indicative of a reversible

intercalation process. The stability of the P2 phase during cycling has been previously

described. This phase requires a π/3 rotation of the $MO_6$ octahedra and a breaking of M-

O bonds to convert to the other layered phases, which is energetically unfavorable [88,89]. This result was further verified by *ex situ* XRD measurements of electrode material cycled to certain voltages. Figure 5.13 shows these *ex situ* XRD patterns of the pristine electrode material after incorporation into a half cell as well as cells charged to 2 V and discharged to 0 V. All display the P2 structure and additionally confirm the P2 structure is maintained throughout cycling, with small variations in the lattice constants.
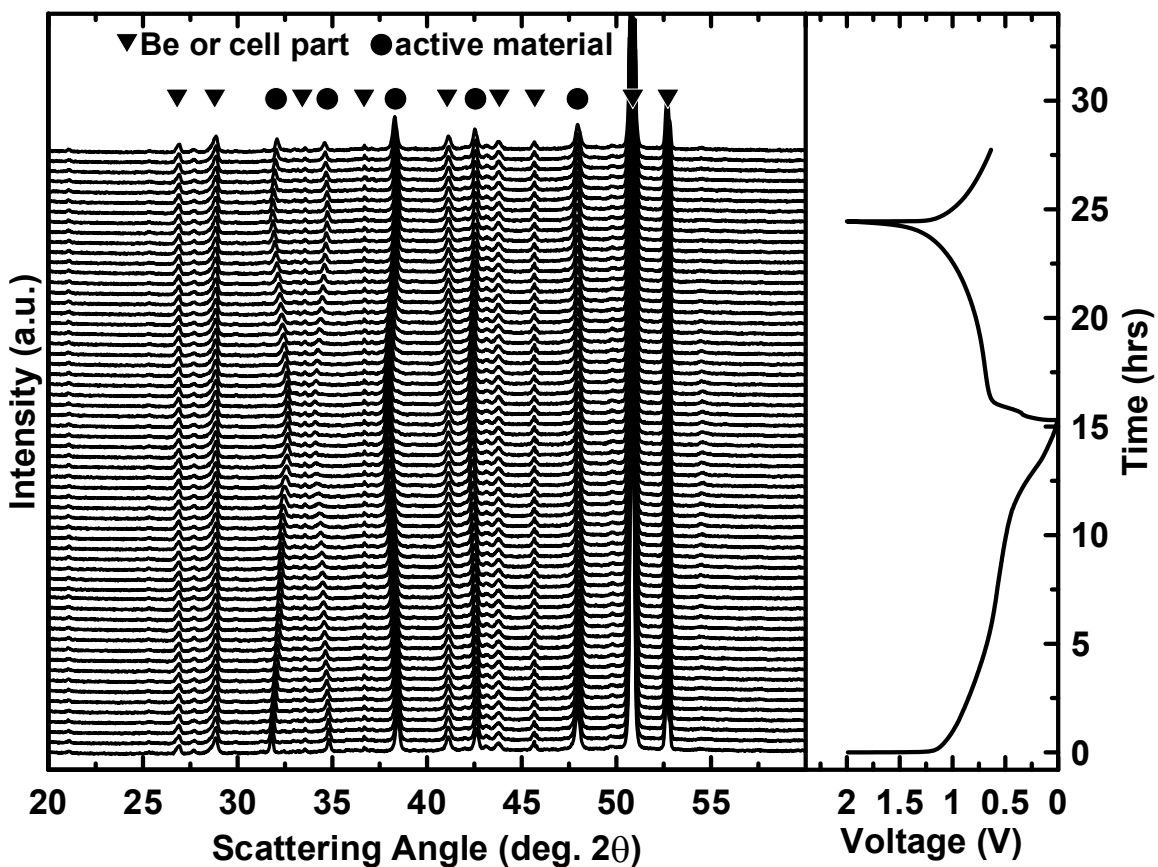


Figure 5.12 XRD patterns measured during charge and discharge of the $Na_{0.6}Ni_{0.3}Ti_{0.7}O_2$ *in situ* cell with the corresponding voltage-time curve.
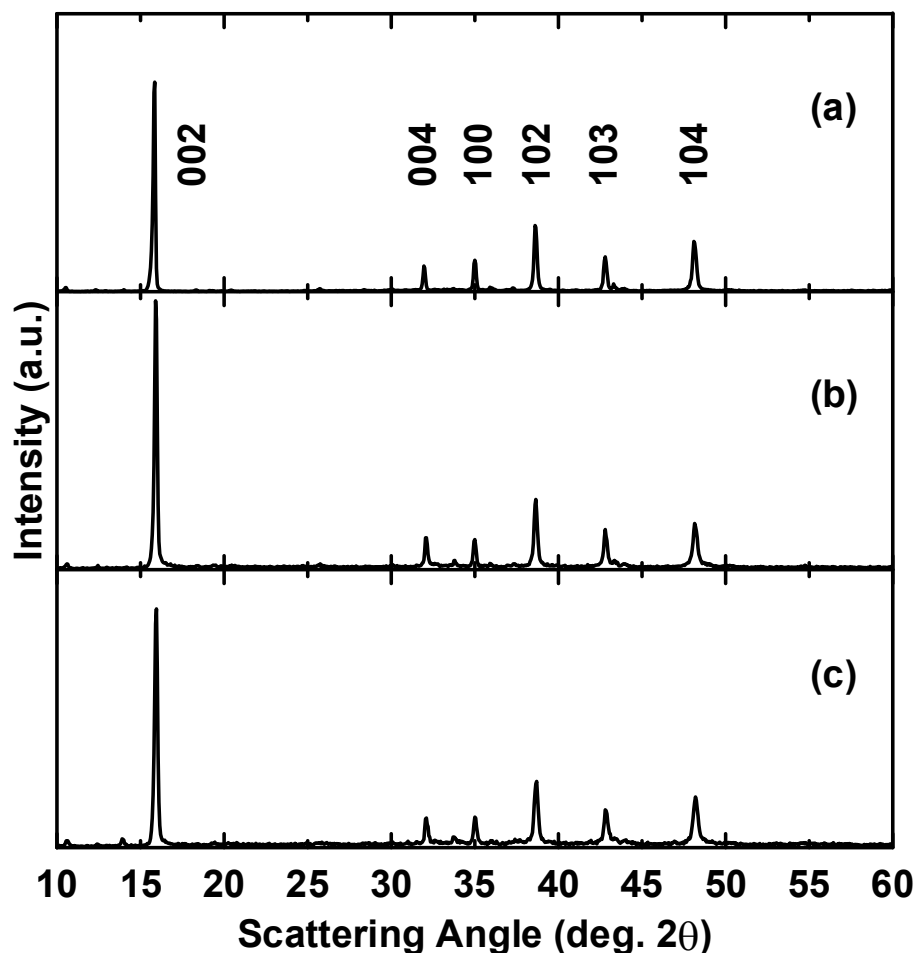
Figure 5.13 (a) XRD pattern of the pristine $Na_{0.6}Ni_{0.3}Ti_{0.7}O_2$ phase, with the Miller indices indicated. *Ex situ* XRD pattern of the $Na_{0.6}Ni_{0.3}Ti_{0.7}O_2$ charged to 2 V and discharged to 0 V, (b) and (c) respectively.

During the *in situ* first discharge the (00*l*) peaks shift to higher angle while the (10*l*) peaks shift to lower angle. This result indicates that the *a*-axis is expanding and the *c*-axis is contracting while sodium is being inserted. During the *in situ* discharge process, the opposite occurs and the peaks shift to their original position. Figure 5.14 shows the voltage, lattice constants, and unit cell volume plotted versus time. Overall, the changes in the lattice constants are small and correspond to a volume expansion of only 1.6% at full sodiation. This small expansion is advantageous, since materials with low volume change during cycling are expected to maintain good structural integrity during cycling. However,

the change in lattice constants does not appear to be completely reversible, but increases after each cycle. Further studies are needed to investigate if irreversible structural changes occur in $Na_{0.6}Ni_{0.3}Ti_{0.7}O_2$ after many cycles, as suggested by the changes in the differential capacity curves.
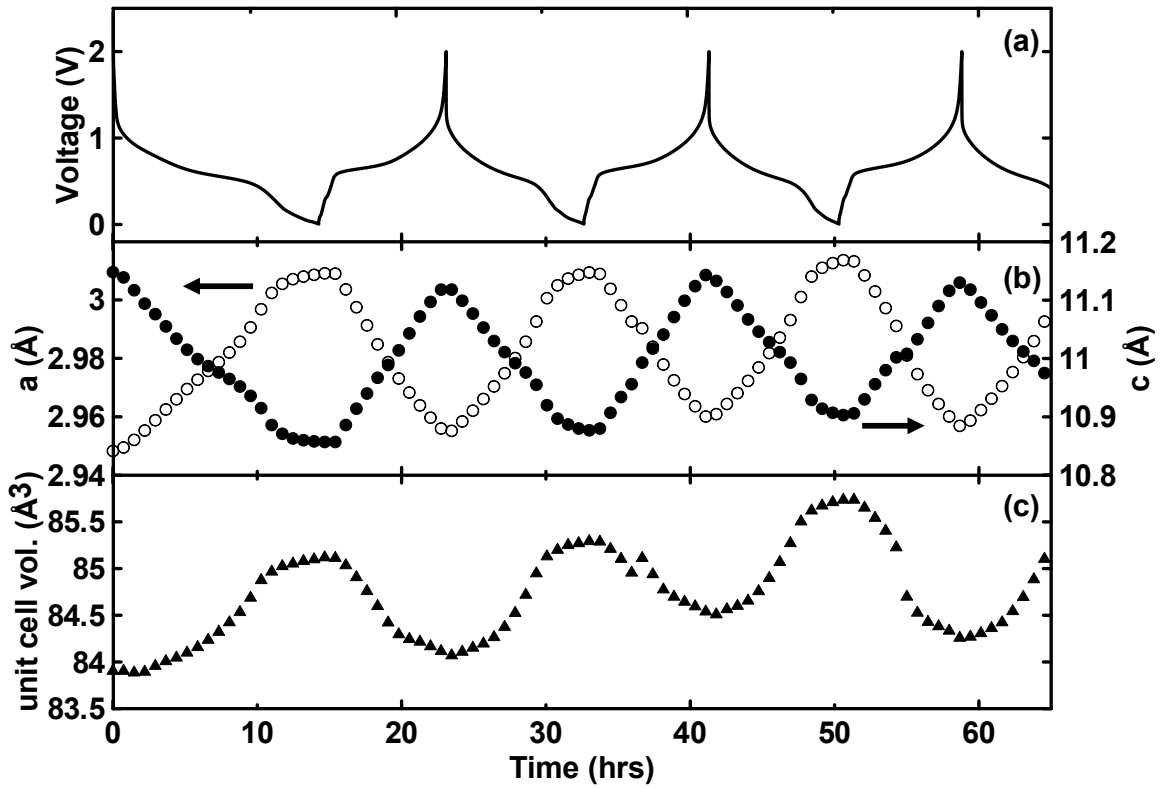


Figure 5.14 (a) Voltage curve of a $Na_xNi_{0.3}Ti_{0.7}O_2$ *in situ* X-ray cell. (b) The variation in the lattice parameters *a* (open circles) and *c* (closed circles) vs. time corresponding to the voltage curve in (a). (c) Unit cell volume vs. time also corresponding to the voltage curve in (a).

Figure 5.15 shows voltage curves of $Na_{0.6}Ni_{0.3}Ti_{0.7}O_2$ cycled at cycling rates ranging from C/10 (11 mA/g) to 5C (550 mA/g). C-rate was defined based on the theoretical capacity calculated from the sodium vacancies, which is equal to 110 mAh/g. The rate capability was poor. Cycling at C/5 resulted in a capacity that was 42% of the C/10 capacity. Further improvements in rate capability are required for such materials to be practical.

68
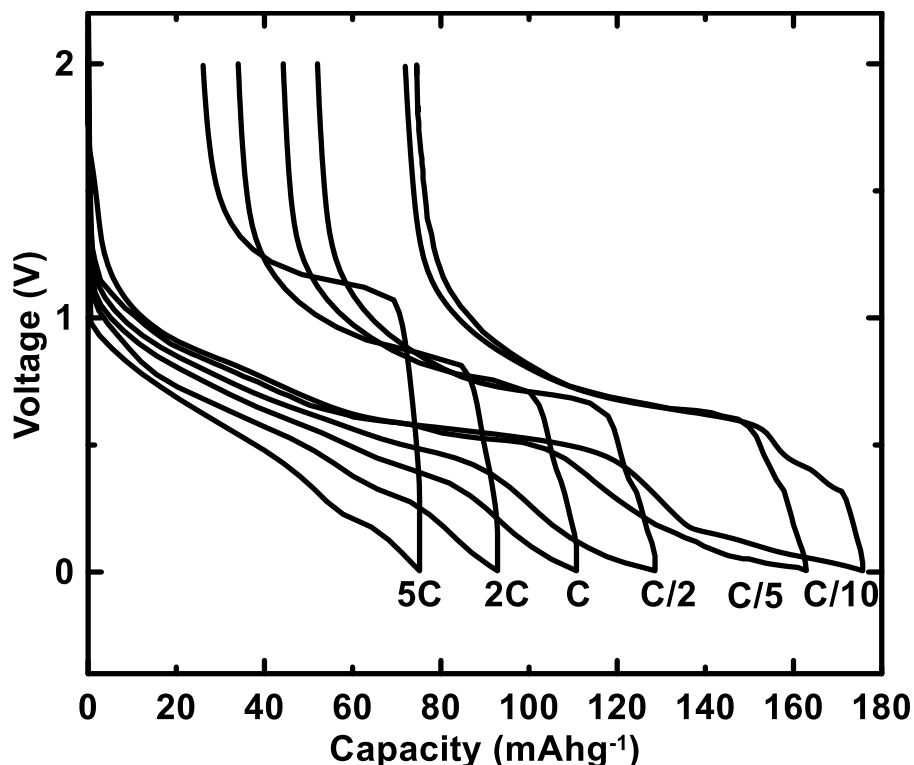
Figure 5.15 Voltage curves of $Na_{0.6}Ni_{0.3}Ti_{0.7}O_2$ cells cycled at different rates. The cells were discharged to 0.005 V and charged to 2 V at rates of C/10, C/5, C/2, C, 2C, and 5C.

## 5.4 Conclusions

In summary, the $Na_xNi_{x/2}Ti_{1-x/2}O_2$ ($0.5 \leq x \leq 1.0$) series of oxides were synthesized via a facile solid-state reaction. These materials were found to have remarkably stability at 0 V vs. Na and can reversibly intercalate sodium at an average potential of 0.7 V with low hysteresis. This is the lowest voltage reported for a layered material that has been cycled using bulk powders. These materials do not require the large amounts of carbon black or conductive coatings that are typically required to cycle anode materials derived from white insulating titanates [90]. This low voltage capacity was demonstrated to arise from the existence of sodium ion vacancies in the layered P2 lattice structure as the capacity increases with increasing sodium vacancy in the structure according to (1-x).

$Na_{0.6}Ni_{0.3}Ti_{0.7}O_2$ had good cyclability (50 cycles) and delivered a first charge capacity of 100 mAh/g during cycling between 0.005 and 2 V, which correlates to a volumetric capacity of about 400 Ah/L. The P2 structure is maintained throughout cycling, as confirmed by i*n situ* and *ex situ* XRD, confirming an intercalation process. Such materials may represent an entire family of layered transition metal titanates with possible low potential versus sodium for application as sodium-ion anodes. These properties make sodium transition metal titanates a promising new area of study for anode materials.

## 5.5 Other Transition Metal Oxide Phases

The use of transition metal titanates offers a new strategy towards making negative electrodes for sodium-ion cells, from which high energy density bulk intercalation materials may be developed. Here a few such examples with different structure types were explored as for use as anode materials in sodium-ion batteries.

### 5.5.1 NiTiO$_3$ Ilmenite Structure

There exist other metal oxide phases that contain nickel and titanium transition metals that could have a sodium intercalation potential similar to the Na$_x$Ni$_{x/2}$Ti$_{1-x/2}$O$_2$ - system. One such structure is the ilmenite NiTiO$_3$ compound. It can be synthesized via a facile solid-state synthesis by mixing stoichiometric amounts of NiO and TiO$_2$ and heating at 1000 °C for 10 hours [91]. The dull yellow powder has the crystal structure seen in Figure 5.16. It consists of layered transition metal octahedra where oxygen atoms reside at the vertices and zigzag open tunnels that could intercalate sodium.
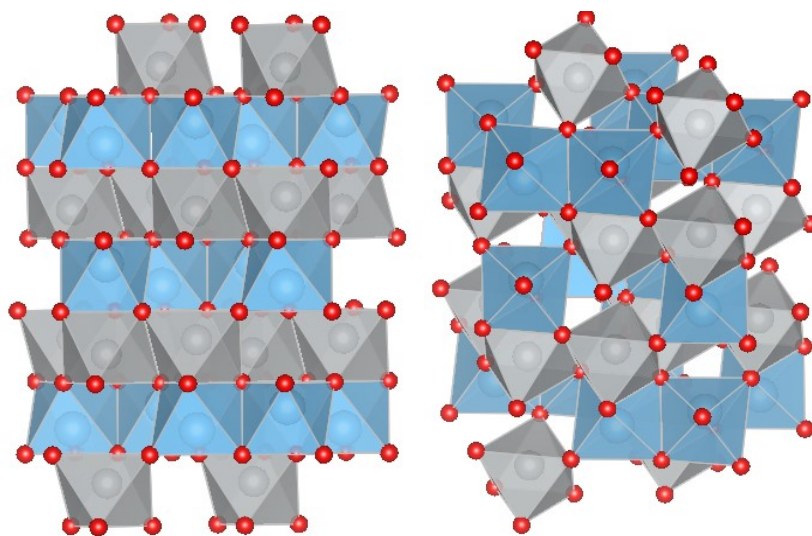


Figure 5.16 Ilmenite crystal structure of the NiTiO$_3$ material. The red, grey, and blue spheres represent oxygen, titanium, and nickel ions respectively.

The XRD experimental pattern of $NiTiO_3$ is shown in Figure 5.17 along with a Rietveld refinement, with parameters used shown in Table 5.2.  The structure was indexed using the ilmenite structure type and the calculated pattern shows good agreement with the experimental pattern data.
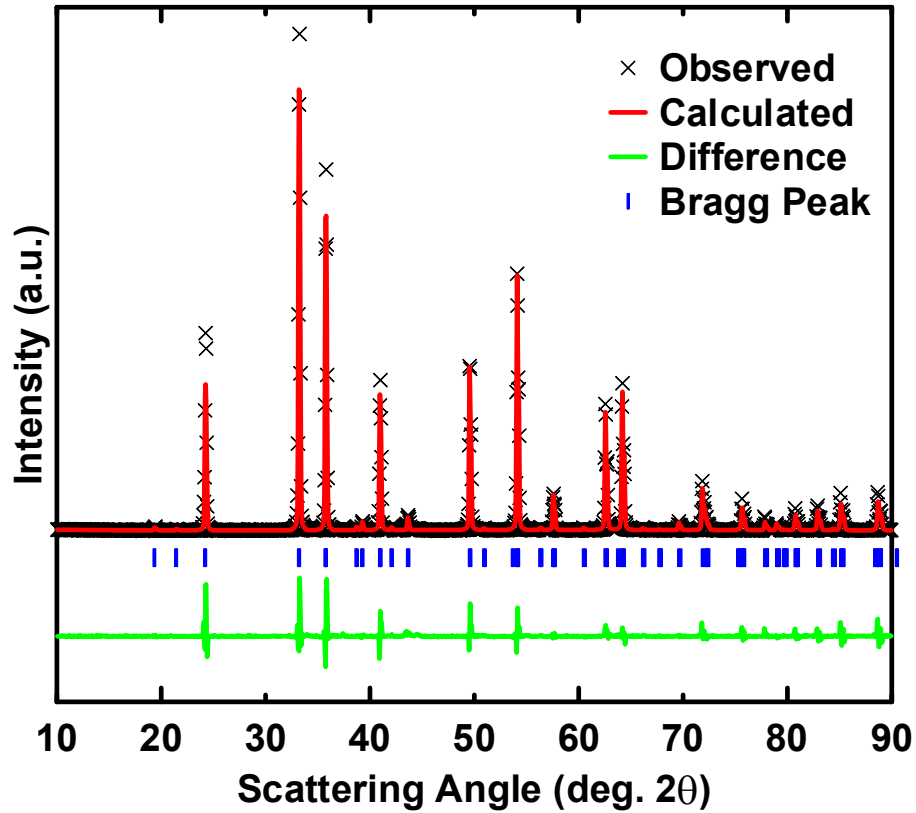


Figure 5.17:  XRD pattern and Rietveld refinement of $NiTiO_3$.

Table 5.2 Parameters used to refine the $NiTiO_3$ ilmenite structure.

| NiTiO₃ (R$\bar{3}$) | | | | | |
|---|---|---|---|---|---|
| atom | site | x | y | z | occupancy |
| Ni | 6c | 0 | 0 | 0.1492(9) | 1.0243(0) |
| Ti | 6c | 0 | 0 | 0.3559(1) | 1.0077(0) |
| O | 18f | 0.3070(2) | 0.0123(4) | 0.2542(1) | 3.1997(7) |
| Cell parameters | a | | b | | c | |
| | 5.023(3) | | 5.023(3) | | 13.77(1) | R-factor 3.81 |
| | α | | β | | γ | |
| | 90 | | 90 | | 120 | |

There are two vacancies present per formula unit. The theoretical capacity for one sodium intercalant per $NiTiO_3$ unit is 173 mAh/g. Figure 5.18 shows the voltage versus specific capacity curve. The reversible experimental capacity for the second discharge cycle is very close to the theoretical capacity for one sodium.
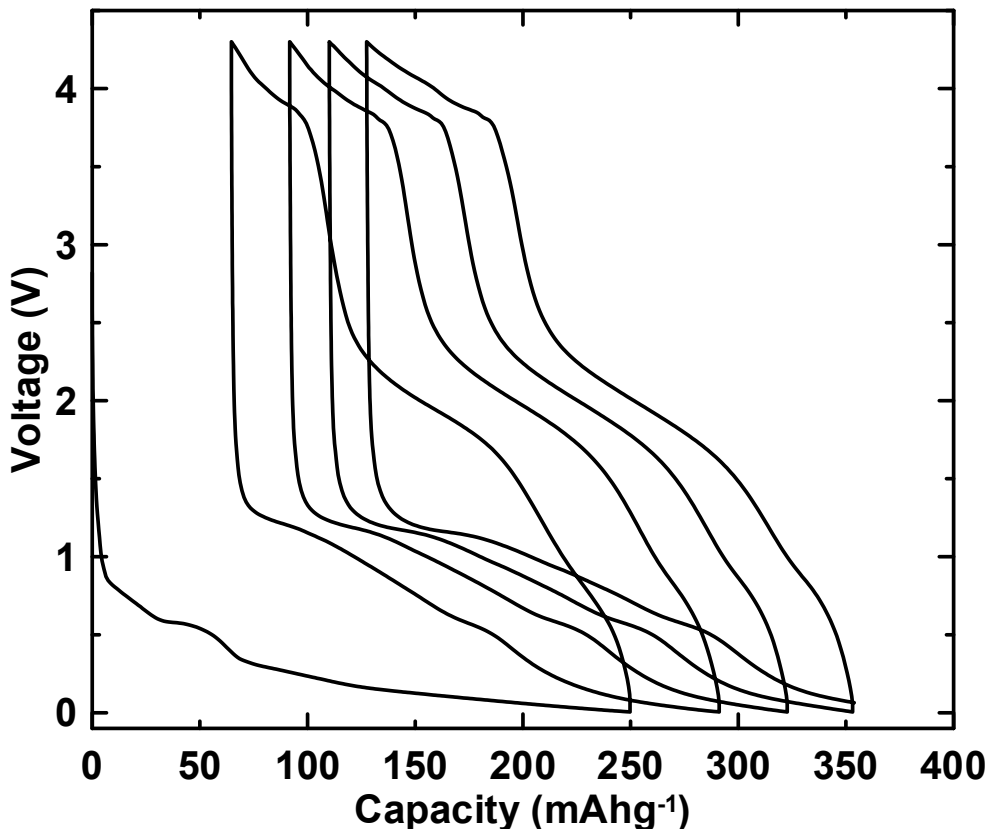


Figure 5.18: Voltage versus capacity curve of $NiTiO_3$ from 0.005 mV – 4.3 V.

Some irreversible capacity is observed as well as large hysteresis, which may be indicative of a conversion reaction instead of intercalation. It should also be noted that this material was cycled over a large voltage range of 0.005 mV to 4.3 V, which would not be practical for cycling in a full-cell. Figure 5.19 shows the charge and discharge capacities versus cycle number.
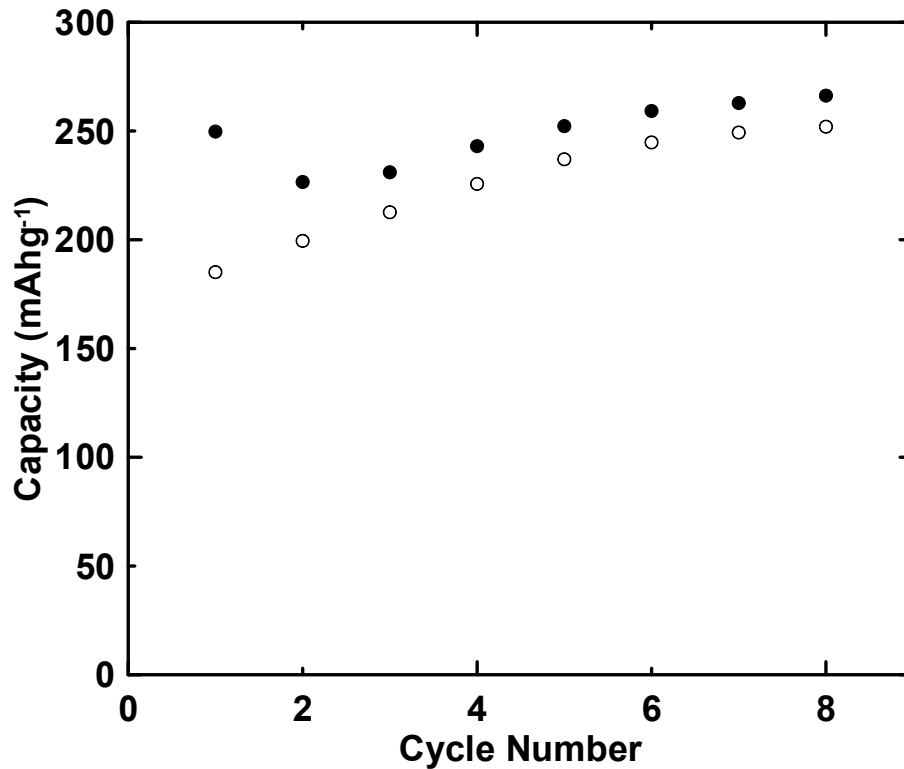
Figure 5.19:  Charge (solid circles) and discharge (open circles) capacities versus cycle number for NiTiO$_3$ during cycling from 0.005 mV − 4.3 V.

The material displays interesting behavior as it cycles.  The capacity actually increases the more it is cycled.  Cycling was also performed at lower voltages and the capacity was small.  Further studies are desirable to understand the irreversible capacity and determine if intercalation or conversion reactions or both are taking place in this structure.

## 5.5.2 Fe$_2$TiO$_5$ and FeTi$_2$O$_5$ Pseudobrookite Structure

Another transition metal titanate structure with a large tunnel network that could intercalate sodium is the pseudobrookite structure. Fe$_2$TiO$_5$ and FeTi$_2$O$_5$ with the pseudobrookite structure can be synthesized by mixing stoichiometric amounts of Fe$_2$O$_3$ and TiO$_2$ and heating at 900 °C for 24 hours. Figure 5.20 shows the crystal structure of the Fe$_2$TiO$_5$ pseudobrookite material.
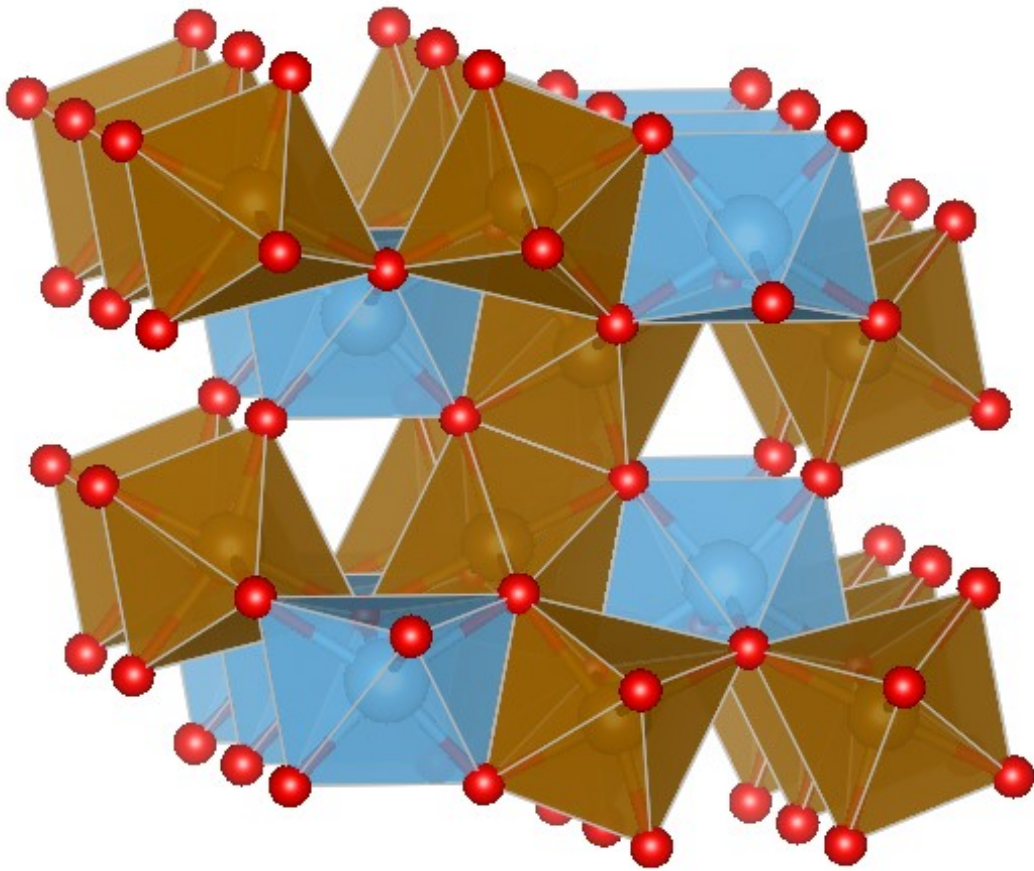


Figure 5.20: Pseudobrookite crystal structure of the Fe$_2$TiO$_5$ material.

Like NiTiO$_3$, pseudobrookite also has transition metal octahedra with oxygen atoms at the vertices. However, it has larger tunnels that extend the length of its crystal structure

(instead of zigzags like ilmenite). The experimental XRD patterns of $Fe_2TiO_5$ and $FeTi_2O_5$ are shown in Figure 5.21 and they match a pseudobrookite structure type.
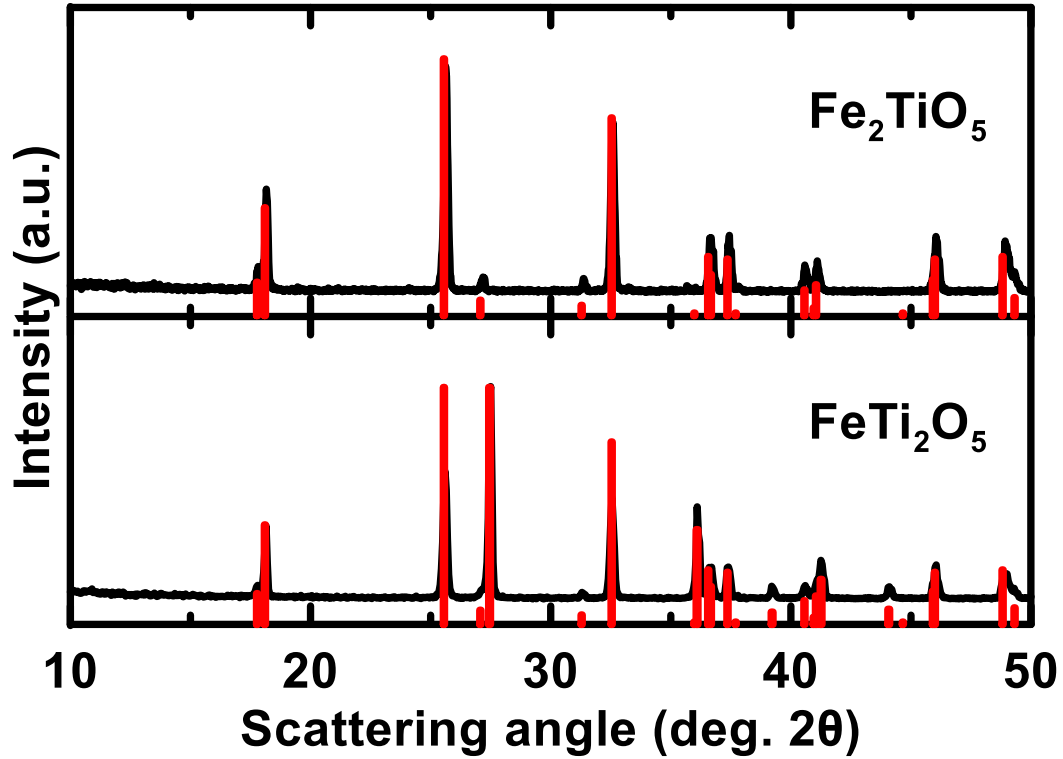


Figure 5.21: Experimental XRD patterns of the pseudobrookite $Fe_2TiO_5$ (top) and $FeTi_2O_5$ (bottom) powders with matching database patterns from Match shown.

The theoretical capacity for one sodium per $FeTi_2O_5$ and $Fe_2TiO_5$ unit is 116 and 112 mAh/g respectively, however these values are expected to be low as the number of vacancies in the structure should allow for more than one sodium per formula unit to be intercalated if indeed intercalation is possible. Figure 5.22 and Figure 5.23 show the voltage versus capacity profile of $FeTi_2O_5$ and $Fe_2TiO_5$, respectively.
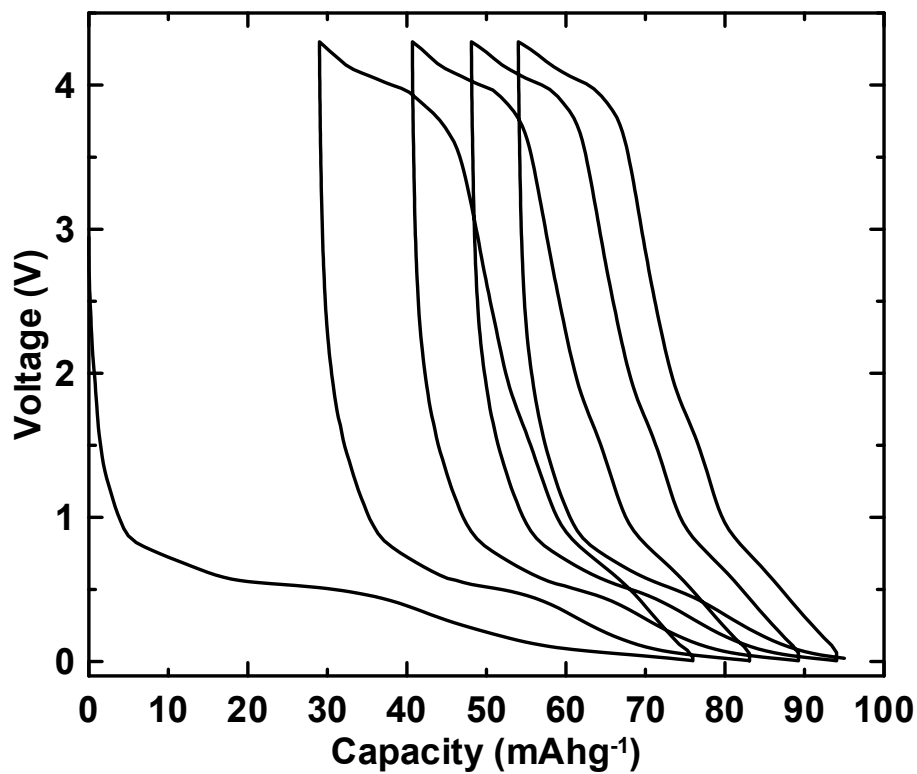
Figure 5.22: Voltage versus capacity curve of pseudobrookite $FeTi_2O_5$.
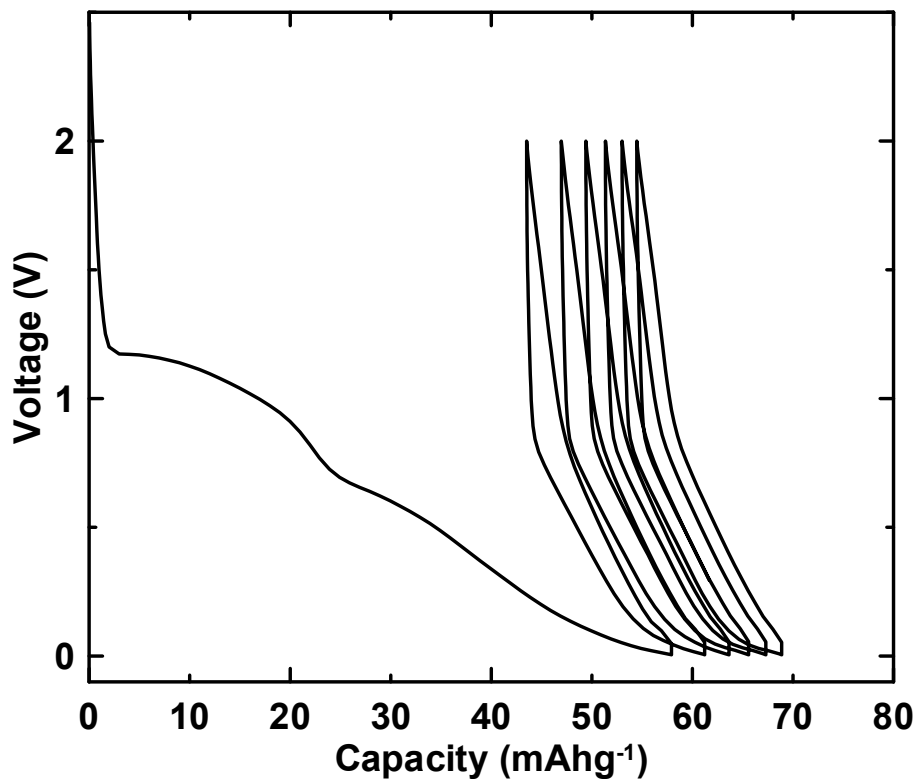


Figure 5.23: Voltage versus capacity curve of pseudobrookite $Fe_2TiO_5$.

Both pseudobrookite structures have low reversible capacities and high irreversible capacities. These results show that the pseudobrookite would make a poor negative electrode material for sodium-ion batteries. It is unclear at this time if this indicative of all transition metal oxides of pseudobrookite structure or if other mixtures of transition metals would yield improved results.

# CHAPTER 6      CONCLUSIONS

## 6.1 Cathode Materials for Sodium-ion Batteries

Studies on cathode materials for sodium-ion batteries have re-emerged after their initial appearance in the early 1980s. Currently, many layered $NaMO_2$ cathodes have been reported, where M could be a single first row transition metal or a mixture of two or three transition metals. When more than one transition metal are used the usual multiple step voltage profiles are typically smoothed to a single sloping plateau. Higher capacities can also be achieved as more vacancies during cycling are tolerated.

When M = Ni or Mn high voltages versus sodium metal are expected. The lithium counterpart, Li-Ni-Mn-O series, is highly studied and displays desirable electrochemical performance. In this work the layered $NaNi_xMn_{1-x}O_2$ (where x = 0, 0.25, 0.33, 0.5, 0.66, and 1) series was synthesized. Synthesis was non-trivial, thus different conditions were needed depending on the composition to obtain phase pure compositions. Phase diagrams were constructed for each syntheses method. These materials have a monoclinically distorted O'3 structure (x = 0, 1), P2 structure ($0.25 \leq x \leq 0.33$) or an O3 structure ($0.5 \leq x \leq 0.66$). Excepting for x = 0, all compositions have high densities, above 4.6 g/mL. All compositions have high reversible capacities when cycled between 1.8 to 4.3 V, corresponding to volumetric energy densities from 1650 – 2705 Wh/L.

The x = 0.66 composition had the highest first discharge capacity of ~ 190 mAh/g and highest volumetric energy density of 2705 Wh/L. It displayed an average discharge voltage of 3.07 V. This energy density approaches the energy density of Li-ion cathodes

(e.g. ~2900 Wh/L for $LiNi_{1/3}Mn_{1/3}Co_{1/3}O_2$) and is among the highest reported volumetric energy densities for Na-ion battery electrodes.

All compositions in the $NaNi_xMn_{1-x}O_2$ series had poor cycling performance. Further improvements are required for materials in this series to be utilized in practical cells. Future work needs to be done to understand the large irreversible capacities observed for most of the compositions, as well as the role of different electrolytes for this system.

## 6.2 Anode Materials for Sodium-ion Batteries

There is a great need for high energy anode materials for sodium-ion batteries. Not nearly as much success has been reported for the negative electrode compared to the positive electrode. Hard carbon, alloys, and conversion materials have been proposed but all suffer from poor cyclability and/or low energy densities. Relatively few intercalation materials have been suggested, but the ones that have been suggested typically contain titanium. Examples include $TiO_2$ and $Na_2Ti_3O_7$. In this work P2 and O3 layered type oxides containing titanium were demonstrated as a new family of sodium-ion anode materials.

The $Na_xNi_{x/2}Ti_{1-x/2}O_2$ $(0.5 \leq x \leq 1.0)$ series was synthesized by solid-state reactions. These materials were found to have remarkably stability at 0 V vs. Na and can reversibly intercalate sodium at an average potential of 0.7 V with low hysteresis. The $Na_xNi_{x/2}Ti_{1-x/2}O_2$ materials have the lowest voltage reported for a layered material that have been cycled using bulk powders. These materials do not require the large amounts of carbon black or conductive coatings that are typically required to cycle anode materials derived from white insulating titanates. This low voltage capacity was demonstrated to arise from the

existence of sodium ion vacancies in the layered P2 lattice structure as the capacity increases with increasing sodium vacancy in the structure. $Na_{0.6}Ni_{0.3}Ti_{0.7}O_2$ had good cyclability (> 50 cycles) and delivered a first charge capacity of 100 mAh/g during cycling between 0.005 and 2 V, which correlates to a volumetric capacity of about 400 Ah/L. The P2 structure is maintained throughout cycling, as confirmed by *in situ* and *ex situ* XRD, confirming an intercalation process. Such materials represent an entire family of layered transition metal titanates with a low potential versus sodium for application as sodium-ion anodes. These properties make layered sodium transition metal titanates a promising new area of study for anode materials.

Future work is required to understand the intercalation process of these and other $Na_xM_{x/2}Ti_{1-x/2}O_2$ systems. Further studies on increasing the tolerance for sodium vacancies is desirable to increase these material's energy densities. Other research could focus on vanadium mixed metal oxide layered systems for anode applications instead of titanium, as vanadium is another low voltage early first row transition metal.

## 6.3 Sodium-ion Battery Outlook

The outlook for sodium-ion batteries is promising, even though at the moment the overall performance lags behind lithium-ion batteries. Sodium is an inexpensive and abundant alternative to lithium where cost and sustainability of resources is of concern. Inexpensive aluminum can be used for both electrode current collectors, which is a major cost when producing electrochemical cells.

The larger size of sodium ions compared to lithium could be detrimental in various ways. Firstly, extreme volume expansion in alloy anode materials can occur. This larger

size is not always a negative thing. The larger sodium can be advantageous because layered sodium oxides can tolerate more vacancies than the layered lithium oxides. This could increase the volumetric capacity and thus compensate for the larger size of sodium.

Secondly, sodium compounds generally show a lower average voltage compared to lithium compounds which is generally thought to reduce energy density. This lower voltage could actually provide areas of research where the lithium analogues have too high a potential to be used with conventional electrolytes, as well as anode materials where the voltage lowering actually leads to an increase in the overall voltage and hence energy density. Furthermore, stable sodium compounds exist for which the lithium counterparts are not stable, this is the most likely source of breakthroughs for sodium-ion battery technology.

There are areas where sodium-ion can compete with lithium-ion batteries, namely grid energy storage. Prototype cells are already being produced indicating that the future for sodium-ion batteries is propitious.

# REFERENCES

[1]  *Linden's Handbook of Batteries*; Linden, D.; Reddy, T.B., Eds.; 4th ed.; McGraw-Hill, **2010**; p. 1200.

[2]  Van Noorden, R. A Better Battery. *Nature*, **2014**, *507*, 26–28.

[3]  Etacheri, V.; Marom, R.; Elazari, R.; Salitra, G.; Aurbach, D. Challenges in the Development of Advanced Li-Ion Batteries: A Review. *Energy Environ. Sci.*, **2011**, *4*, 3243–3262.

[4]  Gaultois, M.W.; Sparks, T.D.; Borg, C.K.H.; Seshadri, R.; Boni, W.D.; Clarke, D.R. Data-Driven Review of Thermoelectric Materials: Performance and Resource Considerations. *Chem. Mater.*, **2013**, *25*, 2911–2920.

[5]  Vikström, H.; Davidsson, S.; Höök, M. Lithium Availability and Future Production Outlooks. *Appl. Energy*, **2013**, *110*, 252–266.

[6]  Palomares, V.; Serras, P.; Villaluenga, I.; Hueso, K.B.; Carretero-González, J.; Rojo, T. Na-Ion Batteries, Recent Advances and Present Challenges to Become Low Cost Energy Storage Systems. *Energy Environ. Sci.*, **2012**, *5*, 5884–5901.

[7]  Ellis, B.L.; Nazar, L.F. Sodium and Sodium-Ion Energy Storage Batteries. *Curr. Opin. Solid State Mater. Sci.*, **2012**, *16*, 168–177.

[8]  Slater, M.D.; Kim, D.; Lee, E.; Johnson, C.S. Sodium-Ion Batteries. *Adv. Funct. Mater.*, **2013**, *23*, 947–958.

[9]  Whittingham, M.S. History, Evolution, and Future Status of Energy Storage. *Proc. IEEE*, **2012**, *100*, 1518–1534.

[10] Gallagher, K.G.; Goebel, S.; Greszler, T.; Mathias, M.; Oelerich, W.; Eroglu, D.; Srinivasan, V. Quantifying the Promise of Lithium–air Batteries for Electric Vehicles. *Energy Environ. Sci.*, **2014**, *7*, 1555.

[11] Sigma-Aldrich http://www.sigmaaldrich.com/canada-english.html (accessed Jun 3, 2014).

[12] Graedel, T.E. On the Future Availability of the Energy Metals. *Annu. Rev. Mater. Res.*, **2011**, *41*, 323–335.

[13] UK Government; Scottish Executive; Welsh Assembly Government; Northern Ireland Administration. Restriction of the Use of Certain Hazardous Substances in Electrical and Electronic Equipment. *Department of Trade and Industry Publication Number URN 03/811*. **2003**, pp. 1–129.

[14] Tsivadze, A.Y.; Kulova, T.L.; Skundin, A.M. Fundamental Problems of Lithium-Ion Rechargeable Batteries. *Prot. Met. Phys. Chem. Surfaces*, **2013**, *49*, 145–150.

[15]   Shannon, R.D. Revised Effective Ionic Radii and Systematic Studies of Interatomic Distances in Halides and Chaleogenides. *Acta Cryst.*, **1976**, *A32*, 752–767.

[16]   Mendiboure, A.; Delmas, C.; Hagenmuller, P. Electrochemical Intercalation and Deintercalation of $Na_xMnO_2$ Bronzes. *J. Solid State Chem.*, **1985**, *57*, 323–331.

[17]   Ma, X.; Chen, H.; Ceder, G. Electrochemical Properties of Monoclinic $NaMnO_2$. *J. Electrochem. Soc.*, **2011**, *158*, A1307–A1312.

[18]   Xu, J.; Lee, D.H.; Meng, Y.S. Recent Advances in Sodium Intercalation Positive Electrode Materials for Sodium Ion Batteries. *Funct. Mater. Lett.*, **2013**, *06*, 1330001–1330007.

[19]   Oh, S.-M.; Myung, S.-T.; Hassoun, J.; Scrosati, B.; Sun, Y.-K. Reversible $NaFePO_4$ Electrode for Sodium Secondary Batteries. *Electrochem. commun.*, **2012**, *22*, 149–152.

[20]   Zanini, M.; Shaw, J.L.; Tennehouse, G.J. Behavior of the $Na_xTiS_2$ as an Electrode Material. *Bull. Am. Phys. Soc.*, **1979**, *25*, 201–201.

[21]   Delmas, C.; Braconnier, J.-J.; Fouassier, C.; Hagenmuller, P. Electrochemical Intercalation of Sodium in $NaCoO_2$ Bronzes. *Solid State Ionics*, **1981**, *3*, 165–169.

[22]   Braconnier, J.-J.; Delmas, C.; Hagenmuller, P. Study of the $Na_xCrO_2$ and $Na_xNiO_2$ Systems by Electrochemical Desintercalation. *Mater. Res. Bull.*, **1982**, *17*, 993–1000.

[23]   Komaba, S.; Takei, C.; Nakayama, T.; Ogata, A.; Yabuuchi, N. Electrochemical Intercalation Activity of Layered $NaCrO_2$ vs. $LiCrO_2$. *Electrochem. commun.*, **2010**, *12*, 355–358.

[24]   Takeda, Y.; Nakahara, K.; Nishijima, M.; Imanishi, N.; Yamamoto, O. Sodium Deintercalation From Sodium Iron Oxide. *Mater. Res. Bull.*, **1994**, *29*, 659–666.

[25]   Yabuuchi, N.; Yoshida, H.; Komaba, S. Crystal Structures and Electrode Performance of Alpha-$NaFeO_2$ for Rechargeable Sodium Batteries. *Electrochemistry*, **2012**, *80*, 716–719.

[26]   Berthelot, R.; Carlier, D.; Delmas, C. Electrochemical Investigation of the P2–$Na_xCoO_2$ Phase Diagram. *Nat. Mater.*, **2011**, *10*, 74–80.

[27]   Vassilaras, P.; Ma, X.; Li, X.; Ceder, G. Electrochemical Properties of Monoclinic $NaNiO_2$. *J. Electrochem. Soc.*, **2012**, *160*, A207–A211.

[28]   Arai, H.; Okada, S.; Sakurai, Y.; Yamaki, J. Electrochemical and Structural Study of $Li_2CuO_2$, $LiCuO_2$ and $NaCuO_2$. *Solid State Ionics*, **1998**, *106*, 45–53.

[29]  Ono, Y.; Yui, Y.; Hayashi, M.; Hayashi, K.; Asakura, K.; Kobayashi, R.; Kitabayashi, H. Electrochemical Properties and Structural Changes of $NaCuO_2$ for Sodium Secondary Batteries. *224th ECS Meet.*, **2013**, Abstract #370.

[30]  Saadoune, I.; Maazaz, A.; Menetrier, M.; Delmas, C. On the $Na_xNi_{0.6}Co_{0.4}O_2$ System : Physical and Electrochemical Studies. *J. Solid State Chem.*, **1996**, *117*, 111–117.

[31]  Lu, Z.; Dahn, J.R. In Situ X-Ray Diffraction Study of P2-$Na_{2/3}[Ni_{1/3}Mn_{2/3}]O_2$. *J. Electrochem. Soc.*, **2001**, *148*, A1225–A1229.

[32]  Sathiya, M.; Hemalatha, K.; Ramesha, K.; Tarascon, J.-M.; Prakash, A.S. Synthesis, Structure, and Electrochemical Properties of Layered Sodium Insertion Cathode Material: $NaNi_{1/3}Mn_{1/3}Co_{1/3}O_2$. *Chem. Mater.*, **2012**, *24*, 1846–1853.

[33]  Kim, D.; Lee, E.; Slater, M.; Lu, W.; Rood, S.; Johnson, C.S. Layered $Na[Ni_{1/3}Fe_{1/3}Mn_{1/3}]O_2$ Cathodes for Na-Ion Battery Application. *Electrochem. commun.*, **2012**, *18*, 66–69.

[34]  Yuan, D.; Hu, X.; Qian, J.; Pei, F.; Wu, F.; Mao, R.; Ai, X.; Yang, H.; Cao, Y. P2-Type $Na_{0.67}Mn_{0.65}Fe_{0.2}Ni_{0.15}O_2$ Cathode Material with High-Capacity for Sodium-Ion Battery. *Electrochim. Acta*, **2014**, *116*, 300–305.

[35]  Thorne, J.S.; Dunlap, R. A.; Obrovac, M.N. Structure and Electrochemistry of $Na_xFe_xMn_{1-x}O2$ ($1.0 \le X \le 0.5$) for Na-Ion Battery Positive Electrodes. *J. Electrochem. Soc.*, **2012**, *160*, A361–A367.

[36]  Mortemard de Boisse, B.; Carlier, D.; Guignard, M.; Delmas, C. Structural and Electrochemical Characterizations of P2 and New O3-$Na_xMn_{1-y}Fe_yO_2$ Phases Prepared by Auto-Combustion Synthesis for Na-Ion Batteries. *J. Electrochem. Soc.*, **2013**, *160*, A569–A574.

[37]  Yabuuchi, N.; Kajiyama, M.; Iwatate, J.; Nishikawa, H.; Hitomi, S.; Okuyama, R.; Usui, R.; Yamada, Y.; Komaba, S. P2-Type $Na_{(x)}[Fe_{(1/2)}Mn_{(1/2)}]O_2$ Made from Earth-Abundant Elements for Rechargeable Na Batteries. *Nat. Mater.*, **2012**, *11*, 512–517.

[38]  Yoshida, H.; Yabuuchi, N.; Komaba, S. $NaFe_{0.5}Co_{0.5}O_2$ as High Energy and Power Positive Electrode for Na-Ion Batteries. *Electrochem. commun.*, **2013**, *34*, 60–63.

[39]  Wang, X.; Tamaru, M.; Okubo, M.; Yamada, A. Electrode Properties of P2−$Na_{2/3}Mn_yCo_{1-y}O_2$ as Cathode Materials for Sodium-Ion Batteries. *J. Phys. Chem.*, **2013**, *117*, 15545–15551.

[40]  Vassilaras, P.; Toumar, A.J.; Ceder, G. Electrochemical Properties of $NaNi_{1/3}Co_{1/3}Fe_{1/3}O_2$ as a Cathode Material for Na-Ion Batteries. *Electrochem. commun.*, **2014**, *38*, 79–81.

85

[41] Komaba, S.; Yabuuchi, N.; Nakayama, T.; Ogata, A.; Ishikawa, T.; Nakai, I. Study on the Reversible Electrode Reaction of $Na_{1-x}Ni_{0.5}Mn_{0.5}O_2$ for a Rechargable Sodium-Ion Battery. *Inorg. Chem.*, **2012**, *51*, 6211–6220.

[42] Komaba, S.; Nakayama, T.; Ogata, A.; Shimizu, T.; Takei, C.; Takada, S.; Hokura, A.; Nakai, I. Electrochemically Reversible Sodium Intercalation of Layered $NaNi_{0.5}Mn_{0.5}O_2$ and $NaCrO_2$. *ECS Trans.*, **2009**, *16*, 43–55.

[43] Chevrier, V.L.; Ceder, G. Challenges for Na-Ion Negative Electrodes. *J. Electrochem. Soc.*, **2011**, *158*, A1011–A1014.

[44] Thomas, P.; Billaud, D.; Nancy, I.; Vandoeu, B.P. Electrochemical Insertion of Sodium into Hard Carbons. *Electrochem. Acta*, **2002**, *47*, 3303–3307.

[45] Komaba, S.; Murata, W.; Ishikawa, T.; Yabuuchi, N.; Ozeki, T.; Nakayama, T.; Ogata, A.; Gotoh, K.; Fujiwara, K. Electrochemical Na Insertion and Solid Electrolyte Interphase for Hard-Carbon Electrodes and Application to Na-Ion Batteries. *Adv. Funct. Mater.*, **2011**, *21*, 3859–3867.

[46] Stevens, D.A.; Dahn, J.R. High Capacity Anode Materials for Rechargeable Sodium-Ion Batteries. *J. Electrochem. Soc.*, **2000**, *147*, 1271.

[47] Ponrouch, A.; Dedryvère, R.; Monti, D.; Demet, A.E.; Ateba Mba, J.M.; Croguennec, L.; Masquelier, C.; Johansson, P.; Palacín, M.R. Towards High Energy Density Sodium Ion Batteries through Electrolyte Optimization. *Energy Environ. Sci.*, **2013**, *6*, 2361.

[48] Ellis, L.D.; Hatchard, T.D.; Obrovac, M.N. Reversible Insertion of Sodium in Tin. *J. Electrochem. Soc.*, **2012**, *159*, A1801–A1805.

[49] Senguttuvan, P.; Rousse, G.; Seznec, V.; Tarascon, J.-M.; Palacín, M.R. $Na_2Ti_3O_7$: Lowest Voltage Ever Reported Oxide Insertion Electrode for Sodium Ion Batteries. *Chem. Mater.*, **2011**, *23*, 4109–4111.

[50] Alcantara, R.; Jaraba, M.; Lavela, P.; Tirado, J.L. $NiCo_2O_4$ Spinel : First Report on a Transition Metal Oxide for the Negative Electrode of Sodium-Ion Batteries. *Chem. Mater.*, **2002**, *14*, 2847–2848.

[51] Klein, F.; Jache, B.; Bhide, A.; Adelhelm, P. Conversion Reactions for Sodium-Ion Batteries. *Phys. Chem. Chem. Phys. PCCP*, **2013**, *15*, 15876–15887.

[52] Darwiche, A.; Marino, C.; Sougrati, M.T.; Fraisse, B.; Stievano, L.; Monconduit, L. Better Cycling Performances of Bulk Sb in Na-Ion Batteries Compared to Li-Ion Systems: An Unexpected Electrochemical Mechanism. *J. Am. Chem. Soc.*, **2012**, *134*, 20805–20811.

[53] Qian, J.; Wu, X.; Cao, Y.; Ai, X.; Yang, H. High Capacity and Rate Capability of Amorphous Phosphorus for Sodium Ion Batteries. *Angew. Chem. Int. Ed. Engl.*, **2013**, *52*, 4633–4636.

[54] Dahbi, M.; Yabuuchi, N.; Kobuta, K.; Komaba, S. Red Phosphorus and Negative Electrodes for Na-Ion Batteries. In *17th International Meeting on Lithium-ion Batteries*; Cernobbio, Italy, **2014**; Poster 268.

[55] Maazaz, A.; Delmas, C.; Hagenmuller, P. On the New Phases with Formula $Na_xTiO_2$. *Solid State Ionics*, **1982**, *2*, 759–761.

[56] Maazaz, A.; Delmas, C.; Hagenmuller, P. A Study of the $Na_xTiO_2$ System by Electrochemical Deintercalation. *J. Incl. Phenom.*, **1983**, *1*, 45–51.

[57] Guignard, M.; Didier, C.; Darriet, J.; Bordet, P.; Elkaïm, E.; Delmas, C. P2-$Na_{(x)}VO_2$ System as Electrodes for Batteries and Electron-Correlated Materials. *Nat. Mater.*, **2013**, *12*, 74–80.

[58] Hamani, D.; Ati, M.; Tarascon, J.-M.; Rozier, P. $Na_xVO_2$ as Possible Electrode for Na-Ion Batteries. *Electrochem. commun.*, **2011**, *13*, 938–941.

[59] Kim, S.-W.; Seo, D.-H.; Ma, X.; Ceder, G.; Kang, K. Electrode Materials for Rechargeable Sodium-Ion Batteries: Potential Alternatives to Current Lithium-Ion Batteries. *Adv. Energy Mater.*, **2012**, *2*, 710–721.

[60] Barker, J.; Heap, R.J.; Roche, N.; Tan, C.; Liu, Y.; Sheffield, S. Low Cost Na-ion Battery Technology http://www.faradion.co.uk/products/sodium-technology/ (accessed Aug 19, 2014).

[61] Delmas, C.; Fouassier, C.; Hagenmuller, P. Structural Classification and Properties of the Layered Oxides. *Physica*, **1980**, *99B*, 81–85.

[62] Ong, S.P.; Chevrier, V.L.; Hautier, G.; Jain, A.; Moore, C.; Kim, S.; Ma, X.; Ceder, G. Voltage, Stability and Diffusion Barrier Differences between Sodium-Ion and Lithium-Ion Intercalation Materials. *Energy Environ. Sci.*, **2011**, *4*, 3680–3688.

[63] Shao-Horn, Y.; Levasseur, S.; Weill, F.; Delmas, C. Probing Lithium and Vacancy Ordering in O3 Layered $Li_xCoO_2$ (x ≈ 0.5). *J. Electrochem. Soc.*, **2003**, *150*, A366.

[64] Cullity, B.D. *Elements of X-Ray Diffraction*; 1st ed.; Addison-Wesley Publishing Company Inc.: Reading, Massachusetts, **1956**; p. 531.

[65] Economou, E.N. *The Physics of Solids*; Springer-Verlag: Heidelberg; Berlin, **2010**; pp. 245–272.

[66] Hunter, B. Rietica- A Visual Rietveld Program. In *International Union of Crystallography Commision on Powder Diffraction Newsletter No. 20*; **1998**.

[67] Momma, K.; Izumi, F. VESTA : A Three-Dimensional Visualization System for Electronic and Structural Analysis. *J. Appl. Crystallogr.*, **2008**, *41*, 653–658.

[68] Delmas, C.; Braconnier, J.J.; Maazaz, A.; Hagenmuller, P. Soft Chemistry in $A_xMO_2$ Sheet Oxides. *Rev. Chim. Miner.*, **1982**, *1*, 343–351.

[69] Reed, J.; Ceder, G. Charge, Potential, and Phase Stability of Layered Li($Ni_{0.5}Mn_{0.5}$)$O_2$. *Electrochem. Solid-State Lett.*, **2002**, *5*, A145–A148.

[70] Ohzuku, T.; Makimura, Y. Layered Lithium Insertion Material of LiNi$_{1/2}$Mn$_{1/2}$O$_2$: A Possible Alternative to LiCoO$_2$ for Advanced Lithium-Ion Batteries. *Chem. Lett.*, **2001**, *2*, 744–745.

[71] Rossen, E.; Jones, C.D.W.; Dahn, J.R. Structure and Electrochemistry of Li$_x$Mn$_y$Ni$_{1-y}$O$_2$. *Solid State Ionics*, **1992**, *57*, 311–318.

[72] Parant, J.-P.; Olazcuaga, R.; Devalette, M.; Fouassier, C.; Hagenmuller, P. Sur Quelques Nouvelles Phases de Formule Na$_x$MnO$_2$ ( x ≤ 1 ). *J. Solid State Chem.*, **1971**, *3*, 1–11.

[73] Paulsen, J.M.; Dahn, J.R. Studies of the Layered Manganese Bronzes , Na$_{2/3}$[Mn$_{1-x}$M$_x$]O$_2$ with M=Co, Ni, Li, and Li$_{2/3}$[Mn$_{1-x}$M$_x$]O$_2$ Prepared by Ion-Exchange. *Solid State Ionics*, **1999**, *126*, 3–24.

[74] Komaba, S.; Ishikawa, T.; Yabuuchi, N.; Murata, W.; Ito, A.; Ohsawa, Y. Fluorinated Ethylene Carbonate as Electrolyte Additive for. *ACS Appl. Mater. Interfaces*, **2011**, *3*, 4165–4168.

[75] Delmas, C.; Werner, P. Powder Diffraction Studies of the Ionic Conductor K$_{0.72}$(In$_{0.72}$Sn$_{0.28}$)O$_2$. *Acta Chem. Scand.*, **1978**, *A32*, 329–332.

[76] Molenda, J. Correlation between Electronic and Electrochemical Properties of A$_x$MO$_2$-Type Electrode Materials. Electronic Criterion. *Solid State Ionics*, **1986**, *21*, 263–272.

[77] Yao, X.L.; Xie, S.; Nian, H.Q.; Chen, C.H. Spinel Li$_4$Ti$_5$O$_{12}$ as a Reversible Anode Material down to 0V. *J. Alloys Compd.*, **2008**, *465*, 375–379.

[78] Reddy, M. V.; Subba Rao, G. V.; Chowdari, B.V.R. Nano-(V$_{1/2}$Sb$_{1/2}$Sn)O$_4$: A High Capacity, High Rate Anode Material for Li-Ion Batteries. *J. Mater. Chem.*, **2011**, *21*, 10003.

[79] Armstrong, A.R.; Lyness, C.; Panchmatia, P.M.; Islam, M.S.; Bruce, P.G. The Lithium Intercalation Process in the Low-Voltage Lithium Battery Anode Li$_{(1+x)}$V$_{(1-x)}$O$_2$. *Nat. Mater.*, **2011**, *10*, 223–229.

[80] Imachi, N.; Nakamura, H.; Fujitani, S.; Yamaki, J. Insertion of an Insulating Layer between Cathode and Separator for Improving Storage Characteristics of Li-Ion Batteries. *J. Electrochem. Soc.*, **2012**, *159*, A269–A272.

[81] Yang, Z.; Choi, D.; Kerisit, S.; Rosso, K.M.; Wang, D.; Zhang, J.; Graff, G.; Liu, J. Nanostructures and Lithium Electrochemical Reactivity of Lithium Titanites and Titanium Oxides: A Review. *J. Power Sources*, **2009**, *192*, 588–598.

[82] Ishihara, T.; Akbay, T.; Furutani, H.; Takita, Y. Improved Oxide Ion Conductivity of Co Doped La$_{0.8}$Sr$_{0.2}$Ga$_{0.8}$Mg$_{0.2}$O$_3$ Perovskite Type Oxide. *Solid State Ionics*, **1998**, *113-115*, 585–591.

[83] Shanmugam, R.; Lai, W. Na$_{2/3}$Ni$_{1/3}$Ti$_{2/3}$O$_2$: "Bi-Functional" Electrode Materials for Na-Ion Batteries. *ECS Electrochem. Lett.*, **2014**, *3*, A23–A25.

[84] Yu, H.; Guo, S.; Zhu, Y.; Ishida, M.; Zhou, H. Novel Titanium-Based O3-Type NaTi$_{0.5}$Ni$_{0.5}$O$_2$ as a Cathode Material for Sodium Ion Batteries. *Chem. Commun. (Camb).*, **2013**, *50*, 457–459.

[85] Okada, S.; Takahashi, Y.; Kiyabu, T.; Doi, T.; Yamaki, J.; Nishida, T. Layered Transition Metal Oxides as Cathodes for Sodium Secondary Battery. *210th ECS Meeting*, **2006**, Abstract #201.

[86] Yoshida, H.; Yabuuchi, N.; Kubota, K.; Ikeuchi, I.; Garsuch, A.; Schulz-Dobrick, M.; Komaba, S. P2-Type Na$_{2/3}$Ni$_{1/3}$Mn$_{2/3-x}$Ti$_x$O$_2$ as a New Positive Electrode for Higher Energy Na-Ion Batteries. *Chem. Commun. (Camb).*, **2014**, *50*, 3677–3680.

[87] Shin, Y.; Yi, M. Preparation and Structural Properties of Layer-Type Oxides Na$_x$Ni$_{x/2}$Ti$_{1-x/2}$O$_2$ (0.60 ≤ x ≤ 1.0). *Solid State Ionics*, **2000**, *132*, 131–141.

[88] Pan, H.; Hu, Y.-S.; Chen, L. Room-Temperature Stationary Sodium-Ion Batteries for Large-Scale Electric Energy Storage. *Energy Environ. Sci.*, **2013**, *6*, 2338–2360.

[89] Shacklette, L.W.; Jew, T.R.; Townsend, L. Rechargeable Electrodes from Sodium Cobalt Bronzes. *J. Electrochem. Soc.*, **1985**, *135*, 2669–2674.

[90] Huang, J.P.; Yuan, D.D.; Zhang, H.Z.; Cao, Y.L.; Li, G.R.; Yang, H.X.; Gao, X.P. Electrochemical Sodium Storage of TiO$_2$(B) Nanotubes for Sodium Ion Batteries. *RSC Adv.*, **2013**, *3*, 12593–12597.

[91] Anjana, P.S.; Sebastian, M.T. Synthesis, Characterization, and Microwave Dielectric Properties of ATiO$_3$ (A=Co, Mn, Ni) Ceramics. *J. Am. Ceram. Soc.*, **2006**, *89*, 2114–2117.

# APPENDIX A

July 29, 2014

Journal of the Electrochemical Society
65 South Main Street, Building D
Pennington, New Jersey 08534-2839, USA
tel 1.609.737.1902
fax 1.609.737.2743

I am preparing my Masters thesis for submission to the Faculty of Graduate Studies at Dalhousie University, Halifax, Nova Scotia, Canada. I am seeking your permission to include all of the following paper as a chapter in the thesis:

Low Voltage Sodium Intercalation in $Na_xNi_{x/2}Ti_{1-x/2}O_2$ ($0.5 \leq x \leq 1.0$), R. Fielden and M. N. Obrovac, J. Electrochem. Soc. 2014, 161 (6): A1158-A1163; doi:10.1149/2.118406jes

Canadian graduate theses are reproduced by the Library and Archives of Canada (formerly National Library of Canada) through a non-exclusive, world-wide license to reproduce, loan, distribute, or sell theses. I am also seeking your permission for the material described above to be reproduced and distributed by the LAC (NLC). Further details about the LAC (NLC) thesis program are available on the LAC (NLC) website (www.nlc-bnc.ca).

Full publication details and a copy of this permission letter will be included in the thesis.

Yours sincerely,

Ryan Fielden

---

Permission is granted to include the above-referenced paper in your thesis, provided that you obtain permission of the other individual authors. In the thesis, please acknowledge the authors and the citation given above, and include the words: "Reproduced by permission of ECS — The Electrochemical Society."

8/4/14
Date

John Lewis, Associate Director of Publications

90